MSc thesis in EEMCS

Design and Optimization of Hydrogenated Intrinsic Amorphous Silicon Bilayers for High-efficiency Silicon Heterojunction Solar Cells

Yi Zheng

28 August 2023

A thesis submitted for Master of Science degree in Sustainable Energy Technology at Delft University of Technology.

Yi Zheng: *Design and Optimization of*
Hydrogenated Intrinsic Amorphous Silicon Bilayers for High-efficiency Silicon Heterojunction
Solar Cells (2023)

The work in this thesis was carried out in the:

PVMD group
Delft University of Technology

Student number:	5611059
Email	itsmezhengyi@163.com
Project duration:	31 October 2022 - 28 August 2023
MSc Thesis Committee:	Prof.dr. Olindo Isabella
	Dr.Peyman Taheri
	ir. Yifeng Zhao
	ir. Katarina Kovačević
	Dr. Engin Özkol

Abstract

Silicon heterojunction (SHJ) solar cell technology is one of the most promising PV technologies because of its high power conversion efficiencies, simple fabrication process and low manufacturing cost. The current world record efficiency of SHJ solar cell reaches up to 26.81%. SHJ solar cell produces the highest V_{OC} over 750 mV among the c-Si solar cell technologies because of the excellent surface passivation provided by the few nanometers (i)a-Si:H layers. The objective of this thesis is to design and optimize the (i)a-Si:H bilayers that not only ensure excellent c-Si surface passivation quality but also allow less-resistive transport of charge carriers in SHJ solar cells.

First, a database focusing on the microstructure properties of (i)a-Si:H layers was established. The database was compiled by systematically varying the PECVD deposition parameters of the pressure, power, and hydrogen dilution ratio. By means of FTIR (Fourier Transform Infrared Spectroscopy) characterizations, higher power and pressure were found to correspond with an increased absorption strength of high stretching modes (HSM), which indicated a higher R* and hydrogen content. These conditions led to the formation of a film that is rich in voids and hydrogen. Conversely, a denser a-Si:H film could be achieved by increasing the hydrogen dilution ratio, where the low stretching modes (LSM) were increased and became dominant. Overall, the built database showcases the possibilities to deposit (i)a-Si:H layers with microstructure factor spanning from 0.193 to 0.805.

Subsequently, passivation optimization of the (i)a-Si:H bilayer on textured (111)-orientated c-Si wafers has been conducted. The optimal passivation is achieved by the combination of a 1 nm underdense i1 layer and a 9 nm dense i2 layer. The void-rich i1 layer with R* = 0.732 and the dense i2 layer with R* = 0.205 improved the passivation greatly from 2 ms to 7.5 ms, as compared to unoptimized STD1 layer (R* = 0.261) and STD2 layer (R* = 0.314). Despite various passivation qualities enabled by various bilayer structures, after hydrogen plasma treatment (HPT), the lifetime of all increased drastically to 17 ms, accompanied by increases FTIR-characterized in both H content and R*, which may indicate that passivation could be saturated after HPT. However, the passivation trend after VHF treatment was not clear. This could potentially be the instability in the PECVD deposition tool.

Finally, (i)a-Si:H bilayers were implemented into FBC-SHJ solar cells, solar cells endowed with a bilayer consisting of X1 layer (R* = 0.382) and D2 layer (R* = 0.205) exhibited an average Voc of 715 mV. Combined with a denser D2 film, R_S is reduced, helping to counteract the elevated series resistance associated with the incorporation of the X1 layer, contributing to the enhancement of the fill factor from 78.65% to 80.53%, although at the expense if a slightly lower V_{OC}. The best-performing cell X1 + D2 with treatments gives achieved the highest efficiency of 23.23% (22.33 % on average) and the highest V_{OC} of 717

mV compared with an average of 22.24% and 711 mV of the 'non-optimized' standard cells fabricated. It is also observed that after treatments, the FF increases while V_{OC} slightly reduces. However, the observed lack of a clear efficiency improvement when using the optimized bilayer as compared to the 'non-optimized' standard bilayer could be attributed to the instability of the PECVD tool, which primarily affects the lifetime of precursors, coupled with the relatively large error bars present in the results.

Acknowledgements

Firstly, I would like to express my great thanks to my three daily supervisors and supervisor:

A great thanks to ir. Yifeng Zhao, my daily supervisor, is the guide for my whole experiment and thesis.

A great thanks to ir. Katarina Kovačević, my other daily supervisor, is always available and happy to help and encourage me anytime any day of anything, and thinking of every detail in the lab.

A great thanks to Dr. Engin Özkol, my daily supervisor since I entered PVMD, who is always happy to buy me a cup of coffee and fixes everything in the lab.

Also my greatest appreciation to my supervisor prof. dr. Olindo Isabella for leading me through the area of solar cells.

Special thanks to ir. Liqi Cao for being my buddy during weekends and fixing all the matters that happening in the lab. My thanks also go to ir. Yingwen Zhao, ir. Haoxu Wang, ir. Wenxian Wang, ir. Jin Yan, Wanyu Si and Yan Wang, for the joyful accompanies in the lab during night and weekends. Tons of thanks to all the technicians for fixing types of equipment and for solving all my questions.

Finally, thanks to all the support from my family and friends.

Contents

List of Figures

List of Tables

1 Introduction

1.1 Current status of Solar energy

The growing concerns related to global climate change and the increasing demand for energy have driven a global shift towards renewable energy sources, aligning with the objectives of the Paris Agreement [1], [2]. Photovoltaics (PV) have emerged as a pivotal component in this energy transition.

As depicted in Figure 1.1, there is a remarkable surge in solar capacity installation in 2022, with 239 GW of new grid-connected solar capacity added worldwide. This growth represented a substantial 45% increase compared to the previous year's addition of 165 GW. By the end of 2022, the global cumulative installed solar capacity experienced a significant expansion of 25%, reaching 1,177 GW, in contrast to the 938 GW recorded in 2021 [3]. Based on estimates, it is speculated that the installed solar PV capacity could reach 617 GW by the year 2027, resulting in a global installed PV generation capacity of 3.5 TW within the next five years.

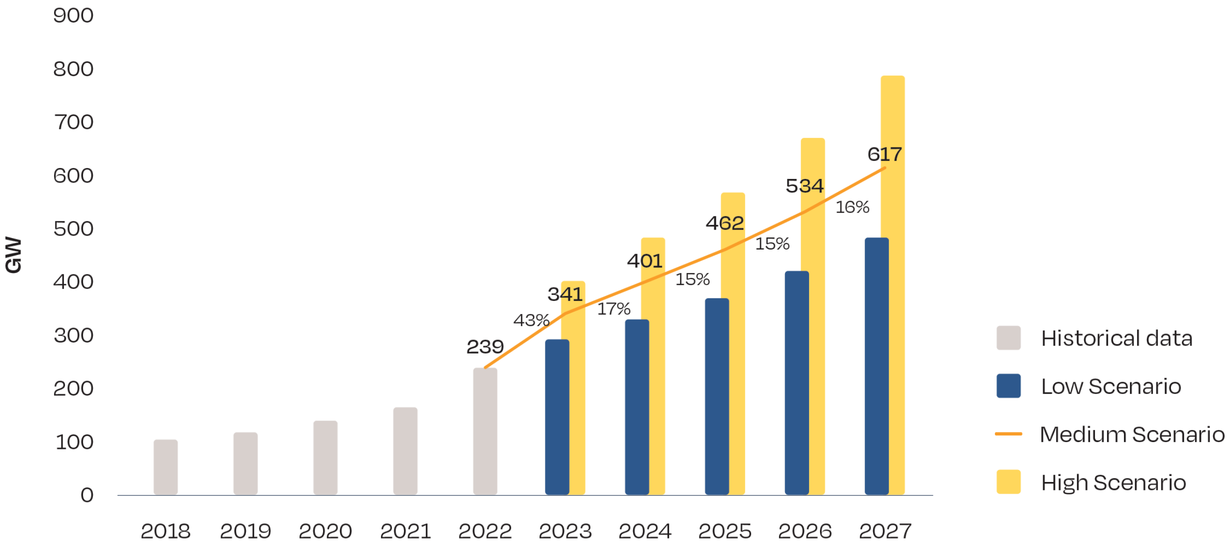

Figure 1.1: World annual solar PV market (installed capacity) scenarios 2023 - 2027 [3].

The substantial growth in solar photovoltaic (PV) capacity, coupled with substantial cost reductions observed over the last decade, has enabled solar PV to capture a significant market share and sustain its leadership role in the ongoing global energy transition [3], [4]. By 2027, the installed power capacity of solar PV will surpass that of coal and natural gas, solidifying its position as the world's largest power generation source [5]. This achievement further underscores the prominent role that solar PV is poised to play in shaping the global energy landscape.

1.2 SHJ solar cells

Silicon heterojunction (SHJ) solar cell technology is one of the most promising PV technologies because of its high power conversion efficiencies, simple fabrication process and low manufacturing cost [6]. The current world record efficiency of SHJ solar cell reaches up to 26.81%, with a fill factor of 86.1% and V_{OC} of 751.4 mV on M6 size industry-grade silicon wafers [7].

1.2.1 Development of SHJ solar cells

Figure 2.3 shows a schematic sketch of a front/back-contacted (FBC) SHJ solar cell. A c-Si wafer is sandwiched between a-Si:H layers. The a-Si:H layers consist of a stack of intrinsic and doped a-Si:H layers. The intrinsic a-Si:H layer is used to passivate the c-Si surfaces. The p-doped layer forms the hole contact and the n-doped a-Si:H layer forms the electron contact. TCO on the front side is deposited for lateral charge transport to the electrode, as well as forming an anti-reflection coating [6]. TCO on the back side is used to avoid metal diffusion as well as improve light management [8]. The metal contacts are formed at last to connect solar cells to external circuit. SHJ solar cells are made on n-type c-Si wafers because of their better chemical passivation with a-Si:H and better inherent electronic bulk quality, compared to p-type c-Si materials [8].

a-Si:H was first incorporated as a junction-formation material for c-Si wafers by Sanyo and reached 21.3% efficiency in 2003 [9], [10]. The low processing temperature of less than 200 °C, low-temperature coefficient, and high efficiency make SHJ solar cells attractive and the efficiency has grown rapidly to over 26% in two decades. Improvements are related to the use of new electron and hole transport layers [7], [11], [12], TCO materials [13], IBC configurations [14], and copper metallization [15].

1.2.2 Passivtaion layer of SHJ solar cells

The thin intrinsic hydrogenated amorphous silicon ((i)a-Si:H) layer is inserted between the doped thin film and the c-Si bulk to passivate the dangling bonds on heterojunction interfaces. It is crucial to guarantee high conversion efficiency [9]. The deposition condition of the (i)a-Si:H layers need to be controlled carefully to prevent epitaxial growth at the a-Si:H/c-Si interface.

A bilayer structure is an effective approach to attain good passivation. It consists of a void-rich (i)a-Si:H-1 (i1) interfacial layer deposited to suppress epitaxial crystallization, and a dense (i)a-Si:H-2 (i2) layer deposited in highly hydrogen-diluted plasma near the transition zone region [16]–[19]. The quality of surface passivation is found to correlate with microstructure factor R*, which is related to the Si-H bonds configurations of a-Si:H

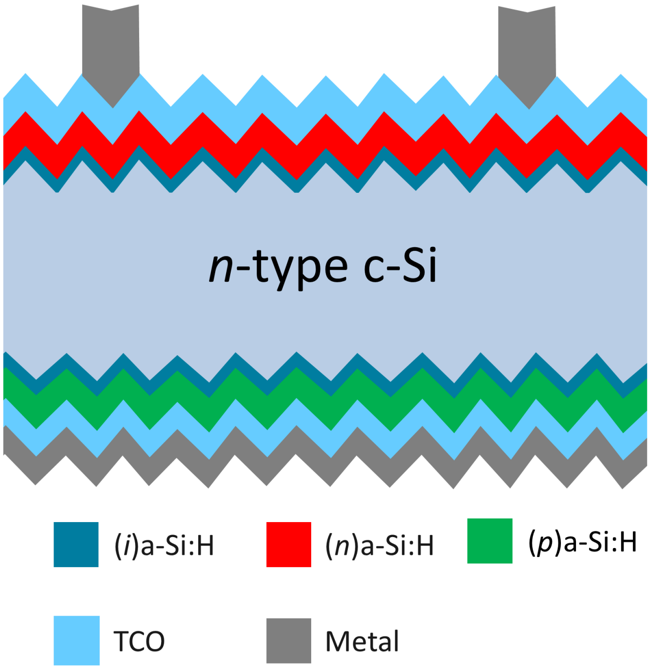

Figure 1.2: The schematic representation of a FBC-SHJ solar cell with (a)Si-H layers.

network. The properties of the (i)a-Si:H layers could be influenced by various process conditions, such as deposition power, pressure [20], [21], hydrogen dilution ratio [19], temperature [22], and hydrogen plasma treatment (HPT) [23], [24]. Furthermore, a variety of interfacial layers have also been investigated, such as intrinsic hydrogenated amorphous silicon oxide alloy ((i)a-SiO$_x$:H) [25], intrinsic amorphous silicon carbide ((i)a-SiC$_x$:H) [26], and ultra-thin oxides [27], [28].

1.3 Research goals

In achieving high-efficiency SHJ solar cells, it is critical to optimize the thin (i)a-Si:H passivating layers. Specifically, an optimized (i)a-Si:H layer (stack) should not only ensure an excellent c-Si surface passivation quality but also not being too resistive to hinder the transport of charge carriers [20]. Therefore, the main research goals of this thesis are:

1. Optimization of hydrogenated intrinsic amorphous silicon layers with good c-Si surface passivation.
    - Characterize the microstructure properties of (i)a-Si:H films with varied deposition conditions.
    - Study the role of layers composing the (i)a-Si:H bilayers in the performance of surface passivation.
    - Optimize the (i)a-Si:H bilayer structure with good passivation performance.

2. Optimization of (i)a-Si:H bilayer to fabricate high-efficiency FBC-SHJ solar cells.
    - Integrate the preliminarily optimized bilayer structure to FBC-SHJ solar cells to identify possible improvement directions to balance the carrier transport and passivation quality.
    - Study the role of layers composing the (i)a-Si:H bilayers in the performance of SHJ solar cells.
    - Further optimize the bilayer combination to achieve solar cells with high FF and V_{OC} solar cells, and therefore, high efficiency.

1.4 Thesis outline

In the first chapter, the advantage of SHJ solar cells has been stressed. Then passivating contact structures were introduced. Subsequently, the main research goals of this thesis have been given.

In Chapter 2 the recombination mechanism, and working principle of FBC solar cells are explained. Besides, the material properties, growth and passivation mechanism of a-Si:H are covered. Chapter 3 introduces the fabrication methods and characterization tools that are used in this thesis. Chapter 4 sets a database with microstructure properties of (i)a-Si:H films by varying their deposition conditions, and the surface passivation of bilayer (i)a-Si:H has been optimized. The optimized bilayer structure is then used to construct FBC-SHJ solar cells in Chapter 5. The effects of various (i)a-Si:H bilayers on the performance of SHJ solar cells are evaluated, especially, optimizing the balance between the surface passivation and carrier transport. Finally, in Chapter 6, the main results are summarized and concluded, and outlook for future research is given.

2 Fundamentals

In this chapter, the recombination mechanism and the working principle of FBC solar cells were explained. Besides, the material properties, growth and passivation mechanism of a-Si:H were covered.

2.1 Photovoltaic Fundamentals

2.1.1 Recombination mechanisms

When the energy of an incident light is equal to or greater than the band gap of the material, the photon is absorbed by the material and excites an electron from the valence band to the conduction band, while creating positively charged holes in the valence band. The excitation of electrons to the conduction band induced by photo absorption leads to a non-equilibrium state and when the excess electrons stabilize back into the valence band, it also removes a hole. This process is named recombination, and could be classified by bulk and surface recombination depending on where recombination happens.

Bulk recombination

Radiative recombination: In direct bandgap materials, such as gallium arsenide, radiative recombination is the dominant loss mechanism of charge carriers. As shown in Figure 2.1, during the process, the electron in the conduction band directly falls to the valence and recombines with a hole giving off the energy as a photon. Because the emitted photon has a similar energy to the band gap, it could only be weakly absorbed and it can leave the material without being absorbed again. Since crystalline silicon is an indirect band gap material, radiative recombination is not the dominant recombination mechanism for c-Si based solar cells.

Auger recombination: In indirect semiconductors, Auger recombination becomes important. As shown in Figure 2.1, Auger recombination is a three-particle process. In Auger recombination, the momentum and energy of the recombination is transferred to a third particle, an electron in the conduction band in this illustration. The electron is excited to higher levels in the electronic band and falls back to the conduction band edge by releasing energy to phonon mode. Auger recombination is most important with high doping concentration and injection level [29]. In the c-Si solar cells, Auger recombination limits the lifetime and ultimate efficiency.

Shockley-Read-Hall recombination: As shown in Figure 2.1, in Shockley-Read-Hall (RSH) recombination, an electron can be trapped at lattice defects and consequently recombines with a hole that is attracted by the trapped electron. The excess energy is dissipated into the lattice by heat.

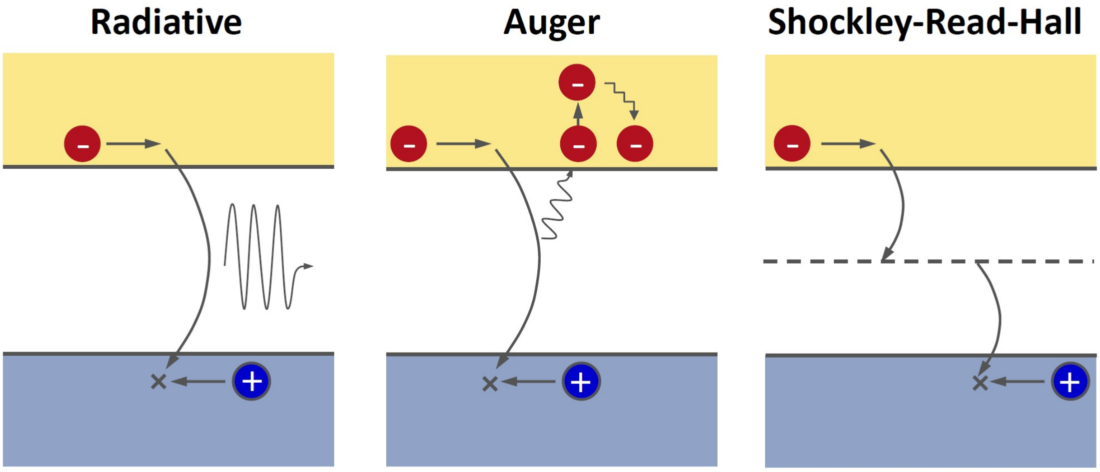

Figure 2.1: Schematic representations of three recombination mechanisms: Radiative recombination, Auger recombination and SRH recombination [29].

Surface recombination

As shown in Figure 2.2, at the silicon surface, dangling bond forms as a defect, where valence electrons on the surface cannot find a partner to create a covalent bond. These defects create surface trap states and induce SRH recombination. To minimize the surface recombination loss, the trap density could be reduced by depositing a thin layer on the surface for the valence electrons on the surface to form covalent bonds, which is called passivation.

Effective minority carrier lifetime

Effective minority carrier lifetime (τ_{eff}) is described as the average time before minority carriers recombine with the corresponding majority carriers in a material. It can be expressed as an expansion of bulk recombination and surface recombination added up, as in Equation 2.1:

$$\frac{1}{\tau_{eff}} = \frac{1}{\tau_{bulk}} + \frac{1}{\tau_{surface}} \tag{2.1}$$

where τ_{bulk} and $\tau_{surface}$ indicates the lifetime of bulk and surface.

In the used FZ c-Si wafer, the lifetime of the bulk is high, then Equation 2.1 could be expressed as Equation 2.2 in below:

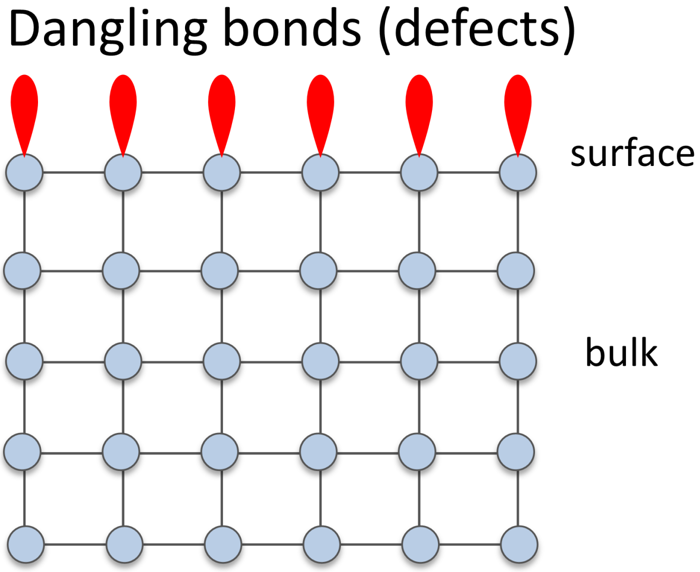

Figure 2.2: Schematic representation of dangling bonds at c-Si surface.

$$\frac{1}{\tau_{eff}} \approx \frac{1}{\tau_{surface}} \tag{2.2}$$

Therefore, the effective lifetime can directly reflect the passivation of the interface, which will be used in Section 4.2.

2.1.2 Working principle of SHJ solar cells

The electronic band diagram of n-type SHJ solar cell under thermal equilibrium is shown in Figure 2.3. Because of the different band gap of a-Si:H (E_G = 1.6 - 1.8 eV) and c-Si (E_G = 1.12 eV), the offsets are presented between the conduction bands and valence bands of the a-Si:H and c-Si:H. The minority carriers (holes) are collected at the p-side contact, and the majority carriers (electrons) are collected at the n-side contact. The holes can drift through narrow energy barriers by tunneling, trap-assisted tunneling and/or thermionic emission into the p-side electrode and collected [30]. On the n side, the large valence band offset shield holes to recombine with electrons, indicating that band bending and offset could reduce the recombination [31]. This is the reason why the intrinsic layer should be thin to allow tunneling of the minority carriers through, and p-type and n-type layers that are heavily doped [32]. While (i)a-Si:H passivate the surface, band bending induced by doped layers has a beneficial influence on charge carrier transport across the c-Si/(i)a-Si:H intersurface. The recombination losses are suppressed and a high V_{OC} can be achieved [33].

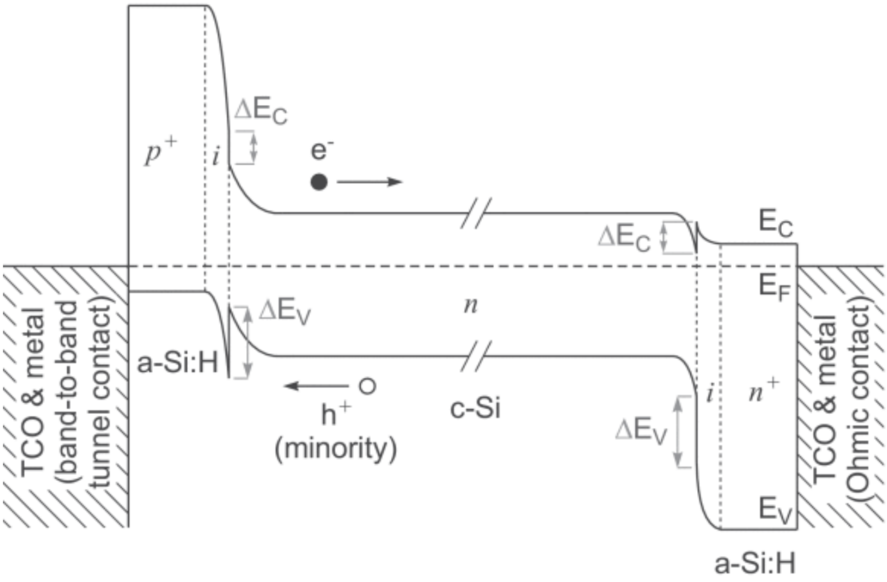

Figure 2.3: The electronic band diagram of n-type SHJ solar cell under dark and thermal equilibrium [34].

2.2 Hydrogenated Amorphous Silicon

2.2.1 Atomic Structure

Crystalline silicon (c-Si) is tetrahedrally bonded to four neighboring silicon atoms and forms a continuous crystalline lattice as shown in Figure 2.4. The bonding angles and lengths are the same, and have hardly any defects. For a-Si, in short-range order, most silicon atoms still have bonds to four neighboring silicon atoms. However, for a-Si, the small deviations in bonding angles and lengths between neighboring atoms lead to a continuous random network. As shown in Figure 2.4(c), some silicon orbitals do not form bonds with other atoms, while some form bonds with atomic hydrogen [35]–[37].

In a-Si:H, hydrides are incorporated into Si bulk as a variety of configurations, such as monovacancy, divacacy, trivacancy, 2 monovacancies, 6-ring void, platelet and nanosized voids. Fourier Transform Infrared Spectroscopy (FTIR) is can be used to determinate microstructure of the hydrides in a-Si:H film [38], which will be discussed in Section 3.3.3.

2.2.2 Growth Mechanisms

The a-Si:H films are deposited in plasma enhanced chemical vapor deposition (PECVD) tool, which is discussed in Section 3.2.1. The reactions between high energy electron and SiH_4 molecules can be reacted by different types and create a variety of plasma species, such as radicals, ions, large clusters. The radicals are mainly dominant by SiH_3 radicals diffuse through the sheath region toward the substrate and participate in film growth [30]. The growth reaction with SiH_3 radicals on H terminated c-Si surface is

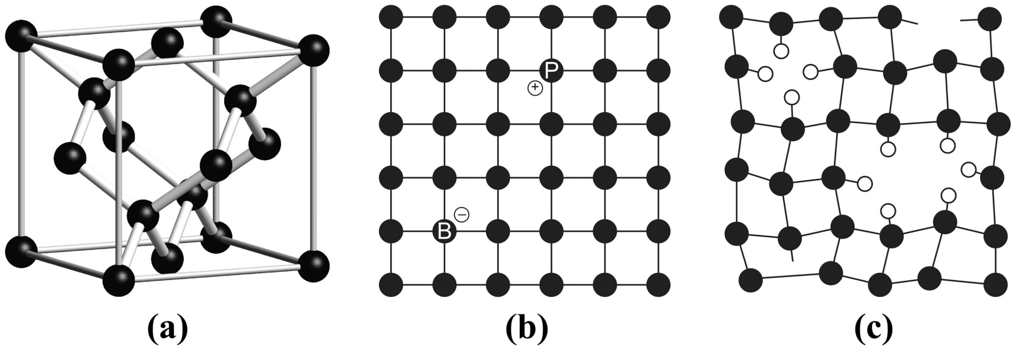

Figure 2.4: Representation of the crystallographic unit cell of c-Si, substitutional phosphorus and boron doping of c-Si, the a-Si:H with hydrogen saturated dangling bonds (empty circles) and unsaturated dangling bonds [36].

shown in Figure 2.5 in the condition of low power and low pressure (< 10 Pa, < 10 mW/cm^2). At high pressure and power conditions, the SiH$_{x\leq 2}$ radicals dominate in film growth. It could format higher cluster silane modules that contributed to Si-H$_2$ bonding configuration [39].

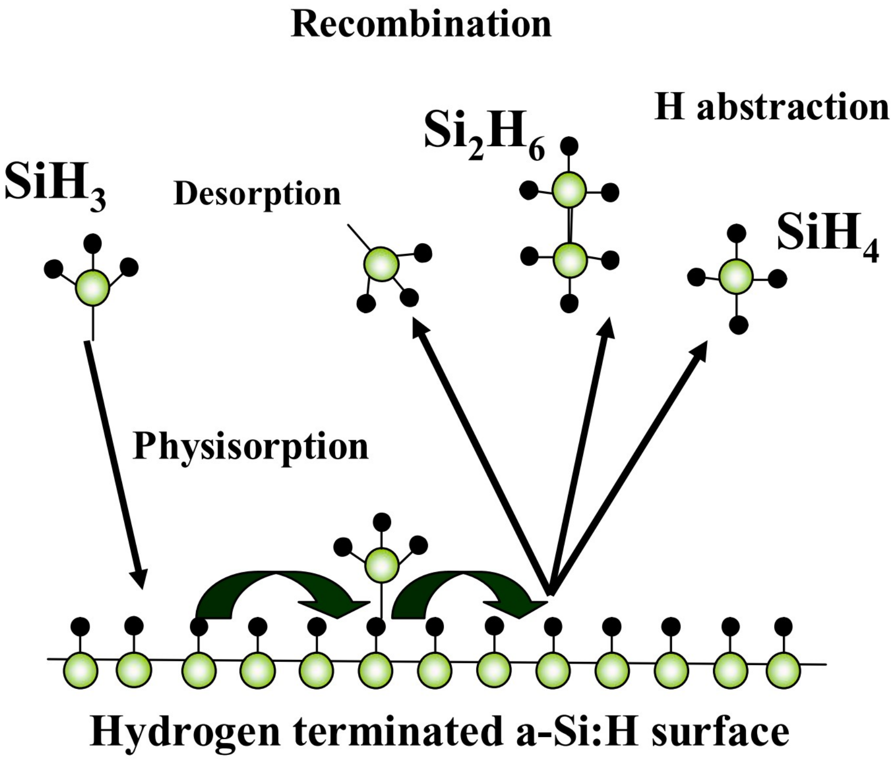

Figure 2.5: Standard view for the deposition of device quality a-Si:H thin films based on the interaction of SiH$_3$ radicals with a hydrogen terminated silicon surface [30].

2.2.3 Passivation Mechanisms

The mechanism illustration of the passivation of dangling bonds at the c-Si surface is shown in Figure 2.6. Without surface passivation, the dangling bonds act as recombination centers to trap electrons, resulting in a high rate of SRH recombination at the a-Si:H/c-Si interface. These dangling bonds can be passivated by H atoms to reduce the rate of SRH recombination [40]. Therefore, H content in the (i)a-Si:H layer is important in the c-Si surface passivation.

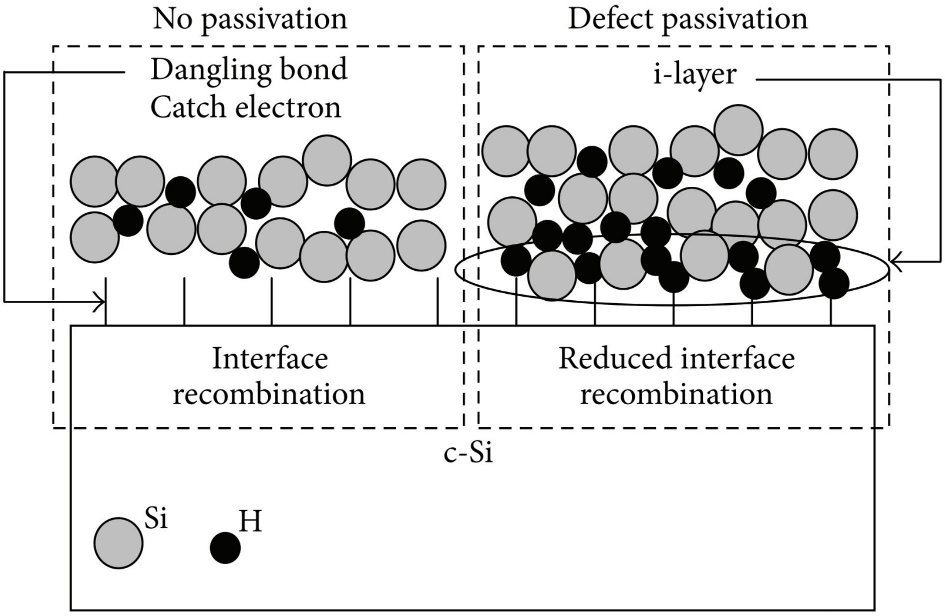

Figure 2.6: Scheme of the mechanism of surface passivation on c-Si [40].

3 Experiment instruments and methods

In this chapter, the experiment methods and instruments for fabricating and the measurement tools were introduced.

3.1 Wet chemical treatment methods

Two types of Wafers were used in this thesis. The wafers with the orientation of (100) were textured into (111) and cleaned before deposition.

- For passivation test and cell fabrication: Double-side polished 4″ Float Zone (FZ) N type Topsil wafers, with (100) orientation, thickness $280 \pm 20\,\mu\mathrm{m}$ and resistivity $3 \pm 2\Omega \cdot \mathrm{cm}$;
- For FTIR measurement: Single-side polished 4″ Czochralski (CZ) N type Siegert wafers, with (100) orientation, thickness $525 \pm 20\,\mu\mathrm{m}$ and resistivity $10 \pm 5\Omega \cdot \mathrm{cm}$;

3.1.1 Texturing process

In order to improve the efficiency of the solar cells, both the front and the rear sides of the wafers were textured. As the incident light beam passed through the textured surface, a part of the light will be reflected to another textured surface and partially transmitted through the surface once again [29]. In addition, the textured surfaces scatter the incident light, effectively increasing the average optical path length through the absorber layer [41]. This process helps reduce surface reflections and absorption is increased, thus improving J_{SC}.

The texturing method uses a alkaline solution anisotropic etching. Due to different etching rates between (100) and (111) surfaces, the (100) surfaces are etched away more rapidly, while (111) surfaces remain, resulting in the morphology of random pyramids [30].

In this thesis, wafers were textured by using 5% tetramethylammonium hydroxide (TMAH, $(CH_3)_4NOH$) hot solution (85-90°C, 100 rpm stir speed). The resulting size of pyramids were ranging from approximately 1-6 µm [13]. The TMAH solution consisted of 1L 25wt.% TMAH (SIGMA-ALDTICH), 4L deionized water (DI water) and 120 ml of ALKA-TEX.8 (ISRA) as an additive. ALKA-TEX.8 was used to increase the reaction speed and extending the lifetime of the solution. While heating up the solution, a clean wafer is put inside for activating the texturing solution. During the texturing, wafers were immersed in the hot solution for 15 min and rinsed in DI water for 5 min. After drying, the textured wafers were dipped into a 40°C acetone bath for 3 min to remove any organic residues prior to standard cleaning. After texturing, the thickness for N-type Tosil wafers was around 260 µm.

3.1.2 Cleaning procedure

Cleaning for Wafers

Although textured wafers enhance light-trapping properties, the interface area between a-Si:H and c-Si is increased and leads to high interface defect densities, which could increase the recombination losses and thus lower V_{oc}. Therefore, removing particles and metallic contamination at the textured Si surface becomes crucial. In this thesis, Nitric Acid Oxidation Cycle (NAOC) cleaning has been used as a pre-deposition cleaning procedure.

One standard NAOC consists of 10 min soaking in 99% room-temperature HNO_3 bath to remove mainly organic residues, 10 min soaking in 110°C 69.5% HNO_3 bath to remove mainly metallic residues, and 5 min soaking in 0.55% hydrofluoric acid (HF) bath to strip off silicon oxide layer. 5 min of deionized water rinsing is used after each step. It is suggested to repeat NAOC 3 times to remove contamination and nano-roughness on the facet of the pyramidal structures after texturing [42].

Finally, Marangoni (0.55% HF) process is used before loading wafers into the vacuum chamber to strip off the formation of the native oxide layer and terminate the crystalline silicon surface with hydrogen [43], [44].

Cleaning for glass

The 4″ glass substrate used in this thesis is cleaned sequentially in ultrasonic baths containing acetone and isopropanol for 10 min each.

3.2 Manufacture tools

3.2.1 Plasma-enhanced chemical vapor deposition

In this thesis, all silicon layers were deposited on the c-Si substrate using Plasma-enhanced chemical vapor deposition (PECVD), named AMIGO (Elettrorava, S.p.A.). The schematic of a PECVD reaction chamber is shown in Figure 3.1a. The top view of AMIGO with multiple chambers is shown in Figure 3.1b.

As shown in Figure 3.1a, the temperature of the substrate is controlled by heating elements to 160 or 180 °C. Working gas input and pumping are performed from the side. The sample is mounted face down on a sample holder that serves as the ground

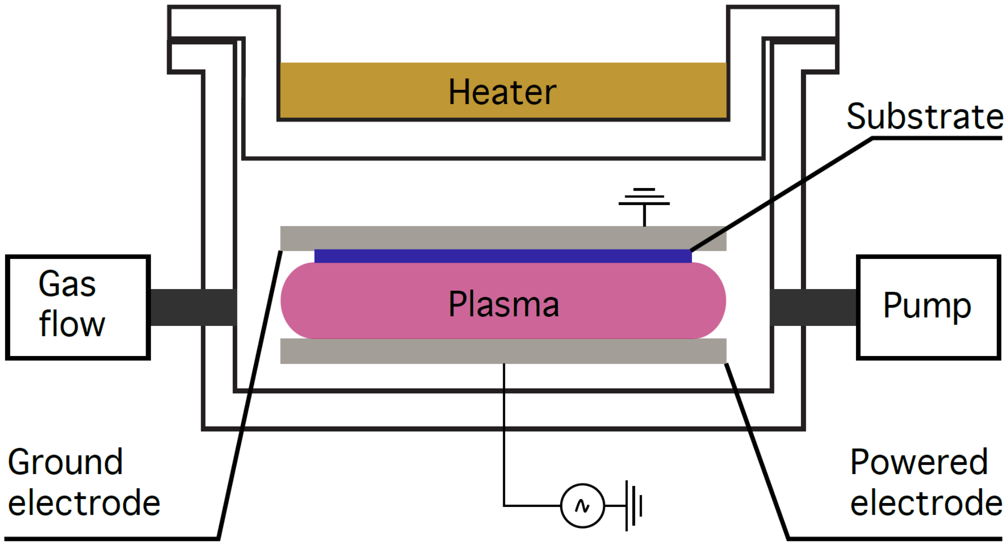

(a)

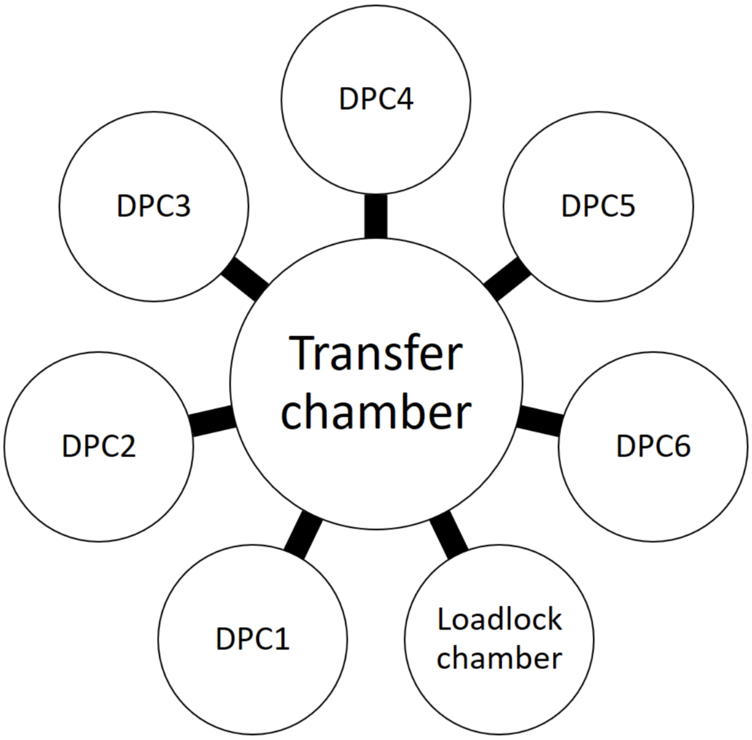

(b)

Figure 3.1: Schematic representation of (a) a PECVD reaction chamber [45], and (b) the top-view of the AMIGO PECVD (Elettrorava, S.p.A.) with six deposition chambers [46].

electrode. A radio frequency (rf, 13.56 MHz) or very high frequency (VHF, 40.36 MHz) power supply is capacitively coupled through a matchbox to the parallel electrodes and the plasma is ignited. After plasma ignition, precusor gas collides with high-energy electrons, dissociated into a variety of plasma species, such as radicals, ions and clusters, interacting with the substrate and growing films [30].

In AMIGO PECVD cluster tool, as in Figure 3.1b, the sample is loaded in the loadlock chamber (LLC). By using a robot arm, the sample could be transferred through transfer chamber (TC) into different deposition chambers (DPCs), which are used for the deposition of different layers. The reason for using different DPCs is to avoid cross-contamination. Various precursor gas mixtures are supplied into DPCs to form different materials, allowing the growth of i/n or i/p stacks of FBC-SHJ solar cells. In this thesis, DPCs from 1 to 4 are used. DPC1 and DPC2 are used for p-type dopant and n-type dopant layers, respectively, while DPC3 is used to deposit intronic (a)-Si:H. DPC4 is VHF chamber.

Table 3.1: Deposition parameters of layers deposited with AMIGO PECVD (Eletrrorava, S.p.A.).

Layer	DPC	SiH_4 (sccm)	B_2H_6 (sccm)	PH_3 (sccm)	H_2 (sccm)	CO_2 (sccm)	Pressure (mbar)	Power (W)	$T_{substrate}$ (°C)
(i1)a-Si:H	DPC1	40	-	-	-	-	0.7	3	160
(i2)a-Si:H	DPC1	10	-	-	-	-	1.4	3	160
HPT (p-side)	DPC1	0	0	-	200	0	2.2	9	180
HPT (n-side)	DPC2	0	-	0	200	0	2.7	9	180
(p)nc-SiO_x:H	DPC1	0.8	10	-	170	1.4	2.2	11	180
(p)nc-Si:H	DPC1	0.8	10	-	170	0	2.2	13	180
(n)nc-Si:H	DPC2	1	-	1.2	100	0	2.7	11	180
(n)a-Si:H	DPC2	40	-	11	0	0	0.6	4	180
VHF	DPC4	1.2	-	-	120	-	4.0	13	180

3.2.2 Radio frequency magnetron sputtering

Radio frequency magnetron sputtering is a physical vapor deposition (PVD) method for depositing transparent conductive oxide (TCO) after the deposition of intrinsic and doped layers in PECVD. The schematic process of a magnetron sputtering is shown in Figure 3.2. The principle of magnetron sputtering is momentum exchange between high energy iterate with a plasma of an inert gas, and the atoms in the target. Therefore, the material is ejected and deposited on the substrate [47].

The magnetron sputtering used in this thesis is ZORRO manufactured by Polyteknik AS. ITO films were deposited at room temperature from a target containing 90 wt% In_2O_3 and 10 wt% SnO_2 [13]. The chamber was evacuated to a base pressure below 1×10^{-7} mbar before the deposition to eliminate the contribution of the water during the processing. Post-deposition annealing at 180 °C for 5 minutes was performed in the air to recover /mitigate sputter damage [48].

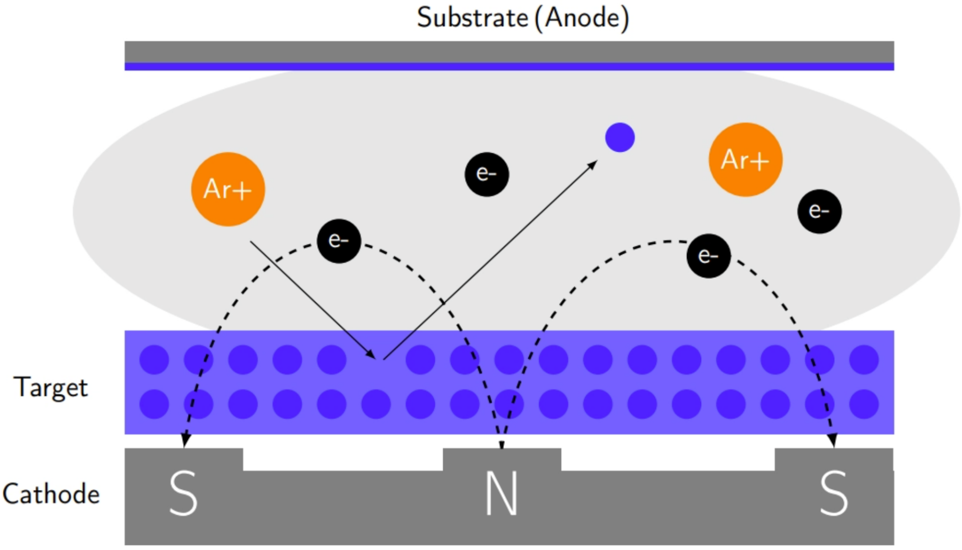

Figure 3.2: Schematic process of a magnetron sputtering [47].

3.2.3 Metal Evaporation

For the deposition of the Ag as the seed layer and back metal contact in SHJ solar cells, as well as SiO_x as an anti-reflection coating, evaporation based on physical vapor deposition is used. Figure 3.3 shows a schematic structure of the Provac PRO500S, which is equipped with two different energy sources for material evaporation: e-beam evaporation and thermal evaporation. The source material is evaporated in a vacuum chamber. The vacuum allows vapor particles to travel directly to the substrates rotating on the top of the processing chamber, where they condense back to a solid state. For thermal evaporation, the tungsten boat serves as a resistor, heating up and melting the material inside with applied high voltage. For electron-beam evaporation, electrons are generated by thermal emission and attained enough kinetic energy to melt the material when hitting the crucible [45]. In this thesis, Ag is deposited by thermal evaporation, and SiO_x is deposited by e-beam evaporation, based on their distinct melting temperatures.

3.2.4 Photolithography

In this thesis, photolithography is used for patterning the front metal grids, the schematic illustration of photolithography process is shown in Figure 3.4 [50]. The sample is coated uniformly with AZ ECI 3027 positive photoresist through spinning three times forming a thickness of around 12 µm. To obtain good adhesion of photoresist on the wafer, it is baked in an oven at 100 °C for 2 min, 3 min and 5 min, respectively. Then, the sample is aligned with desired patterned mask and the uncovered area is exposed to UV light with SUSS MicroTec MA/BA8 mask aligner for 100 s. Since the light will weaken the positive resist, the uncovered area is dissolved by alkaline developer Microposit^{TM} MF-322 for 120 s. Therefore, the grid patterning is opened up for Cu plating, leaving the rest protected

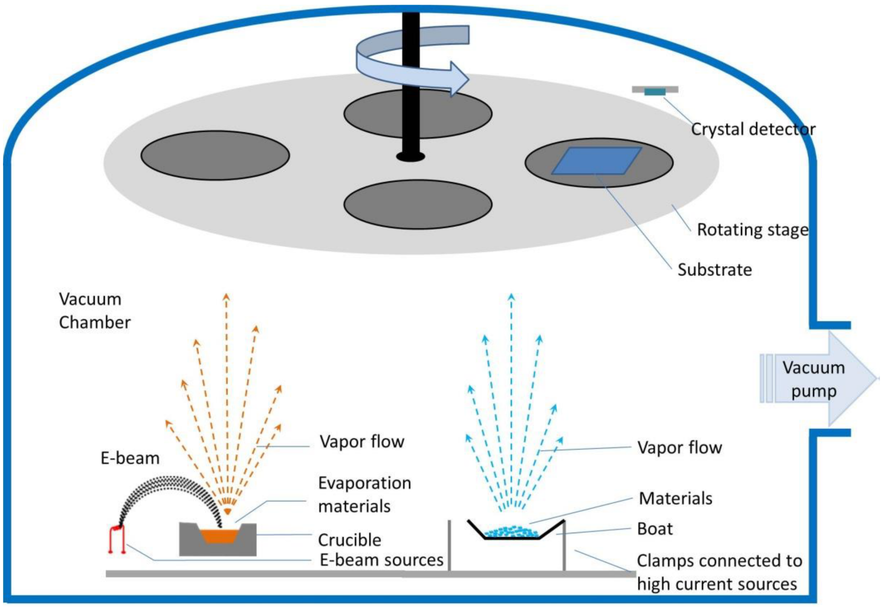

Figure 3.3: A schematic structure of the metal evaporation deposition system Provac PRO500S. Electron-beam (E-beam) and thermal evaporation are shown on the left and right side, respectively [49].

by the photoresist. The photolithography process was finished in polymer lab of EKL, which is lightened with yellow light to avoid photoreaction of photoresist.

3.2.5 Cu plating

Metallization is the final step in solar cell fabrication, which greatly affects the performance of solar cells. The state of the art of metallization technology uses screen printing of silver pastes to make metal contacts [51]. To enable an over 3 TW solar market by 2030, the main concern is the supply and cost of silver. Therefore, the development of alternative materials is needed [8]. Electroplating of Cu is becoming more attractive than the method of screen-printing of low-temperature Ag-pastes, mainly because of its low cost and abundance, high conductivity, and high potential aspect ratio [52].

Figure 3.5 shows the schematic three-electrode configuration of copper electroplating process, which consists of a working electrode (WE), counter electrode (CE) and reference electrode (RE) [53]. The Ag/AgCl reference electrode has a constant electrochemical potential, all voltages are reported with the reference of RE [54]. The probe is connected to the working electrode contacted with the exposed Ag seed layer on the wafer. By sinking the wafer in an electrolyte bath (which consists of $CuSO_4$ and Sulfuric acid), copper ions flow and deposit on the Ag seed layer. Levelers polarize the areas with high current densities and even out current distribution, and help control the surface morphology [55].

To improve the finger height uniformity and adhesion, electroplating uses a 2-step deposition approach: potentiostatic process (0.35 V, 30 s) and galvanostatic process (-0.4

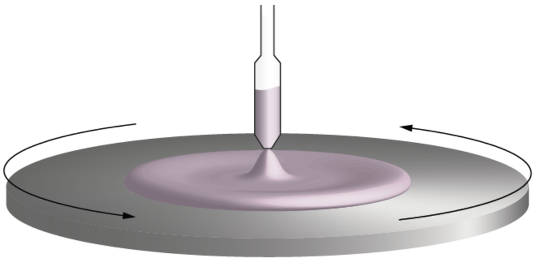

(a) Step 1: spin coating.

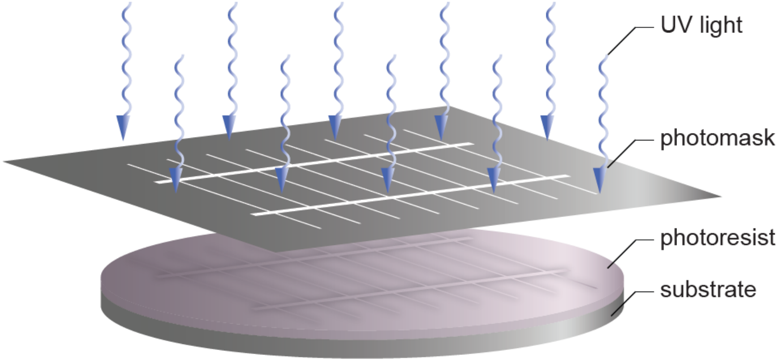

(b) Step 2: exposure.

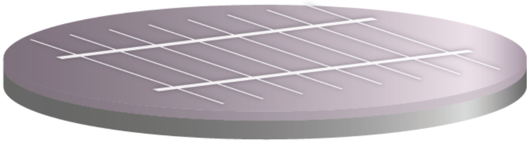

(c) Step 3: development.

Figure 3.4: Schematic process of photolithography with the use of a positive photoresist [50].

A, 10 min). After the electroplating process, the photoresist is removed by acetone. The Ag seed layer on the outside of the grid pattern is lifted off via a mixed fresh solution, which consists of 2400 mL DI H_2O + 200 mL NH_4OH (28%) + 800 mL H_2O_2 (31%). The height of the Cu finger is approximately 26 μm [54].

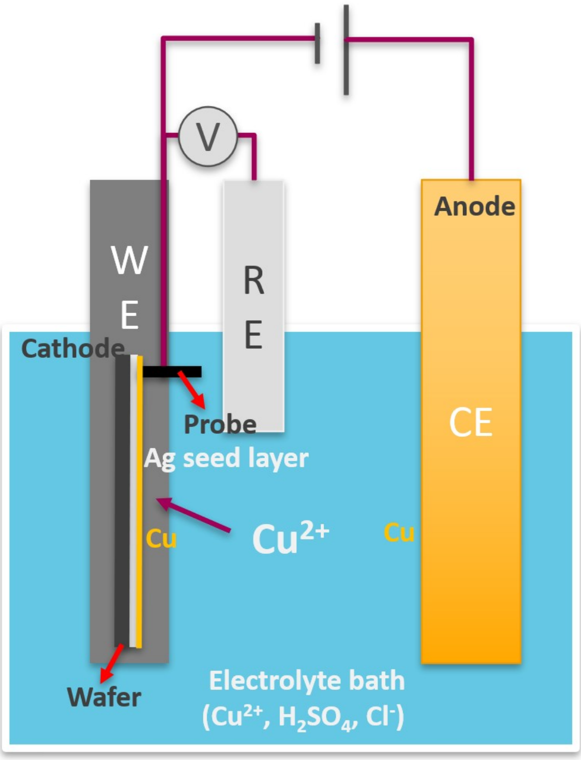

Figure 3.5: Schematic configuration of Cu-plating processes.

3.3 Measurement tools

3.3.1 Spectroscopic Ellipsometry

In this thesis, spectroscopic ellipsometry by J.A. Woollam Co., M-2000DI is used for thickness measurements of deposited (i)a-Si:H films and ITO films. The schematic sketch of SE is shown in Figure 3.6. When a linearly polarized light is reflected by a thin film sample on the stage, the polarization state is measured. Amplitude and phase are obtained in different angles of incidence and wavelength, which could describe the change in polarization of reflected light.

In this thesis, the thickness of the deposition layer could not be directly determined on textured wafers, because randomly textured wafers feature high roughness that induces significant uncertainty when fitting thickness in SE. Instead, the deposition thickness is tested on the flat glass samples. Therefore, the deposition thickness on the wafer is assumed to be 1.7 times thicker considering the angle of the pyramid structure.

3.3.2 Photoconductance lifetime tester(Sinton)

In this thesis, a photoconductance lifetime tester (Sinton WCT-120) is used to characterize the passivation results of layers, as well as that of solar cell precursors. Figure 3.7 shows the schematic representation of the Sinton setup.

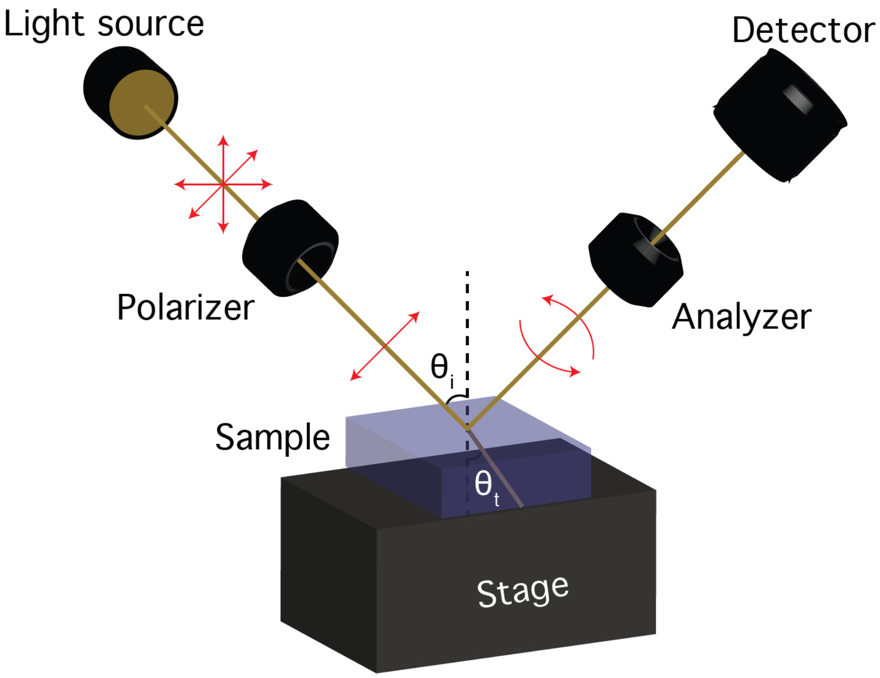

Figure 3.6: Schematic representation of the spectroscopic ellipsometry measurement setup [45].

The sample is placed on a stage, where the RF coil beneath the sample senses the change in conductance in the wafer. the sample is then illuminated by IR flashlight, changes in the photoconductance of the sample are used to determine τ_{eff} in Equation 3.1 [39], [45]:

$$\tau_{eff} = \frac{\Delta p}{G(t) - \frac{\delta \Delta p}{\delta t}} \tag{3.1}$$

where G is the carrier generation rate and it is calculated from the photodiode. For QSSPC mode ($< 200\,\mu\text{s}$), $\frac{\delta \Delta p}{\delta t}$ is neglected because $G \gg \frac{\delta \Delta p}{\delta t}$ and for transient mode ($> 200\,\mu\text{s}$), G is almost zero.

Implied open-circuit voltage (iV$_{OC}$) could be determined based on measured τ_{eff} and Δp data, as in Equation 3.2:

$$iV_{oc} = \frac{kT}{q} \ln\left(\frac{\Delta p(N_D + \Delta p)}{n_i^2}\right) \tag{3.2}$$

During this thesis, lifetime measurements of solar cell precusors have been performed after PECVD, ITO deposition, and annealing to ensure good tracking of passivation quality during the fabrication of solar cells.

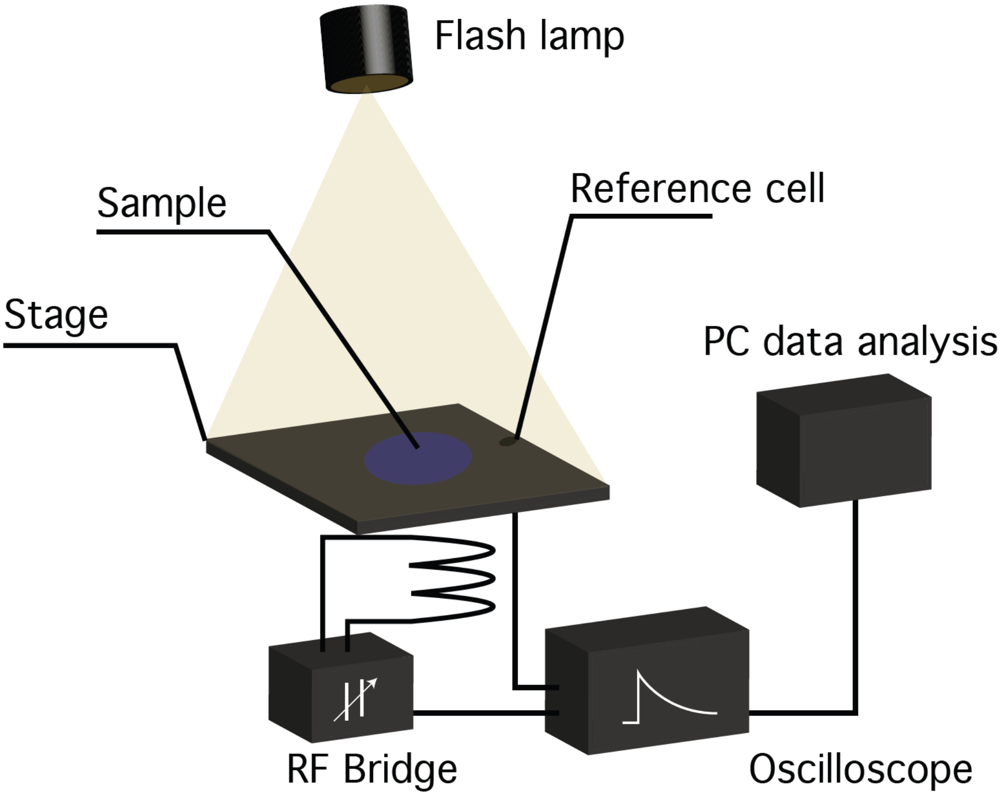

Figure 3.7: Schematic representation of the photoconductance decay measurement setup [45].

3.3.3 Fourier Transform Infrared (FTIR) Spectroscopy

Fourier transform infrared (FTIR) spectrometry is used to analyze silicon-hydrogen bonding configurations of a-Si:H films based on different vibration modes at different infrared wavenumbers. In this thesis, Thermo Scientific Nicolet 5700 FTIR spectrometer in transmission mode has been used.

The main component of the FTIR spectrometer is a Michelson interferometer. It consists of one beam splitter, one fixed mirror and one moving mirror, as shown in Figure 3.8. The incoming infrared beam is split into two halves at the beamsplitter, reflected off the mirrors, and then recombined at the beamsplitter again [56]. The optical path difference between the fixed and the movable mirror results in interference light. As it passes through the sample, certain frequencies of light could trigger the vibration of specific molecular modes or chemical bondings and be absorbed, then the rest of the transmitted light signal is measured by the detector. The interferogram records the response of the detector at each interval of the moving mirror position. Through Fourier transformation, this time-domain spectrum is converted into a frequency-domain spectrum, which shows the transmittance intensity against frequency [57], [58].

The infrared spectrum of a-Si:H consists of three absorption regions: wagging mode, bending scissor modes, and two stretching modes. The corresponding absorption regions

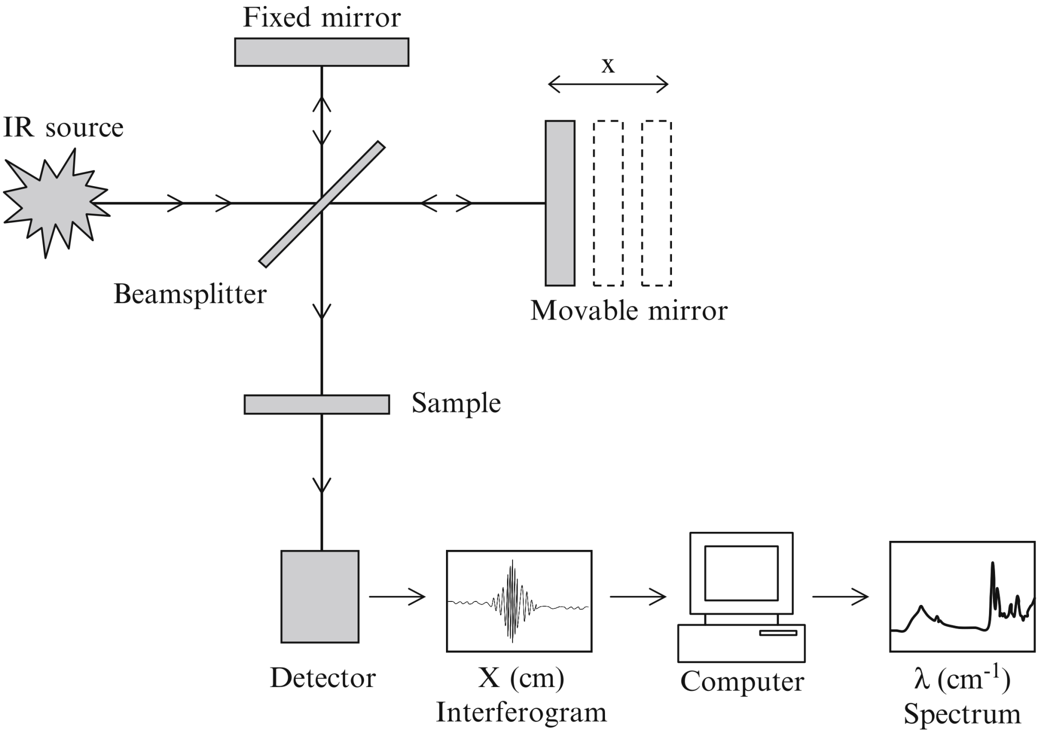

Figure 3.8: Schematic sketch of a FTIR spectrometer [56].

and related vibration modes are listed in Table 3.2.

Table 3.2: Corresponding relations between specified absorptions regions and vibration modes [59]–[61].

Absorption regions (wavenumber [cm^{-1}])	Vibrational modes
640	Si-H wagging mode
840-890	dihydride bending or scissors modes
2000	monohydrides stretching mode (LSM)
2090	clustered monohydrides and polyhydrides stretching mode (HSM)

The transmittance spectra could be converted into absorption spectra through Lambert–Beer's law in Equation 3.3:

$$\alpha^* = -\frac{lnT}{t} \tag{3.3}$$

where T is the transmittance in the function of wavenumber (ω) obtained from the FITR measurement, t is the effective thickness of the film, α^* is the effective absorption coefficient.

The integrated absorbance strength I could be calculated by Equation 3.4. the concentration of C_H, which is proportional to absorbance strength by the stretching modes, could be calculated in Equation 3.5 [62].

$$I = \int \left(\frac{\alpha^*}{\omega} \right) d\omega \tag{3.4}$$

$$C_H = \frac{P_C}{N_{Si}} \int \frac{\alpha\left(\omega\right)}{\omega} d\omega = \frac{1}{N_{Si}} \left(P_{C,LSM} I_{LSM} + P_{C,HSM} I_{HSM} \right) \tag{3.5}$$

where P_C represents a proportionality constant for HSM and LSM obtained by experimental, N_{Si} is the atomic density of a-Si:H films, $P_{C,LSM} = 9.0 \times 10^{19} cm^{-2}$, $P_{C,HSM} = 2.2 \times 10^{20} cm^{-2}$, $N_{Si} = 5.0 \times 10^{22} cm^{-3}$.

Apart from extracting hydrogen content, the microstructure factor R^* could be obtained from the absorption ratios between HSM and LSM. It is calculated by Equation 3.6 [63]:

$$R^* = \frac{I_{HSM}}{I_{HSM} + I_{LSM}} \tag{3.6}$$

where I_{HSM} and I_{LSM} are the absorption intensities of HSM and LSM in the IR absorption spectra, respectively. A higher R* means an underdense a-Si:H film with a higher density of dihydride bonds and nano-sized voids.

3.3.4 Current-Voltage measurement

In this thesis, the performances of the solar cells are tested with a AAA class Wacom WXS-90S-L2 solar simulator. The tests are performed under standard test conditions (STC), which is characterized by an irradiance of 1000 W/m^2, an AM 1.5 spectrum and solar cell temperature of 25°C [29]. The illustration of the current-voltage measurement setup is shown in Figure 3.9. AM 1.5 solar spectrum is simulated with a halogen and a xenon lamp. A temperature controlled stage is used where the solar cell is placed. The solar cell is measured by a four-point probe technique. Before measurement, two calibrated reference solar cells are used for calibration of the simulated spectrum.

An example of the measured J-V curve is shown in Figure 3.10, where open-circuit voltage (V$_{OC}$), short-circuit current density (J$_{SC}$), fill factor (FF) and efficiency (η) can be extracted. MPP stands for maximum power point. Shunt and series resistance (R$_{SH}$ and R$_S$) can be determined based on the slope of the J-V curve of J$_{SC}$ and V$_{OC}$, respectively, which could influence the FF. In this thesis, there R$_{SH}$ is really high and no shunt happens, while R$_S$ is the crucial limitation to FF.

3.3.5 SunsVoc

The J$_{SC}$ obtained from Wacom is used as an input for SunsVoc measurement. Since only voltage is measured with various illumination intensities. SunsVoc setup uses a flash lamp with a slow decay to provide a pseudo I-V curve that has no effect on the series resistance. The obtained SunsVoc is a function of illumination level, which gives a hint of

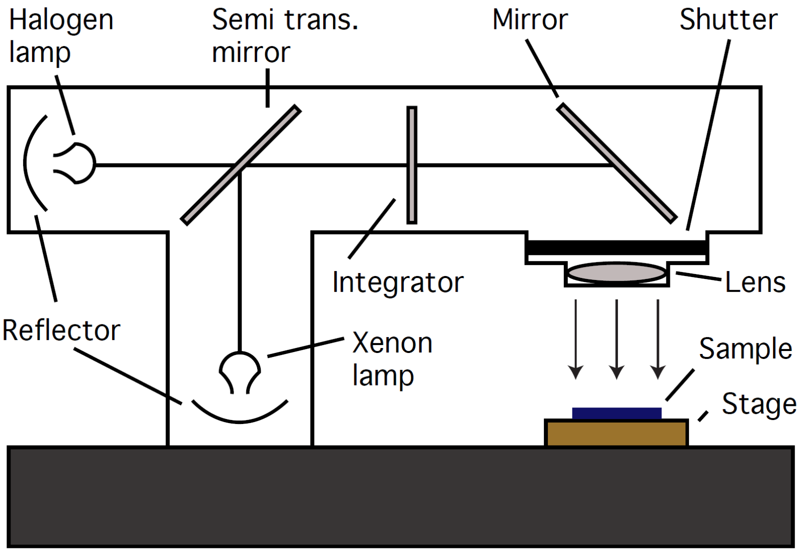

Figure 3.9: Illustration of the current-voltage measurement setup [45].

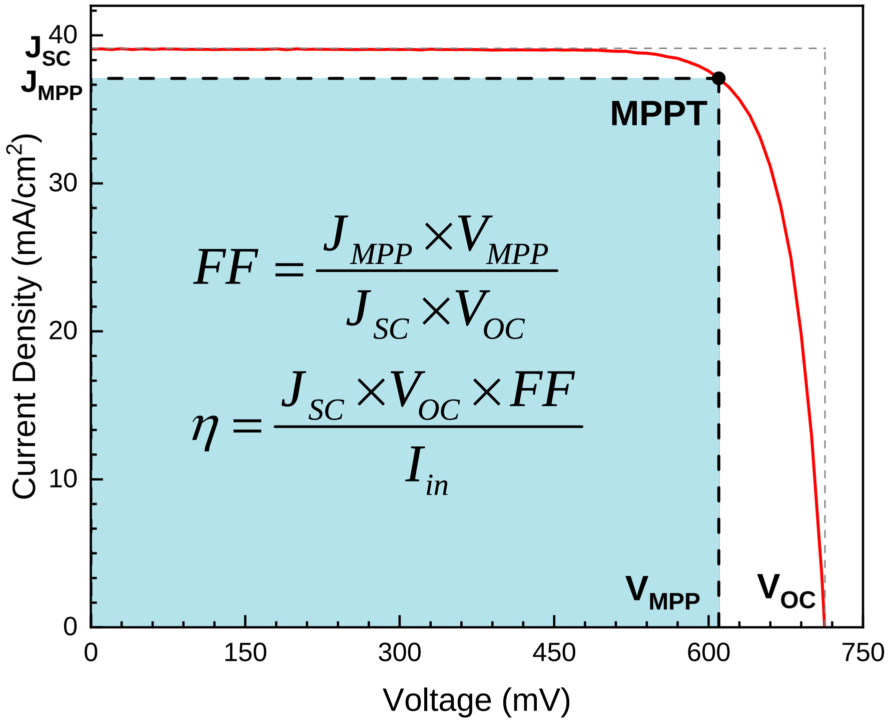

Figure 3.10: An example of the measured J-V curve with the definition of fill factor and efficiency.

the upper limit of Voc that can be measured from Wacom [64]. By comparing J-V curve and pseudo J-V curve, series resistance could be calculated by [65]:

$$R_s = (pFF - FF)\, V_{oc} J_{sc} / J_{mpp}^2 \tag{3.7}$$

where J_{mpp} is current at the maximum power point.

3.3.6 External quantum efficiency(EQE)

The external quantum efficiency EQE is the fraction of photons incident on the solar cell that creates electron-hole pairs in the absorber which are successfully collected. It is measured by illuminating the solar cell with monochromatic light of wavelength λ and measuring the photocurrent $I_{ph}(\lambda)$ through the solar cell, as shown in Equation 3.8 [29]:

$$EQE(\lambda) = \frac{I_{ph}(\lambda)}{q\Psi_{ph,\lambda}} \tag{3.8}$$

where q is the elementary charge and $\Psi_{ph,\lambda}$ is the spectral photon flow incident on the solar cell.

In this thesis, a home-built EQE measurement system (spectral response setup) is used. Light from a broad-emitting xenon lamp is converted into monochromatic, chopped light. Then it is used to generate photocurrent in the cell that is amplified and detected with the help of a lock-in amplifier, converting it into voltage and reading to the computer [29], [39].

Since $\Psi_{ph,\lambda}$ is obtained by a calibrated photodiode, the EQE measurement of the compared solar cells should be taken with the same calibration. The J_{SC} could be determined by integration in Equation 3.9 and Equation 3.10:

$$J_{SC} = -q \int_{\lambda 1}^{\lambda 2} EQE(\lambda) \Phi_{ph,\lambda}^{AM1.5} d\lambda \tag{3.9}$$

$$\Phi_{ph,\lambda}^{AM1.5} = \frac{P_{ph,\lambda}^{AM1.5}(\lambda)}{hc} \tag{3.10}$$

where h is Planck constant, c is the speed of light in vacuum, $P_{ph,\lambda}^{AM1.5}$ is the AM1.5 spectral power density.

Because EQE measured also includes the reflectance losses, the total reflectance of the cell is measured for obtaining the Internal Quantum Efficiency (IQE). IQE indicates the fraction of absorbed photons that are successfully collected, which is calculated by Equation 3.11:

$$IQE = \frac{EQE}{1 - R(\lambda)} \tag{3.11}$$

where $R(\lambda)$ is the reflectance measured by Lambda 1050 system (UV-Vis-NIR spectrophotometer) , and $1 - R(\lambda)$ is the effective absorbance assuming no transmission is occurred.

4 Optimization of Hydrogenated Intrinsic Amorphous Silicon Layers

As it is mentioned in Chapter 2, surface passivation at the a-Si:H and c-Si could be enhanced by implementing an intrinsic a-Si:H bilayer, consisting an underdense layer and a denser layer. To optimize the structure of (i)a-Si:H bilayer, a database containing microstructure properties of various (i)a-Si:H single layers was first established. During this period, the influence of PECVD deposition parameters, such as pressure, power, and dilution ratio on the microstructure properties of (i)a-Si:H were studied. Subsequently, various bilayer candidates were selected and the passivation qualities of the resulting bilayers were studied. Finally, the impacts of hydrogen plasma treatment (HPT) and very high frequency (VHF) treatment on microstructure properties and passivation qualities were investigated for following SHJ solar cell fabrication.

4.1 Microstructure properties of (i)a-Si:H

4.1.1 Flowchart and Methods

The investigation on the microstructure properties of (i)a-Si:H layers follows the steps below:

1. **Pre-deposition**: N type (100) Siegert wafers were textured by 5% TMAH solution into (111) surface orientation and cleaned by 3 times of NAOC. The details of the pre-deposition process could be found in Section 3.1.
2. **Preliminary test on glass**: As mentioned in Section 3.3.1, the thickness of the deposition layer could not be directly determined on textured wafers. Therefore, in order to measure the deposition rate and access the non-uniformity, a deposition test on the glass substrate was performed when changing the deposition parameters of PECVD. Non-uniformity (NU) is based on Equation 4.1 [66]:

$$NU\% = \frac{t_{max} - t_{min}}{2 \times t_{avg}} \tag{4.1}$$

   where $NU\%$ is the deposition non-uniformity, $t_{max}$and t_{min} are the maximum and minimum thickness, respectively, t_{avg} is the mean thickness.

On the glass, a total of nine points (3x3) were measured. The (i)a-Si:H layers with $NU \leq 10\%$ are considered to meet the uniformity criteria and will proceed to the next experiment.

3. **Deposition on textured wafers**: To collect the background spectrum for FTIR analysis, the wafer was divided in half. One half of the wafer was stored in a vacuum box as a reference for future use in FTIR analysis, while the other half of the wafer underwent deposition in PECVD. As shown in Figure 4.1, a symmetric i-layer deposition was performed on the textured wafer. To ensure comparability among different samples, the thickness of the layer is aimed to be controlled to 10 nm.

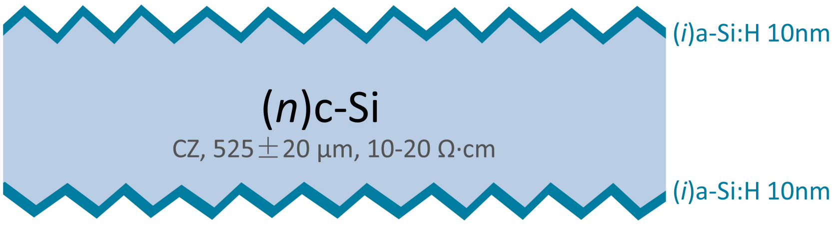

Figure 4.1: Sketch for FTIR measurement sample.

4. **Lifetime and FTIR measurement, data analysis**: After deposition, lifetime first was measured. Subsequently, the sample was placed in FTIR spectroscopy to obtain transmittance spectra as a function of frequency. Microstructure property was obtained after further analysis. The details can be found in Section 3.3.3.

Figure 4.2 shows a normalized infrared absorption spectra of an example of (i)a-Si:H layer after data processing. The figure has already subtracted the baseline from the raw data. The spectra consist of three absorption regions: Si-H wagging mode at $\omega = 640\,cm^{-1}$, Si-H bending scissor mode at $\omega = 840 - 890\,cm^{-1}$, Si-H low stretching mode (LSM) and Si-H high stretch mode (HSM) at around 2000 cm^{-1} and 2090 cm^{-1}, respectively [59]. This is coherent with previous literature in Section 3.3.3.

4.1.2 Effects of Deposition parameters on the microstructure properties of (a)-Si:H films

In order to systematically investigate the microstructure characteristics of the hydrogenated intrinsic a-Si film, their relationship with PECVD parameters has been studied. Table 4.1 displays the reference parameters of the (i)a-Si:H bilayers implemented in the standard SHJ solar cells. The effect of temperature has been previously optimized to be 160 °C [22].

In this thesis, the individual effects of dilution ratio, pressure, and power on the microstructural properties of a-Si:H layer were first studied, then the effect of their combinations were also assessed. To study the impact of the hydrogen dilution ratio, the

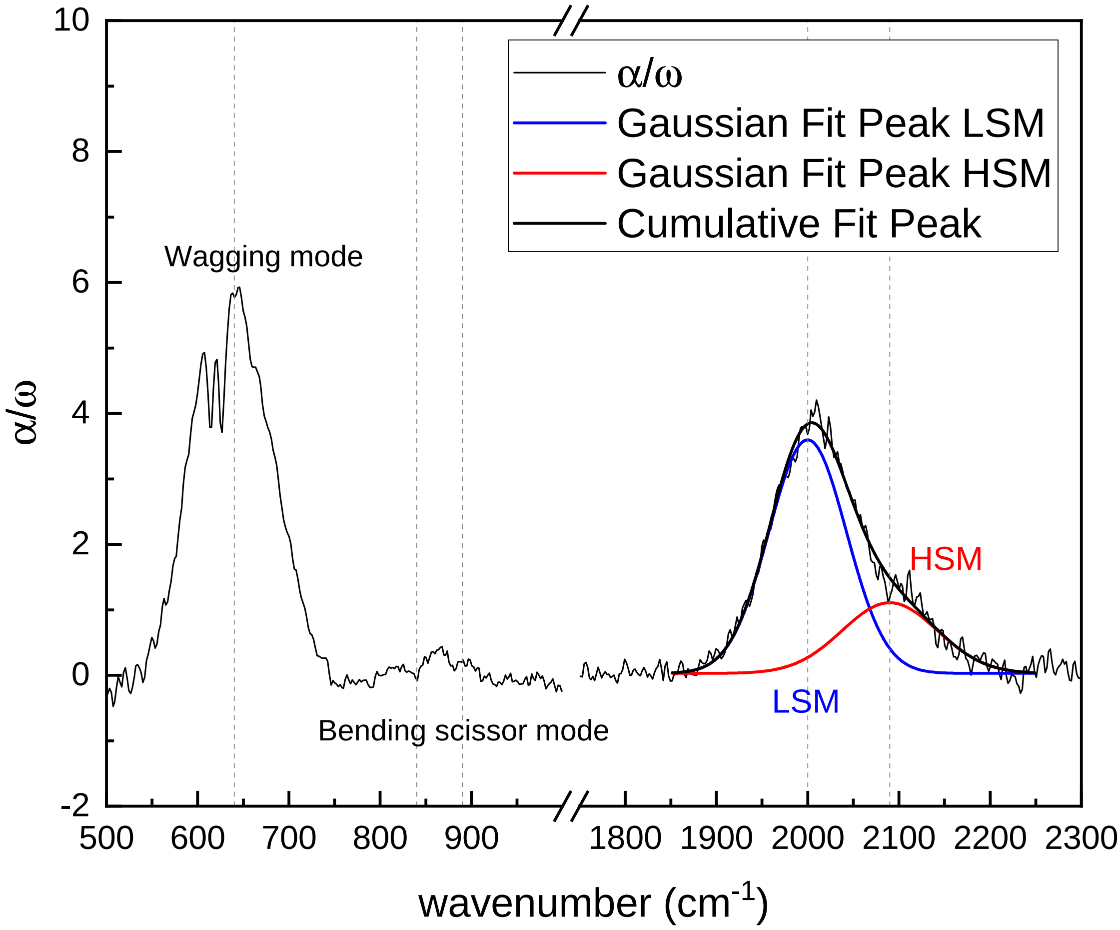

Figure 4.2: An example infared absorption spectrum of (i)a-Si:H film deposited by PECVD. Two Si-H stretching modes, LSM and HSM, are fitted by Gaussian functions.

Table 4.1: Main deposition parameters of rf-PECVD

Parameters	Dilution Ratio H_2(sccm)/SiH_4(sccm)	Pressure mbar	Power[1] W	Flow rate sccm	$T_{Substrate}$ °C	Frequency MHz
Standard i1	0	0.7	3	40	160	13.56
Standard i2	3	1.4	3	40	160	13.56
(i)a-Si:H	0-5	0.4-2.8	1-12	40	160	13.56

total gas flow rate was fixed at 40 sccm. The ranges of variations for the main deposition parameters are shown in Table 4.1 in the third row.

Effect of Pressure

To study the effect of pressure, the power was fixed to 3 W in various dilution ratios from 0 to 5. Figure 4.3 shows an example of the absorption spectra of (i)a-Si:H films in relation

---

[1] The size of the electrode showerhead in Amigo is fixed to 12 cm × 12 cm, allowing the power parameter studied in this thesis could be converted into power density. For instance, an RF power of 3 W in this thesis corresponds to 20.8 mW/cm^2.

to pressure, using pure silane plasma (DR = 0). As pressure rises, the proportion of the HSM absorption strength increases, indicating an increase in the microstructure factor R* [20]. This means a larger density of monohydrides and polyhydrides of larger volume deficiencies such as nano-sized voids at the internal surfaces in the a-Si:H film [22].

According to Equation 3.5, the relative H content could be compared by the areas under curves of both LSM and HSM. In Figure 4.3, as pressure increases, the absorption peak intensities of the LSM and HSM increase, indicating a higher hydrogen content in the amorphous network with higher pressure [20], [67].

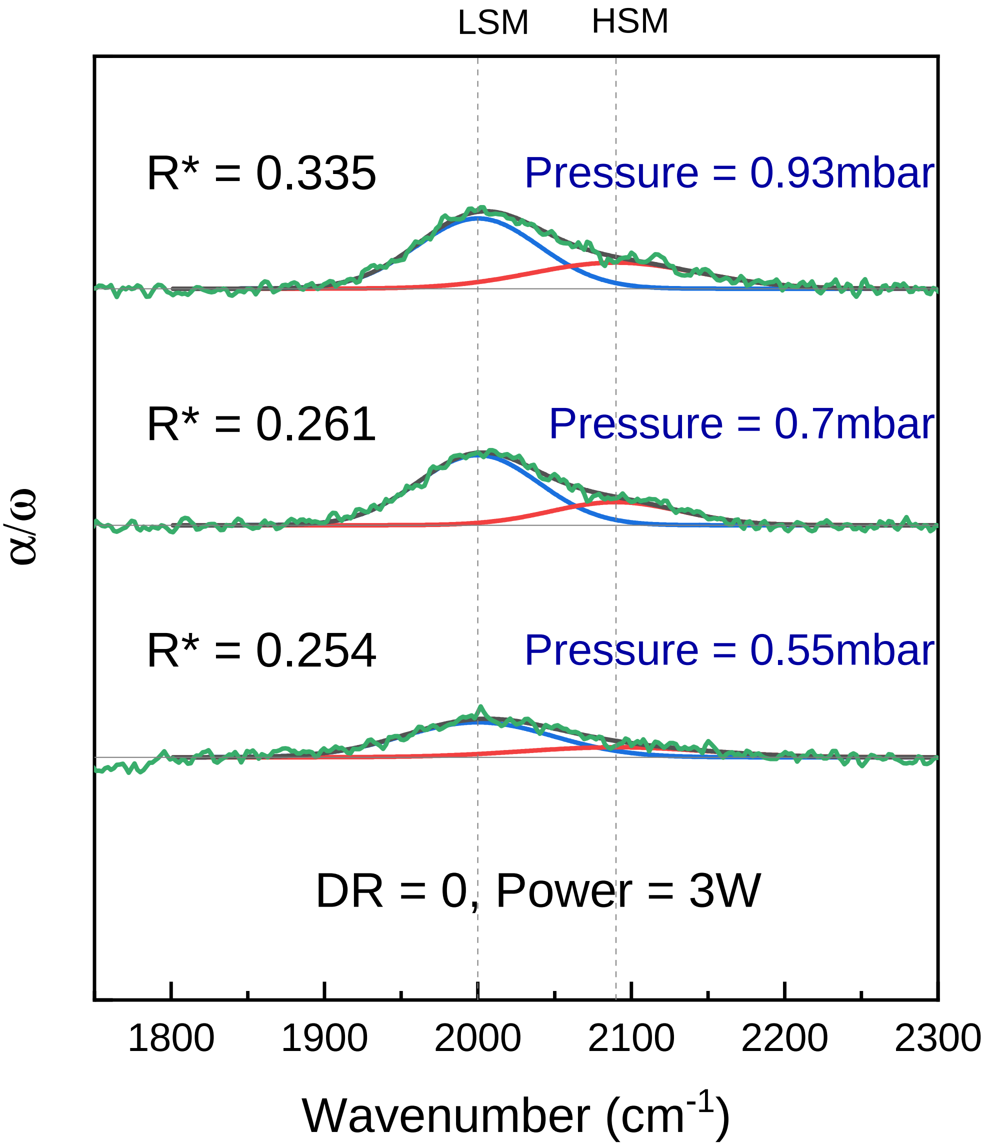

Figure 4.3: Infrared spectra of (i)a-Si:H films deposited at different pressures. The deposition power was fixed to 3 W and pure silane (DR = 0) was used.

Effect of Power

Similarly, the influence of RF power was changed with different DR conditions, while keeping the deposition pressure at 0.7 mbar. Figure 4.4 shows an example of the infrared spectra of (i)a-Si:H films as a function of pressure at DR = 0. The absorption strength of high stretching modes increases significantly as power is raised from 3W to 8 W. With high RF power, SiH$x \leq 2$ radicals dominate in film growth and start to form higher silane molecules, which is responsible for Si-H_2 bonding configurations. Therefore, the (i)a-Si:H film becomes more void-rich and H-rich [39].

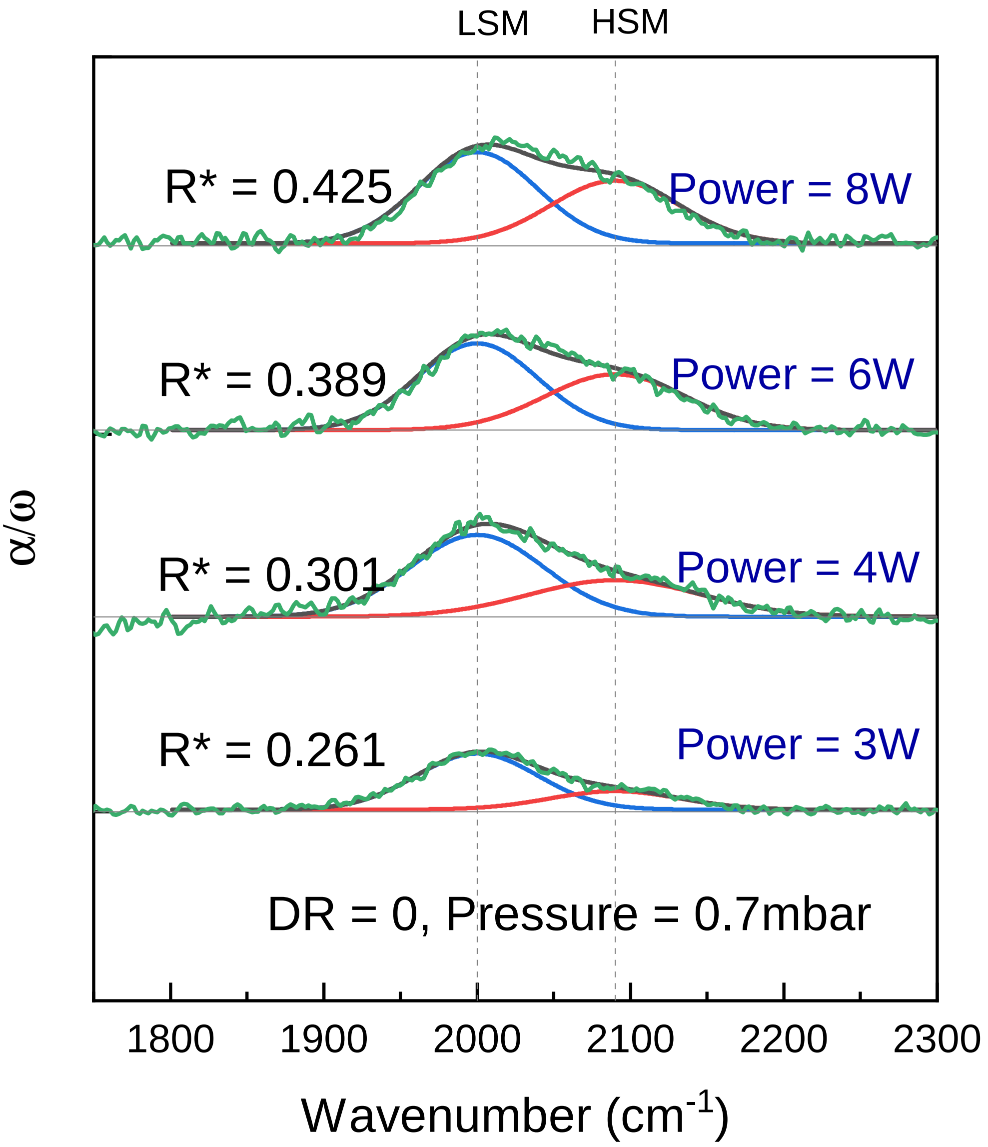

Figure 4.4: Infrared spectra of (i)a-Si:H films deposited at different RF powers. The deposition pressure was fixed to 0.7 mbar and pure silane (DR = 0) was used.

Combined Effect of Pressure and Power

As mentioned in Section 2.2.2, the RF power is related to the dissociation of the gas molecules, while the deposition pressure influences the mean free path of the radicals. To study the combined effect of increasing pressure and power simultaneously, the ratio between pressure and power was first fixed. The ratio of power to pressure is referenced to the parameters of i1 layer in the standard recipe, as shown in Table 4.1, which is 3 W / 0.7 mbar.

In Figure 4.5, four subplots with different dilution ratios are displayed, presenting the infrared peak spectra when the power and pressure increase proportionally. The area and proportion of HSM intensity increase significantly with an increase in power and pressure, whereas LSM sometimes decreases slightly or remains relatively unchanged. This indicates that the (i)a-Si:H film becomes more void-rich and H-rich, coherent to the impacts of changing power and pressure individually, as presented in Section 4.1.2.

It is also observed that at high stretching mode, the peak shift to a smaller wavenumber slightly with higher power and pressure. This is well coherent with the finding in [39]. Therefore, in this thesis, for R* > 0.5, the peak absorption spectrum is fitted to center at 2080 cm^{-1} instead of 2090 cm^{-1}.

As presented in Figure 4.5, by simultaneously increasing power and pressure and keeping their ratio constant, a significant enhancement in R* can be achieved. However, the Figure 4.6 shows both the R* factor and deposition rate of films change when increasing the power and pressure simultaneously. An excessively rapid deposition rate can present difficulties in effectively controlling the process to attain extremely thin film thicknesses, which are in the order of a few nanometers. For example, the highest R* = 0.805 in the figure occurs when DR = 1, Power = 12 W, and Pressure = 2.8 mbar, and the deposition rate reaches 0.91 nm/s. This means it would only take 1.9 s to have a 1 nm thin layer on a textured wafer, which is the i-1 layer that used for solar cells. Considering the delay time of controlling Amigo remotely and the 5 s time interval for logbook data recording, it becomes challenging to precisely control the deposition thickness and monitor the ignition process within such a short period.

To extend the deposition time and thus the controllability of deposited thickness of films featuring high R* values, the influence of power and pressure on deposition rate were studied individually. As shown in Figure 4.7a, increasing RF power increases the rate of SiH_4 dissociation, thus increasing the deposition rate. In Figure 4.7b, while increasing pressure and keeping the RF power constant, the growth rate is lower due to the reduction in the mean free path of the dissociation products [39].

The reduced deposition rate with increasing pressure gives a hint of better control of thickness. A further increase in pressure could increase both the R* and reduce the deposition rate. The absorption spectra of the a-Si:H film grown at different pressures and powers are shown in Figure 4.8. At DR = 1, the pressure is increased from 1.9 mbar to 2.8 mbar, while power is maintained at 8 W. As consistent with the trend highlighted in Section 4.1.2, the microstructure factor increased from 0.637 to 0.732, and the area below the HSM curve expanded, indicating an increase in H content. The deposition time on 1 nm textured wafer is prolonged from 2.5 s to 3.2 s. Although following the

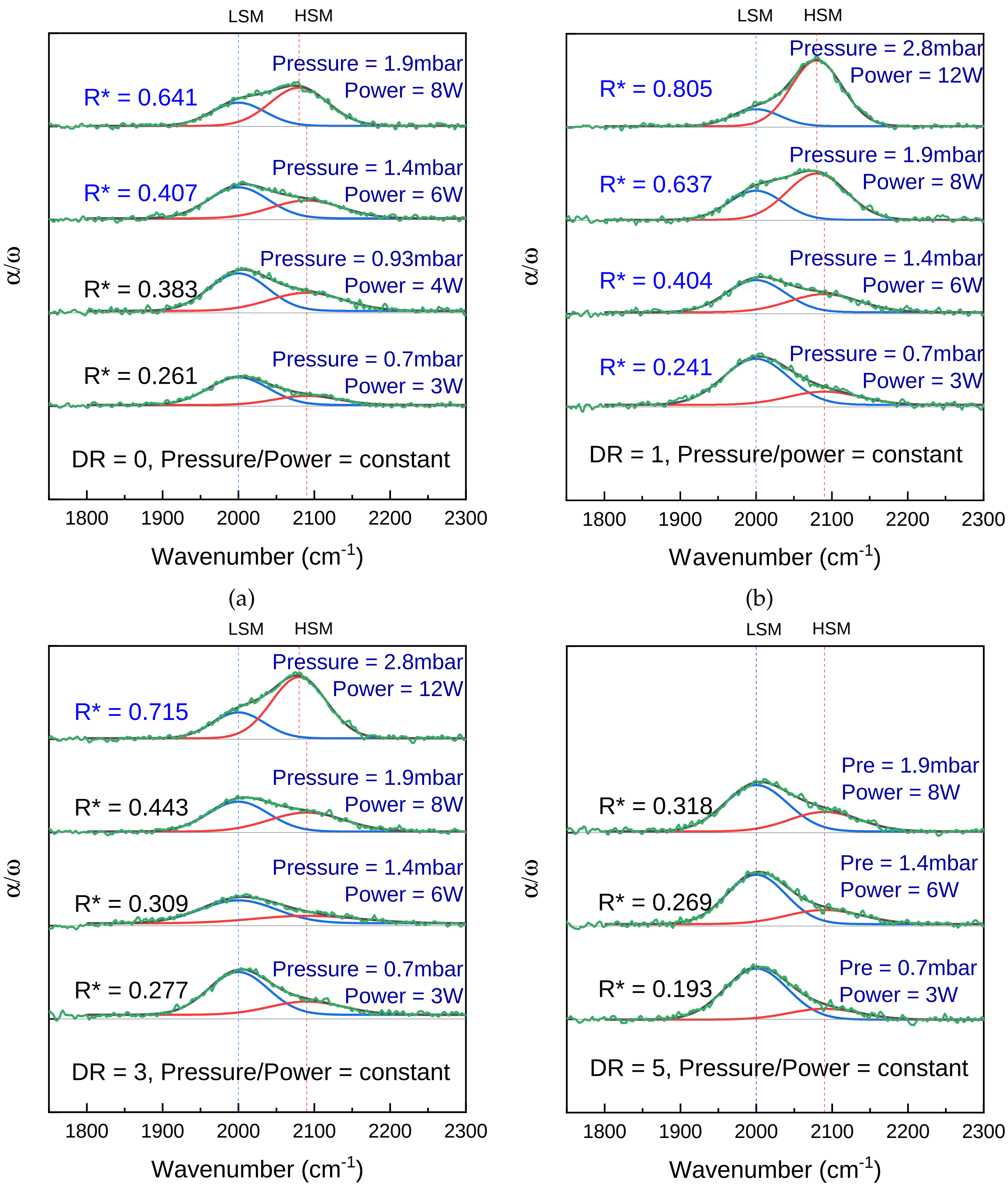

(a) (b)

(c) (d)

Figure 4.5: Infrared spectra of (i)a-Si:H films deposited with different dilution ratios: (a) DR = 0, (b) DR = 1, (c) DR = 3, and (d) DR = 5, while the RF power and deposition pressure increased proportionally. For R* $>$ 0.5, the peak wavenumber of HSM is fitted to 2080 cm^{-1} instead of 2090 cm^{-1}.

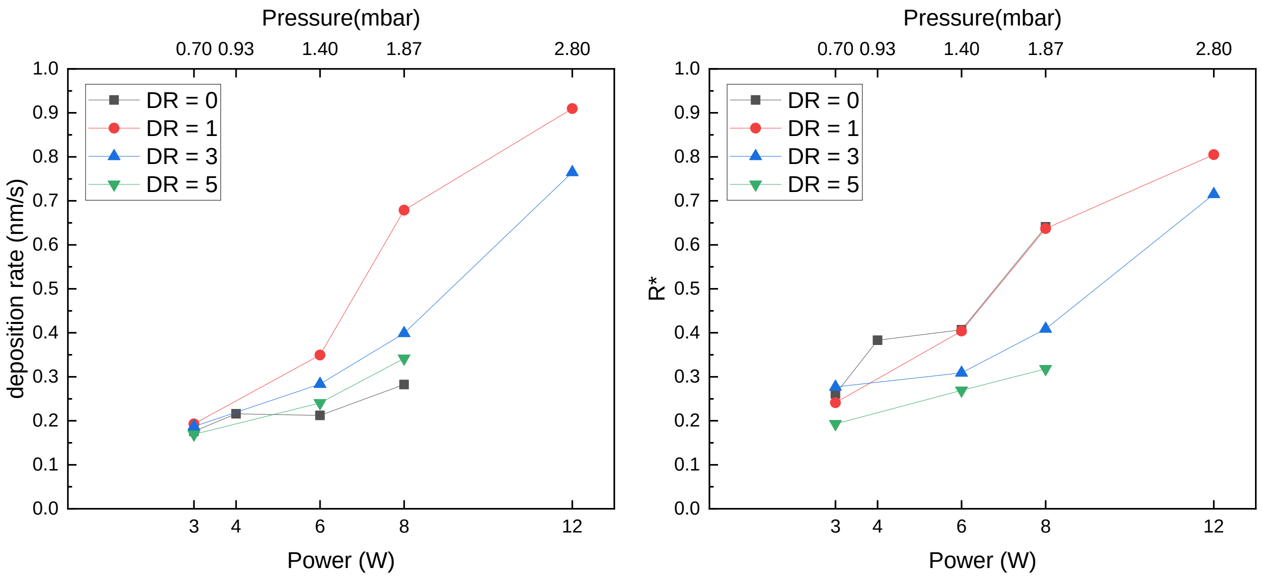

(a) (b)

Figure 4.6: (a) Deposition rate of (i)a-Si:H layer and (b) microstructure factor R* of (i)a-Si:H layer as functions of increasing power and pressure at different dilution ratios.

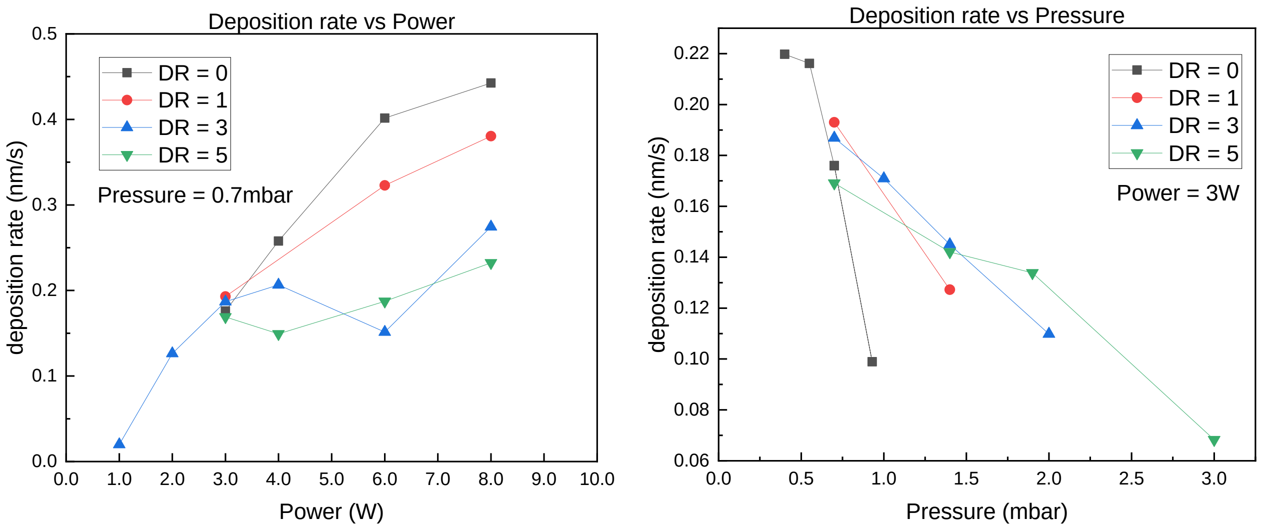

(a) (b)

Figure 4.7: Deposition rate of (i)a-Si:H layer: (a) as a function of increasing RF power at different dilution ratios (DR), with pressure fixed at 0.7 mbar, and (b) as a function of increasing pressure at different dilution ratios (DR), with the power fixed at 3W.

same ratio of power/pressure, increasing the power to 12 W could lead to a higher R* of 0.805 and higher H content, the deposition time would then be reduced to 1.9s. Therefore, this provides an opportunity to use a film with a higher R* value while still maintaining a reasonable deposition rate, which is crucial for better process control. Similarly, in the case of the film with an R* value of 0.805 (deposited at 2.8 mbar and 12 W), a lower deposition rate can be attained by further increasing the pressure. However, due to concerns related to non-uniformity, this particular film has been excluded from consideration.

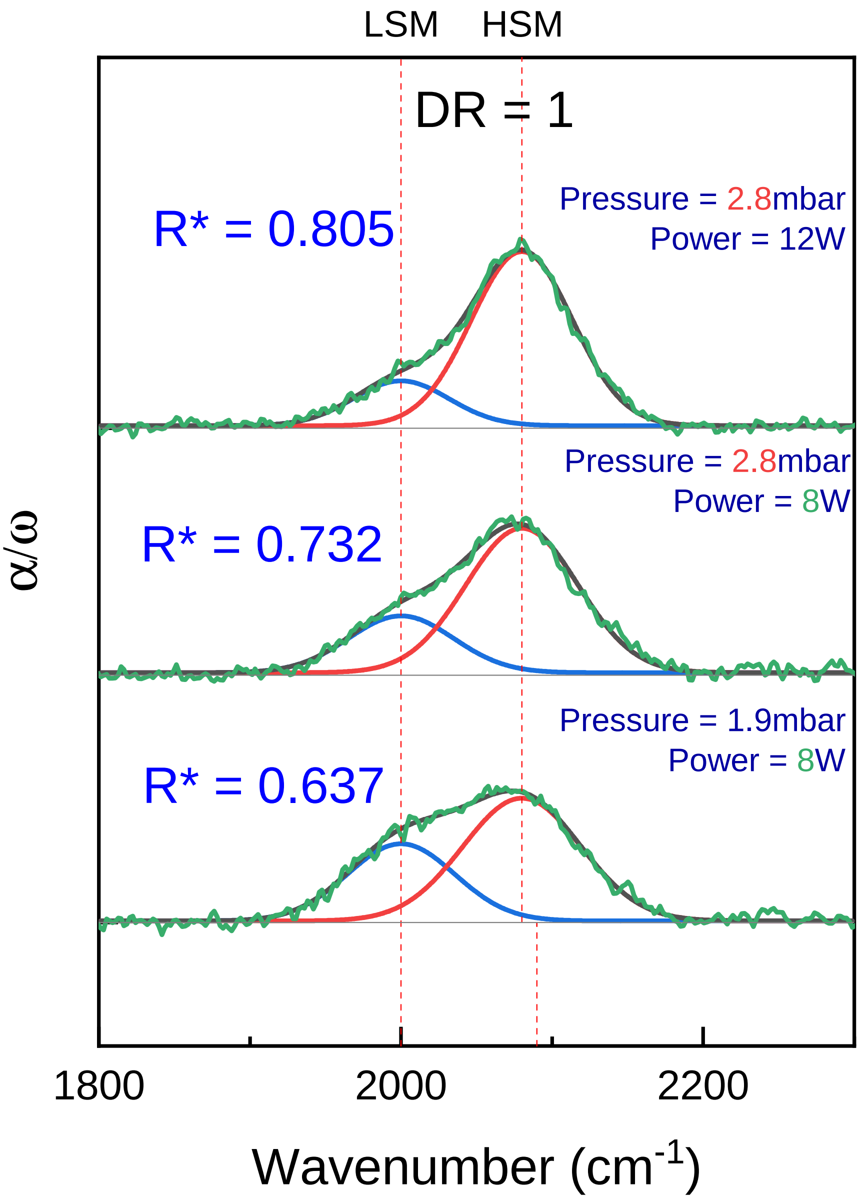

Figure 4.8: A comparison of the infrared spectrum when further increasing pressure

Effect of Dilution Ratio

Figure 4.9 shows infrared spectra of (i)a-Si:H films with different dilution ratios. In general, with the same parameters, R* is smaller with higher dilution ratios. This indicates that the (i)a-Si:H film becomes denser. This is contributed to the etching effect from more hydrogen plasma, which breaks up weak Si-bonded hydrogen that forms clusters [19]. With a higher proportion of hydrogen diluted into the silane gas, the intensity of the low-stretching mode increases, while for high-stretching mode decreases slightly, which contributes to a higher H content in the film [68], [69]. The H-rich film could have a better passivation quality, which will be discussed in Section 4.2.2.

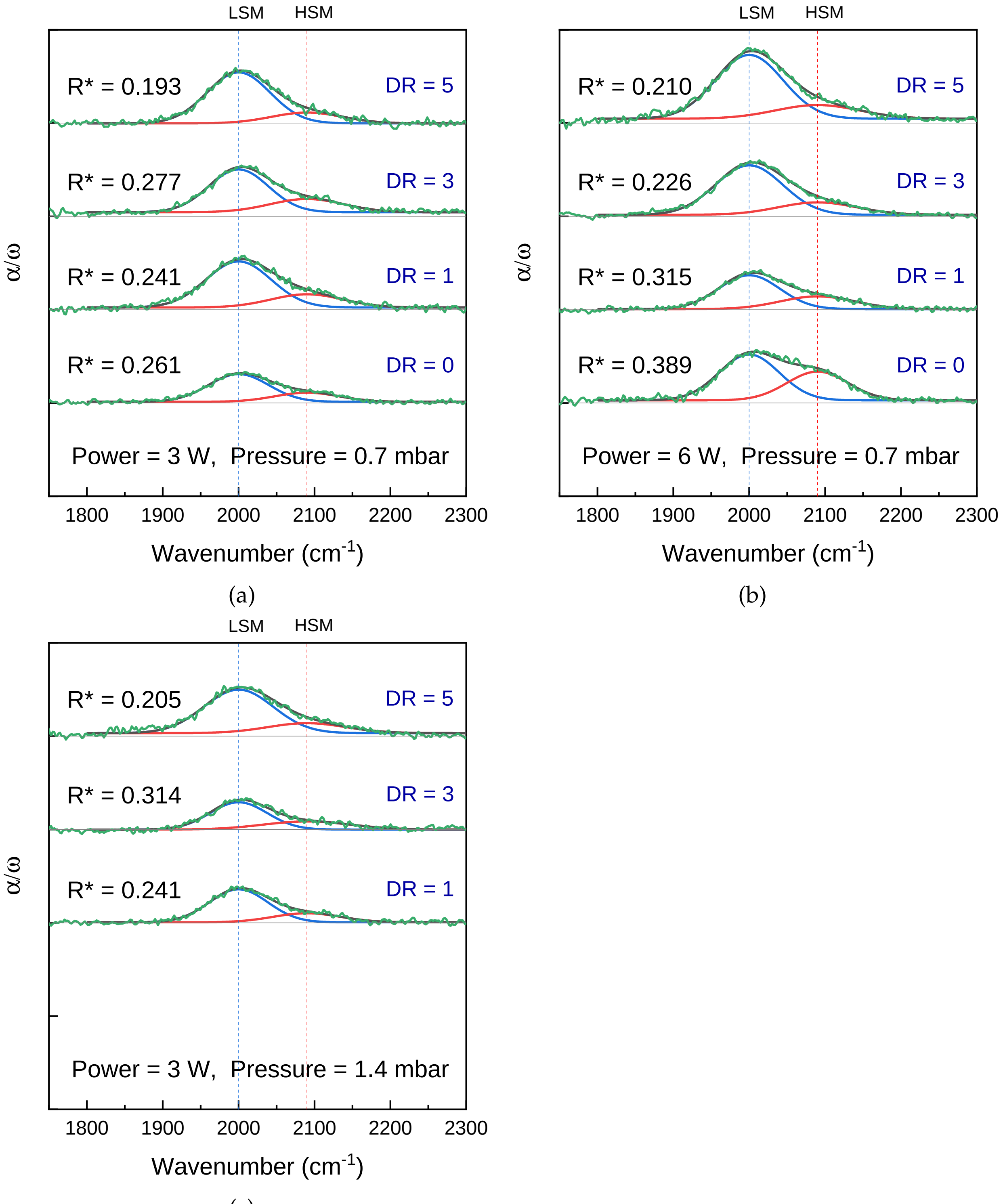

(a)

(b)

(c)

Figure 4.9: Infrared spectra of (i)a-Si:H films deposited with different dilution ratios, while in different subplots the power and pressure were kept the same. For Figure 4.9c, DR = 0 is excluded because of non-uniformity in the film.

4.1.3 R* Database for (i)a-Si:H

To conclude all the data points of R* that were achieved in the variation of deposition parameters, a database R* with containing different combinations of dilution ratio, power and pressure is generated. As shown in Figure 4.10, four subplots represent the R* factor at different dilution ratios, RF-power and deposition pressure.

In Figure 4.10, with the increases in power and pressure, the micro-structure factor R* becomes larger, indicating the film becomes less dense. The highest R* = 0.805 occurs when DR = 1, Power = 12 W, and Pressure = 2.8 mbar. At a higher dilution ratio, the R* decreases. The smallest R* = 0.193 occurs when DR = 0, Power = 3 W, and Pressure = 0.7 mbar.

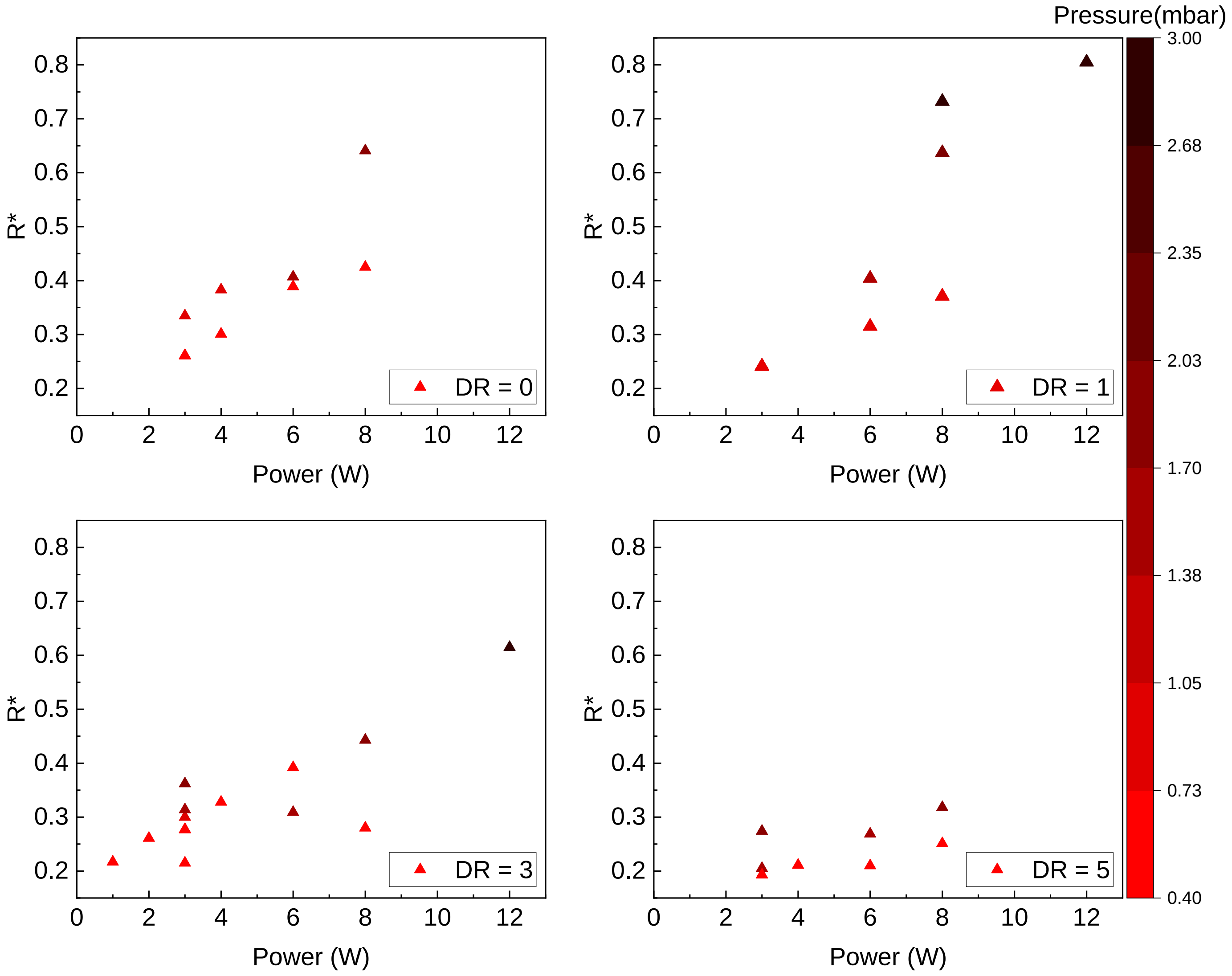

Figure 4.10: R* database of tested (i)a-Si:H films, while the x-axis shows the changes in power and the color of markers indicates the pressure. The deeper the red color, the higher the pressure. Different dilution ratios are shown in different subplots.

The hydrogen content of the (i)a-Si:H film is also analyzed quantitatively. However, the method of extracting H content through FTIR in Equation 3.5 is for films deposited on the flat wafers. For textured wafers, because of the enhanced light trapping, the incident infrared light will bounce inside the c-Si wafer several times, thus enabling the optical path longer than expected. This means the actual absorption spectrum α^*/ω is lower than the calculation as in Equation 3.3, due to a higher thickness t in reality. Therefore, the H content should be significantly lower than the calculated value. Furthermore, the proportional constants used for calculating H content from LSM and HSM may not be accurate as they were determined empirically.

Although the calculated H content values may not directly indicate the absolute value of H content, they are relatively comparable among the films deposited under different conditions. Figure 4.11 shows the relative H content of (i)a-Si:H with respect to the standard i1 layer. As seen in Figure 4.11a, with an increase in R*, the H content originates from the low-stretching mode decreases, while the H content attributed to HSM increase. Due to the more dominant role of HSM in determining the overall H content, an increase in overall H content as R* increases when adding up LSM and HSM together. At higher dilution ratio, even with lower R*, the total relative H content is higher. This is primarily due to the significant increase in C_H for LSM with hydrogen implementation, combined with slightly decreased HSM, which raises the H content while preserving a relatively low R*.

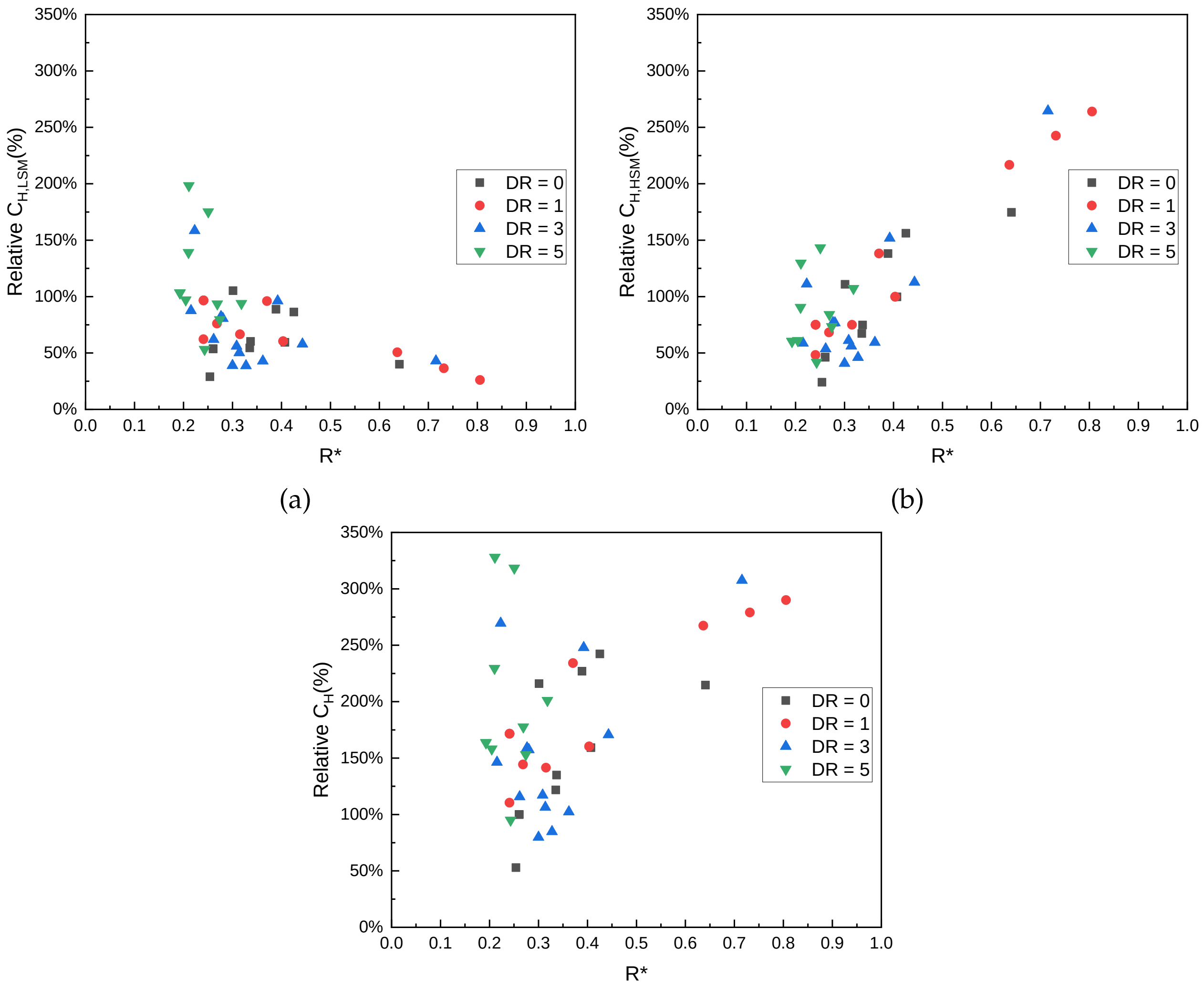

(a)

(b)

(c)

Figure 4.11: (a) Relative H content of LSM, (b) relative H content of HSM, and (c) relative overall H content in 10 nm (i)a-Si:H layers, symmetrically deposited on double-side-textured wafers, as a function of R* under different deposition conditions. The variations of power and pressure are not represented in the graphs. All the films are referenced to the standard i1 layer shown in Table 4.1.

4.2 Passivation optimization of (i)a-Si:H Bilayers

Based on the R* database that was established in the previous section, the (i)a-Si:H bilayers could be further optimized. In this section, an initial passivation test was first conducted to compare the passivation quality of monolayer and bilayer. Then, the thickness of the bilayer was optimized, followed by an examination of R* effects in relation to its layer. Finally, the influences of hydrogen plasma treatment (HPT) and very high-frequency treatment (VHF) were studied. FTIR analysis was employed as well to compare the H contents among films.

4.2.1 Flowchart

Figure 4.12 shows the flowchart of (i)a-Si:H bilayer test. Two different types of wafers were chosen for the passivation test and FTIR analysis, respectively. To mitigate the influence of uncertainty arising from variations in deposition among different batches in Amigo, both two wafers were cut into halves. One-half of each wafer was then combined and placed into one holder. This approach ensures that the same deposition environment is applied to different wafers.

Figure 4.13 shows the symmetric bilayer structure deposited on the Topsil wafer used for passivation tests. A series of layers were selected as in Table 4.2, considering uniformity and R*. Standard layers (STD i1 and STD i2) were chosen as references. To ensure it is also comparable for H content, the total thickness of the layers for each side is designed to be 10 nm.

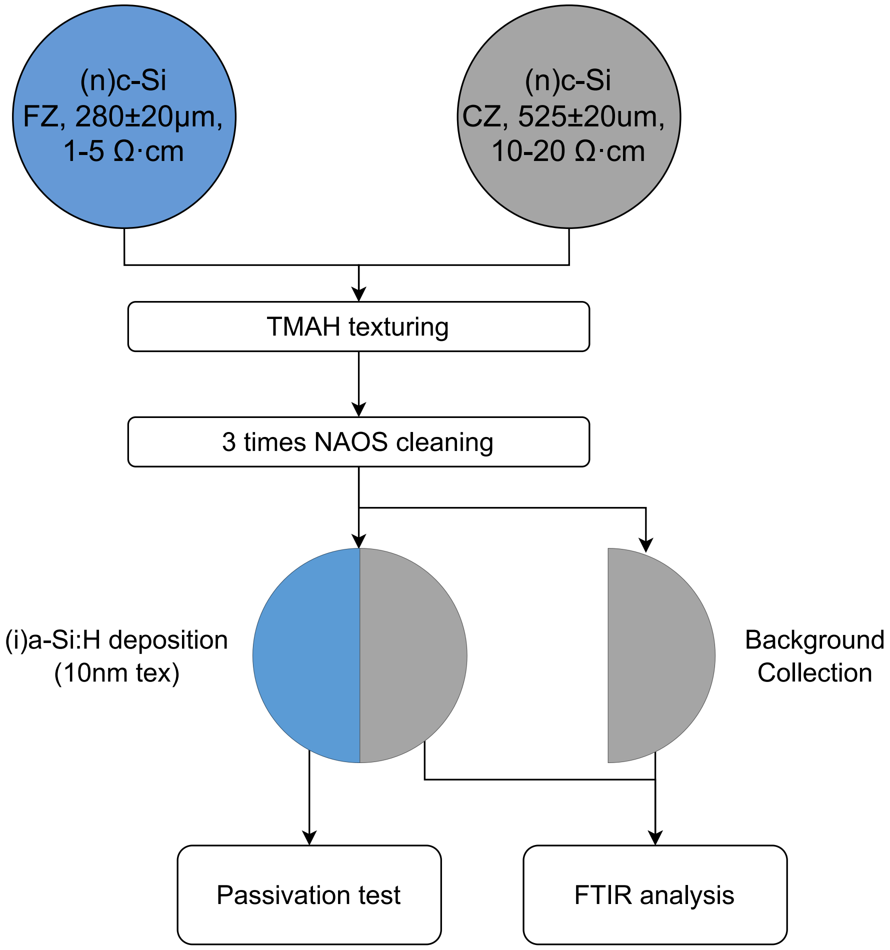

Figure 4.12: Flowchart of the bilayer tests

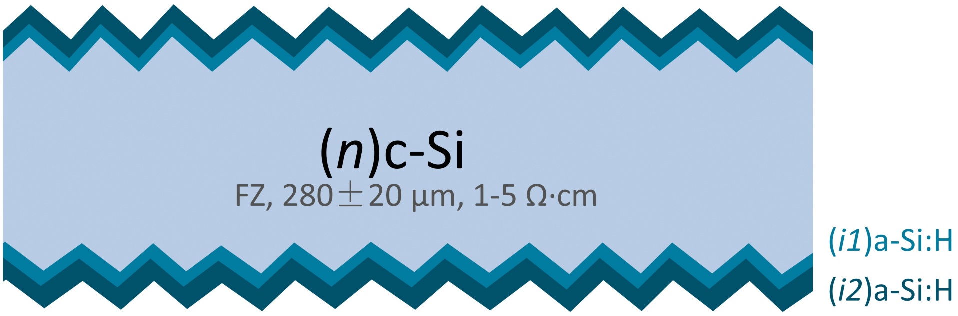

Figure 4.13: Optimized (i)a-Si:H bilayer passivation sketch

Table 4.2: Deposition parameters and properties of the selected (i)a-Si:H layer

Parameters	Dilution Ratio H_2(sccm)/SiH_4(sccm)	Pressure (mbar)	Power (W)	R* (-)	Non-uniformity (-)
STD i1	0	0.7	3	0.261	4%
STD i2	3	1.4	3	0.314	7%
X i1	0	0.93	4	0.383	8%
A i1	3	1.9	8	0.409	7%
B i1	1	1.9	8	0.637	9%
C i1	1	2.8	8	0.732	9%
D i2	5	1.4	3	0.205	5%

4.2.2 Passivation Results for Bilayers

According to [16] and [17], the optimal H-rich and underdense i1 buffer layer should be below 2 nm considering surface passivation and carrier transport. As a preliminary test, bilayer composed of a 2 nm i1 layer and an 8 nm i2 layer was compared with 10 nm i1 single layer and i2 single layer, respectively. Then, a total thickness of 10 nm for both sides was fixed to find the optimal thickness combination of the i1 and i2 layers, especially the i1 layer. Due to the rather significant batch-to-batch variations of passivation quality, passivation results were compared exclusively within the same batch.

Preliminary bilayer test

Lifetime results for bilayer structures were compared with single layers in Figure 4.14. Compared with i1 layers, i2 layers have better passivation qualities. This could be explained by the denser and less-defective film deposited with diluted silane. As for the bilayer, although the i1 layers alone have poor passivation quality because of the large density of defects, its combination with the i2 layer outperformed the passivation qualities of single layers. This is related to void-rich and H-rich i1 preventing the epitaxial growth at c-Si and a-Si:H interface that could be induced by the deposition of i2 layer, and thus improving the surface passivation [20]. Moreover, by using less dense i1 and denser i2 layers forming the bilayer, the passivation quality of the bilayer is better as compared to the bilayers with standard i1 and i2 layers. This is because more H-rich and void-rich i1 could better suppress epitaxial growth and denser i2 could cap H within the i1 layer [24]. By using the designed bilayer, the lifetime increases to 3.4 ms, indicating a promising improvement.

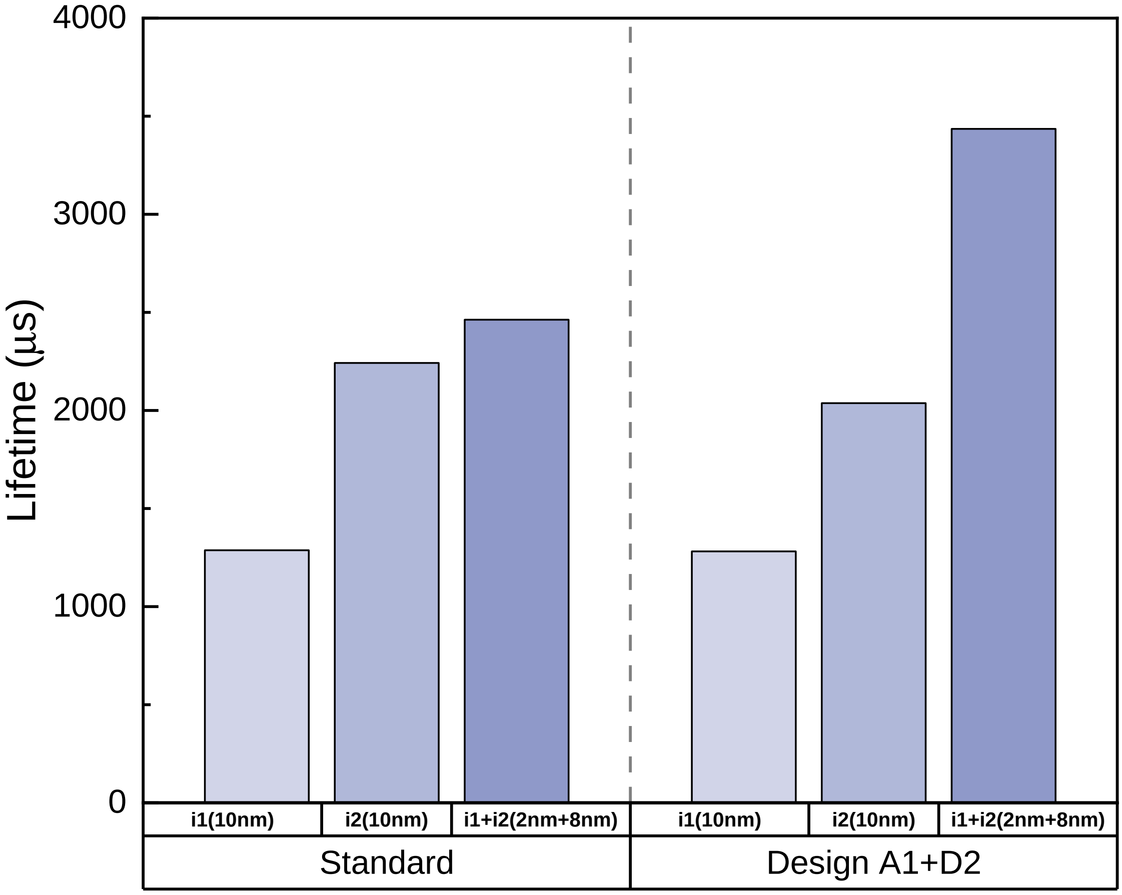

Figure 4.14: Lifetime results for bilayers. The combined bilayer structures using both the standard and designed recipes were contrasted with single layers. The material properties of various i1 and i2 layers are listed in Table 4.2.

Optmization of layer thickness

As shown in Figure 4.14, although implementing i1 layer could have a better passivation, constantly increasing i1 to 10 nm could only have a worse performance because of the large density of defects. Therefore, the thickness of i1 should have an optimal value. In Figure 4.15, a total thickness of 10 nm was fixed to find the optimal thickness of the i1 layer. For the bilayer with the C1 + D2 combination, as the i1 layer increases from 1 nm to 3 nm, the lifetime decreases from 7.5 ms to 3.3 ms. In addition, a thicker i1 layer over 2 nm could deteriorate the FF of SHJ solar cells, which would be discussed in Chapter 5. As suggested in [17], a thinner thickness of 0.5-1 nm i1 a-Si:H buffer layer could improve the surface passivation effectively. However, to ensure the good controllability of the deposition process in PECVD, the optimal thickness of the (i1)a-Si:H layer is 1 nm and will not be optimized further in this thesis.

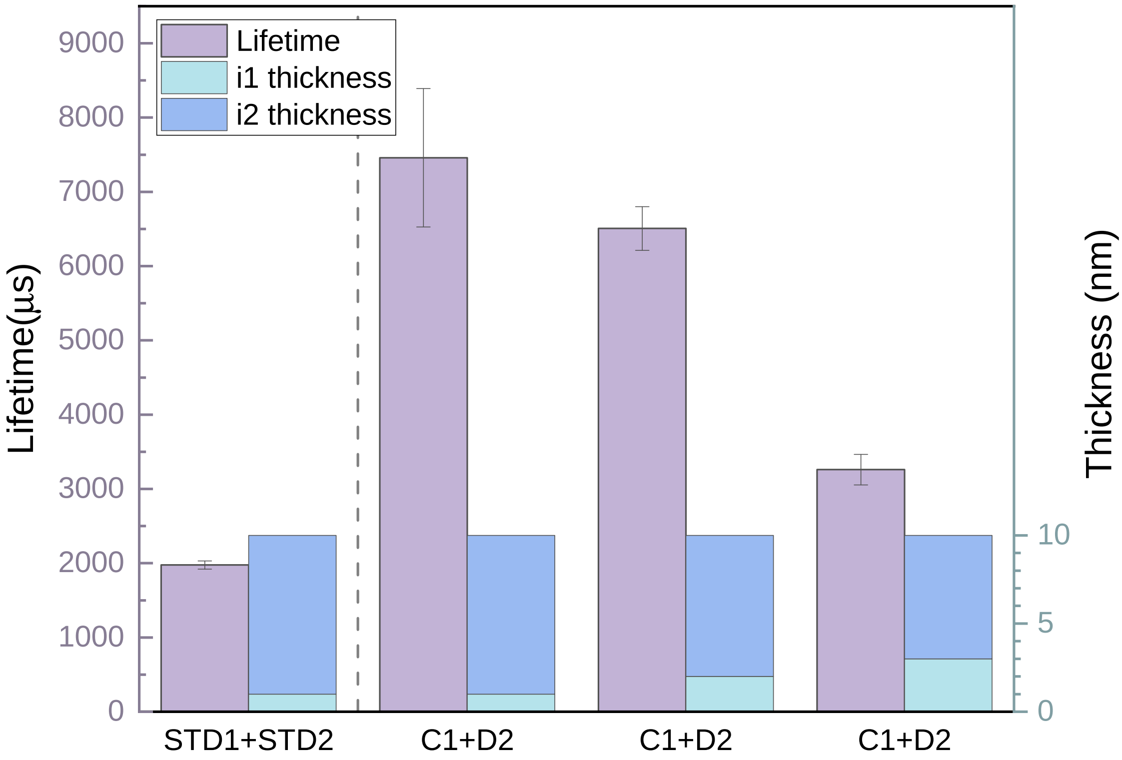

Figure 4.15: Lifetime results with different bilayer thickness combinations. The standard bilayer (1nm i1 + 9nm i2) is shown as a reference.

Effect of R* of layers on surface passivation quality

To investigate the impact of microstructure of each layer on the surface passvation quality, a series of samples were prepared with only one layer being modified. As shown in Figure 4.16, by replacing the standard i1 layer with a layer (A1) featuring a higher microstructure factor, the passivation increases from 2.0 ms to 4.8 ms. Furthermore, the lifetime improves to 6.8 ms by relacing the i2 layer with a denser film (D2). Therefore, the lifetime is independently enhanced when using i1 layer which is more H-rich and void-rich and capping with i2 layer which is denser [24].

To further investigate the effect of R* of i1 layers on the passivation quality, another batch of passivation tests regarding the range of R* of the i1 layer is conducted. As shown in Figure 4.17. With R* varying from 0.443 to 0.732, passivation continues to rise. It is worth noting that an optimized (i)a-Si:H should not only ensure excellent c-Si surface passivation quality, but also be less resistive to not hinder the transport of charge carriers. However, a higher R* could increase the series resistance in the fabrication of SHJ solar cells [20], which is going to be further optimized in Chapter 5.

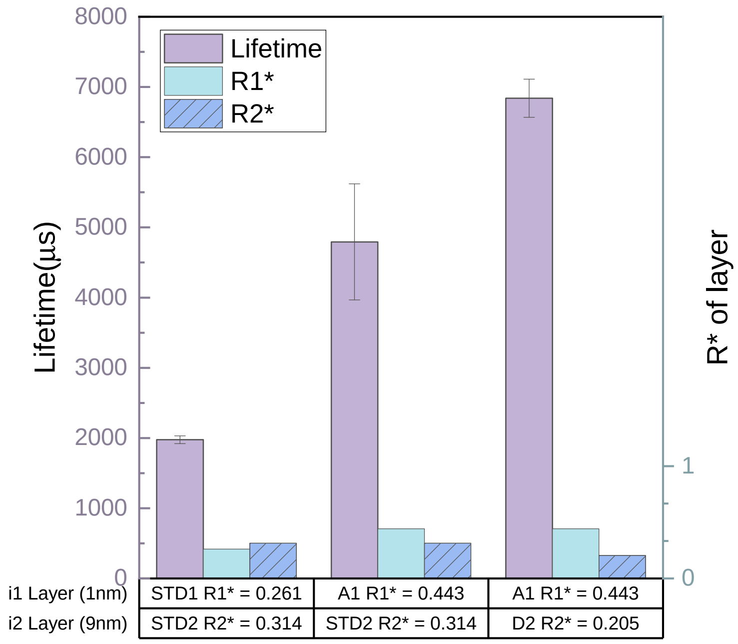

Figure 4.16: The passivation results as a function of changing layers individually. Firstly, the i1 layer was altered, followed by the i2 layer.

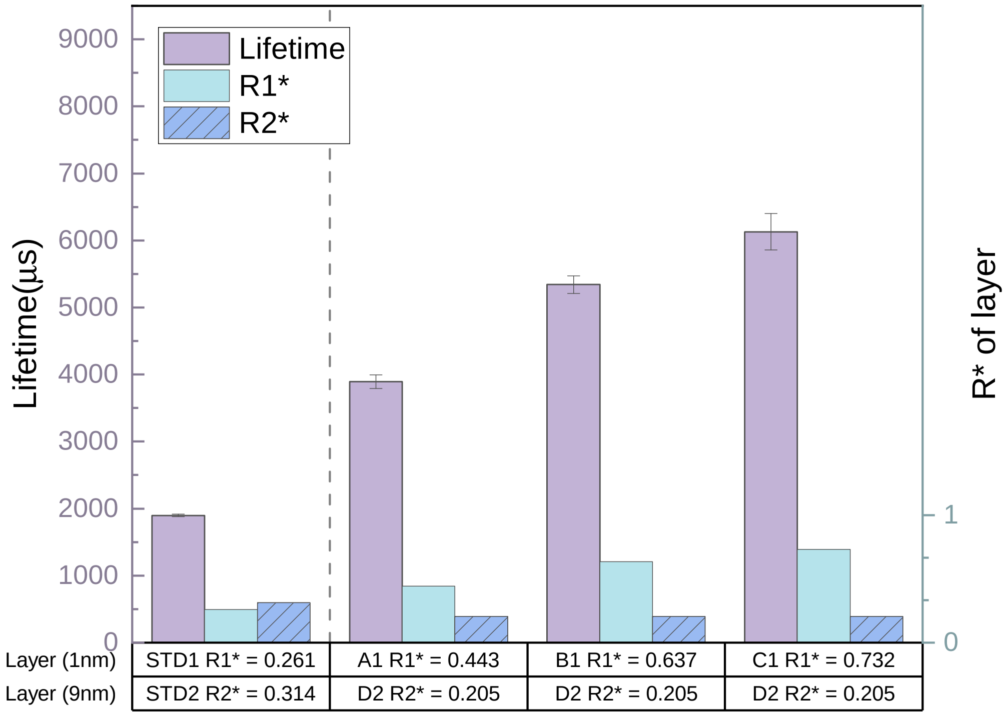

Figure 4.17: The passivation results as a function of changing i1 layer. Standard bilayer on the left was shown as a reference.

The variations in overall H content and R* of the bilayer were depicted in Figure 4.18 through changes in individual layers.

- Changes in i1 layer: The role of the i1 layer can be observed by comparing STD1+STD2 and X1+STD2, as well as STD1+D2, X1+D2 and D2. Since X1 has a higher R* = 0.383, the overall microstructure factor is higher when standard i1 is replaced with X1 layer. Meanwhile, the total H content is increased because X1 is richer with hydrogen. The reason for the lack of a significant increase in H content when comparing STD1+D2 with D2 could be: D2 contains a higher amount of H than STD1, as indicated in Figure 4.9. The passivation of implementing X1 is also improved, except that the lifetime for the X1+D2 sample fluctuated a lot.
- Changes in i2 layer: Due to more hydrogen diluted plasma in D2 that can incorporate more H for passivating the c-Si/(i)a-Si:H interface, the passivation enhanced with D2, as compared with STD1+STD2 and STD1+D2, or X1+STD2 and X1+D2 [18]. As the R* of the D2 film is lower and more H-rich, samples involving its participation should exhibit higher H content and smaller R*. This is coherent with X1+D2 combination. However, for the STD1+D2 sample, it is not the case. This is probably due to the instability of PECVD. In addition, with a denser i2, it could cap the hydrogen within the i1 layer, and penetrate and saturate hydrogen at the c-Si and i1 surface [24].

Despite some unexpected outcomes, possibly due to the instability of this round of Amigo and uncertainties in removing the baseline from FTIR absorption spectra, there is still a discernible trend in the overall relative H content and R* value changes. Looking at the lifetimes of solar cell precursors in Figure 5.15, the variations in passivation are consistent with expectations.

4.2.3 Impact of HPT and VHF Treatment

After (i)a-Si:H deposition, hydrogen plasma treatment (HPT) technique is commonly used to enhance passivation [70]. This technique involves the diffusion of hydrogen atoms with high energy into the (i)a-Si:H and c-Si interface, effectively saturating dangling bonds [71], [23]. Furthermore, very high frequency (VHF) treatment enables an effective selective etching of disordered material [72], which is beneficial to the nucleation for nanocrystal growth of thin doped layers deposited afterward, [11]. The deposition parameters for HPT and VHF treatment are shown in Table 4.3:

Table 4.3: PECVD HPT and VHF treatment parameters [11]

Parameters	SiH_4 sccm	H_2 sccm	Pressure mbar	Power W	$T_{Substrate}$ °C	Frequency MHz
HPT (p side)	0	200	2.2	9	180	13.56
HPT (n side)	0	200	2.7	9	180	13.56
VHF	1.2	120	4.0	13	180	40.68

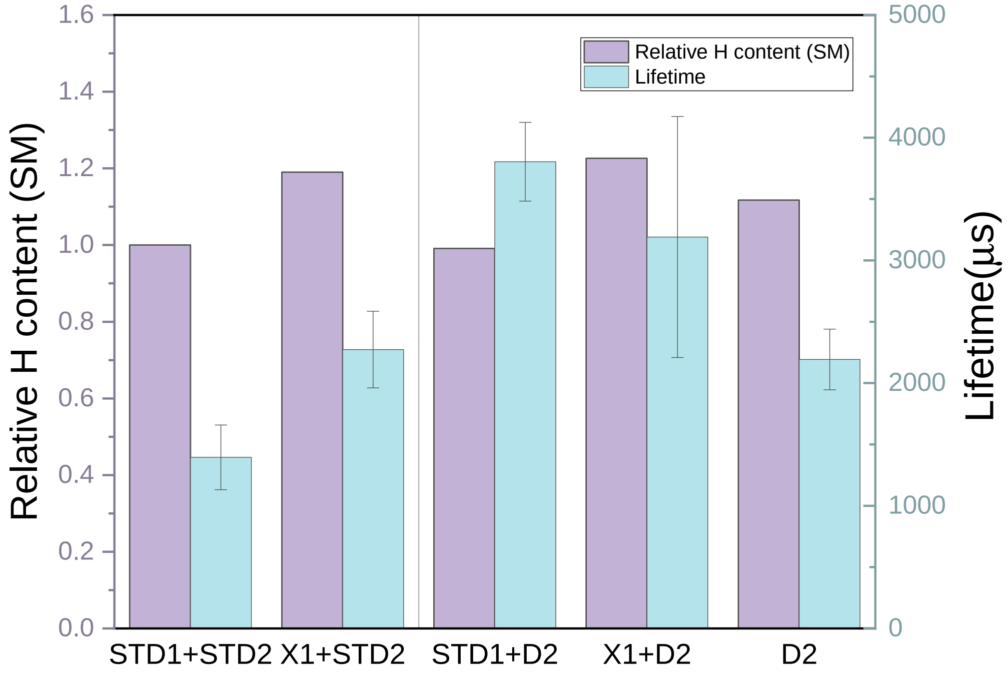

(a)

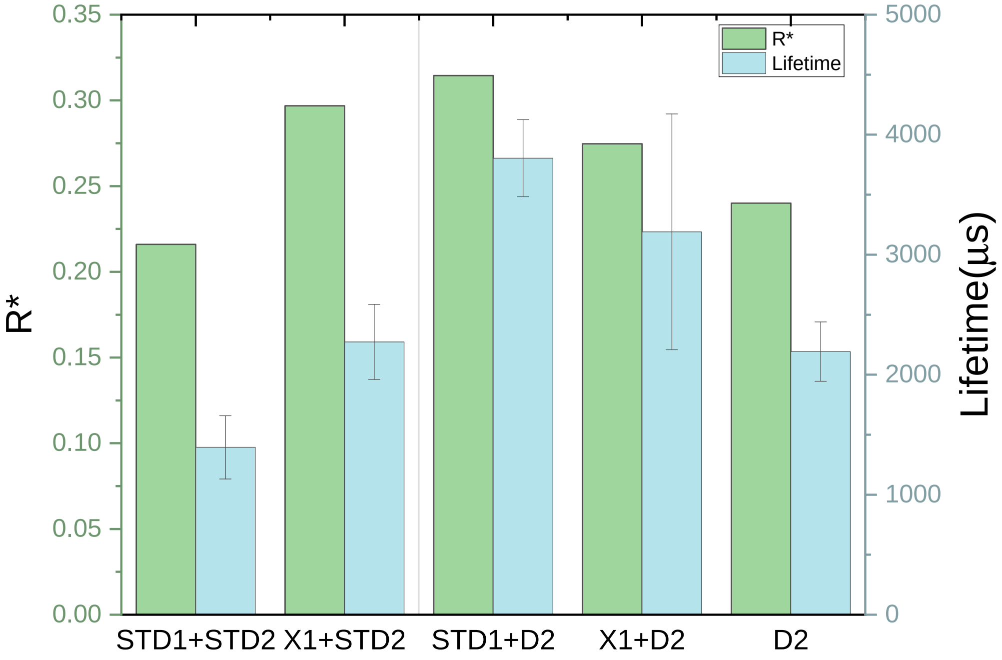

(b)

Figure 4.18: The lifetime of the selected (i)a-Si:H bilayers was compared with (a) Relative H content calculated from the stretching mode intensities. The H content in the standard bilayer structure was set as a reference of 100%. And (b) Overall microstructure factor R* versus lifetime. The total film thickness was maintained at 10 nm at both sides. The blue columns on the right represent the lifetime for each sample. The material properties of various i1 and i2 layers are listed in Table 4.2.

Passivation results after treatments

Figure 4.19 represents the passivation results after HPT and VHF treatments. The passivation quality improved significantly for all samples after treatments. However, after VHF, it is expected to have a constant passivation improvement [22]. Instead, the lifetime fluctuates a lot, which could be the instability of the VHF chamber of PECVD.

Despite the significant differences in lifetimes among various bilayers without HPT (variations from 2 ms to 7.5 ms), they all increased to over 17 ms after the treatment. This could potentially be attributed to the saturation of dangling bonds after HPT, consequently reducing the prominence of differences in lifetime among the various bilayers prior to HPT.

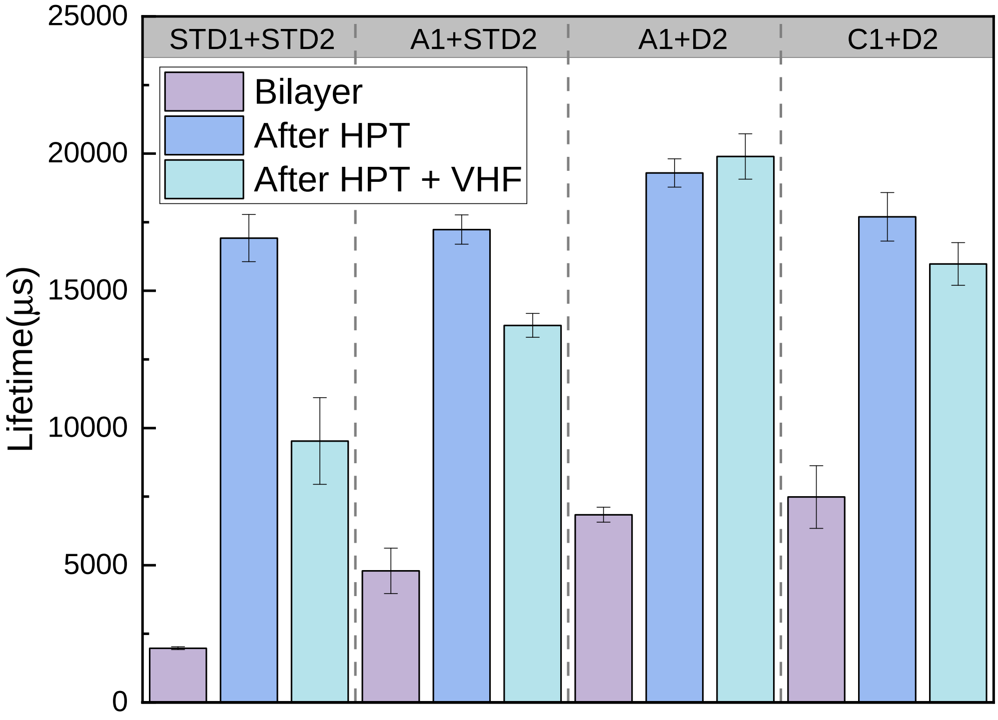

Figure 4.19: Passivation results after HPT and VHF treatments. A batch of three wafers was used to create the samples by altering the deposition conditions. This approach was chosen instead of subjecting a single wafer to three separate deposition and lifetime measurements in between, in order to minimize the influence of breaking the vacuum state on the samples and potential damage during measurement.

H content after treatments

Figure 4.20 shows the infrared spectra of the series samples of "A1 +D2" as an example. The peak of wavenumber has been shifted from 2000 to 2010 cm^{-1} for LSM to have a better fit according to [22]. The overall H content increased significantly. The deconvolution of the Si-H stretching mode shows that the monohydrides and dihydrides were increased after treatments [34]. The increase in R* suggests that the treatments result in a higher proportion of dihydride Si-H_2 bonds and the formation of nano-sized voids containing hydrogen [71].

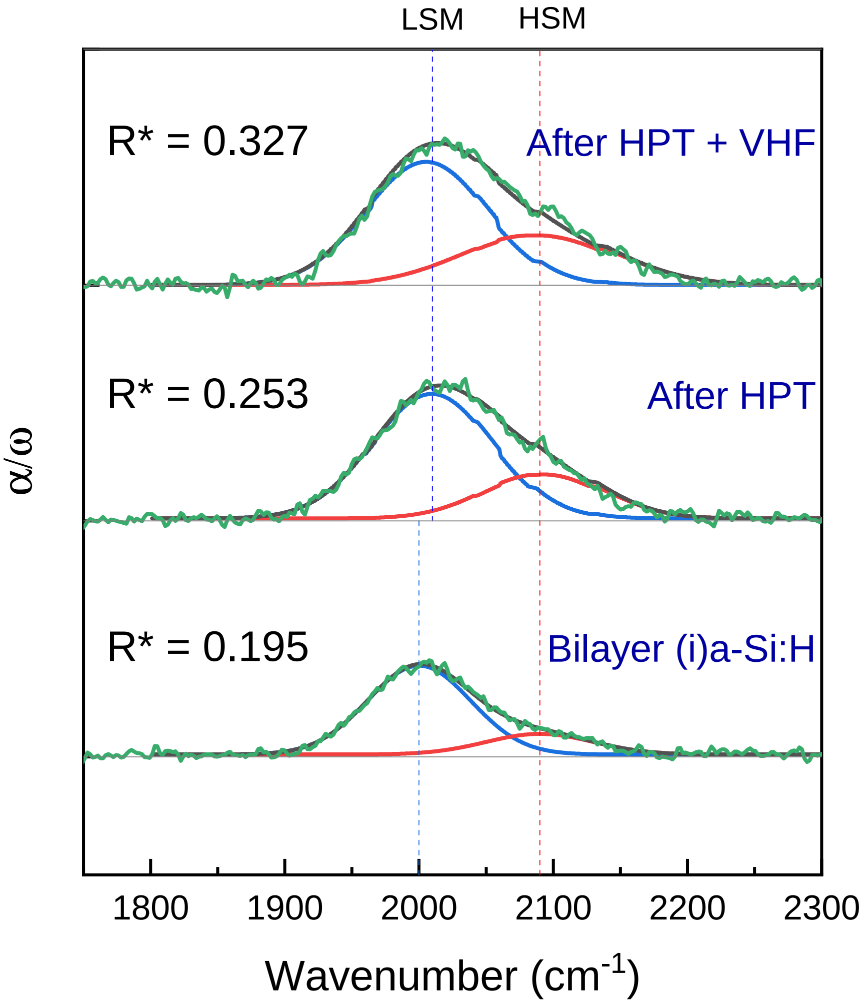

Figure 4.20: Absorption spectra of "A1 + D2" (i)a-Si:H bilayers deposited with and without treatments. Wavenumber shifted from 2000 to 2010 cm^{-1} for LSM. The thickness was adjusted by SE measurements on the glass because (i)a-Si:H layer could be etched around 3.5 nm by HPT.

Similarly, as shown in Figure 4.21, overall relative H content and microstructure factor increase after HPT. This means the density of nanovoids increases and improves surface passivation [23].

However, as seen from Figure 4.21, the R* of STD1+STD2 bilayer is higher than expected. There are also some uncertainties that influence the accuracy of H content and R*. The experimental reasons could mainly come from the instability during the deposition process, or thickness variations resulting in inaccuracies in the calculated spectra. Additionally, measuring FTIR on randomly textured wafers rather than flat wafers and the manual baseline removal in FTIR analysis could introduce uncertainties as well.

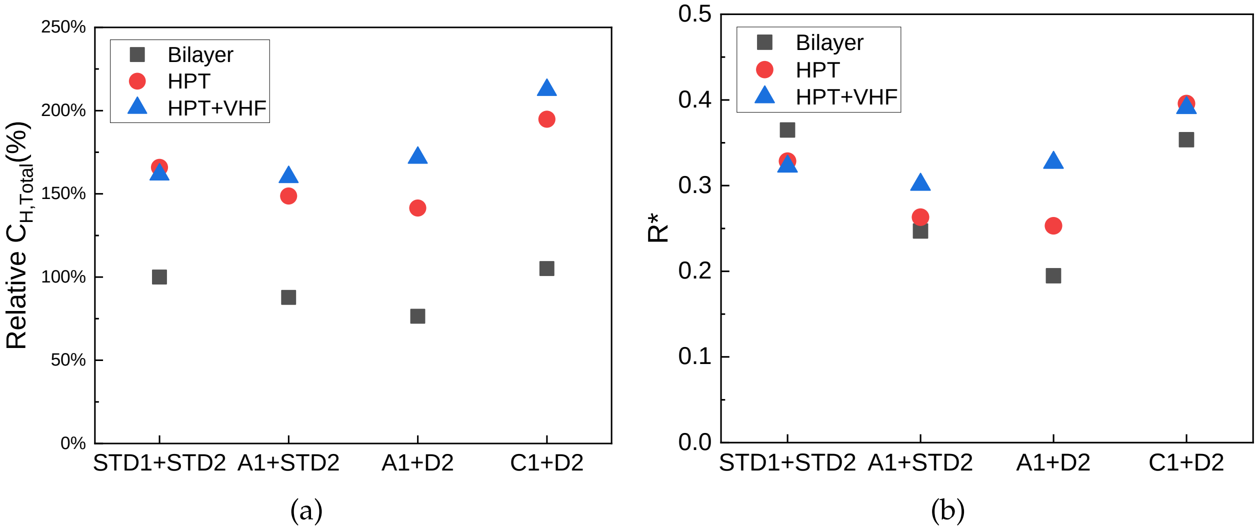

(a) (b)

Figure 4.21: (a) Relative overall H content $C_{H,Total}$ and (b) Microstructure factor R* of different samples with and without treatments. The standard sample without treatments was set as a reference of $C_{H,Total}$ = 100%

4.3 Summary

Within this chapter, aiming at constructing bilayers with i1 layers being H-rich and void-rich and i2 layers being dense for delivering optimized passivation quality, a database focusing on the microstructure factor R* of intrinsic a-Si:H was established. It incorporated various PECVD deposition parameters, including combinations of pressure, power, and dilution ratio. With higher power and pressure, the absorption strength of high stretching modes (HSM), as determined by FTIR, exhibited an increase, indicating higher R* and H content. Additionally, a denser a-Si:H film could be achieved through a higher dilution ratio, in which the low stretching modes (LSM) became dominant. These findings provide insight of searching for the range of R*, spanning from 0.193 to 0.805. Higher R* could be obtained by a lower dilution ratio with higher pressure and power density. Conversely, the lowest R* under a high dilution ratio of 5 is achieved. Despite films with high R values can be achieved by increasing both power and pressure, it still needs to consider the non-uniformity issue and practical constraint of deposition control time for growing approximately 1 nm deposition layer on textured wafers. Moreover, a further increase in pressure could potentially decrease the deposition rate while simultaneously contributing to a more H-rich and void-rich film.

Based on the established database, a series of (i)a-Si:H with various R* from 0.205 to 0.732 has been selected to optimize the structure of (i)a-Si:H bilayer. It has been found that a thickness of 1 nm underdense i1 layer combing with 9 nm of i2 layer on the textured wafer was optimal for surface passivation. The void-rich i1 layer, characterized by higher R* and rich H content, could effectively suppress the dangling bonds and prevent epitaxial growth. Conversely, the dense i2 layer deposited with hydrogen-diluted plasma capped on the top, constrained H within i1 layer, further contributed to better passivation. Those combinations of layers improved the lifetime greatly from 2 ms to 7.5 ms.

Despite various passivation qualities enabled by various bilayer structures (varied from 2 ms to 7.5 ms), after HPT treatment, the lifetime of all bilayer structures increased drastically to 17 ms, accompanied by increases in both H content and R*. That is, the differences in lifetime among various bilayers are not significant, which may indicate the passivation could be saturated after HPT. Overall, surface passivation is enhanced with the combination of i1 with a higher R* and i2 with a lower R*. However, the selection of bilayer is still to be optimized through the aspect of carrier transport, which will be discussed in Chapter 5.

However, the passivation trend after VHF treatment was not clear. It is expected to have a constant passivation improvement after VHF. This could potentially be the cause of the instability in the PECVD deposition tool.

5 Fabrication of FBC-SHJ solar cells

This chapter applies the optimized (i)a-Si:H bilayer to the fabrication of FBC-SHJ solar cells and aims to balance surface passivation and carrier transport. First, the flowchart of the manufacturing process has been introduced. For the promising bilayer combinations identified in Chapter 4, they were implemented into solar cells for performance testing. Based on the current-voltage (I-V) characteristics and series resistance of the resulting FBC-SHJ solar cells, further optimization and selection for layers composing the (i)a-Si:H bilayer were carried out. The impacts of i1 and i2 layers on the performance of the solar cell were investigated. The influence of applying HPT and VHF treatment for solar cells was also discussed.

5.1 Fabrication process

5.1.1 Flowchart of FBC-SHJ solar cell manufacture process

The flowchart of manufacturing the FBC-SHJ solar cell is shown in Figure 5.1. Figure 5.2 illustrated the sketch of FBC-SHJ solar cell.

For the process of solar cell fabrications, N type (100) Topsil wafers were textured by 5% TMAH solution into (111) surface orientation and cleaned by 3 times of NAOS. The details of the pre-deposition process could be found in Section 3.1. During PECVD deposition, the (i)a-Si:H/n layer stacks were first deposited in Amigo. To minimize contamination, a strategic choice was made to deposit the n-type doped layers before the p-type doped layers. This approach was taken due to the higher relative atomic mass of phosphorus (P) compared to boron (B), making it less prone to diffusing into the intrinsic layer and the bare wafer. The specific deposition parameters and layer thicknesses for the doped layers were referenced from [11] and [22].

In this thesis, ITO was deposited on the wafer for both sides and patterned by hard masks, as shown in Figure 5.3. Then, the solar cell precursors were annealed in the oven at 180 °C for 5 min. The effective lifetime was monitored after each steps to assess the passivation quality of the precursor. For metallization, copper electro-plating was employed to create the front metal contacts, while Ag was thermally evaporated on the rear side. To enhance light absorption, a 100 nm SiO_x layer was applied on top of the cell in conjunction with the ITO layer. The performance of this double-layer anti-reflection coating is evaluated in section Section 5.1.2. Detailed descriptions related to the deposition tools and metalization procedures can be found in Section 3.2.

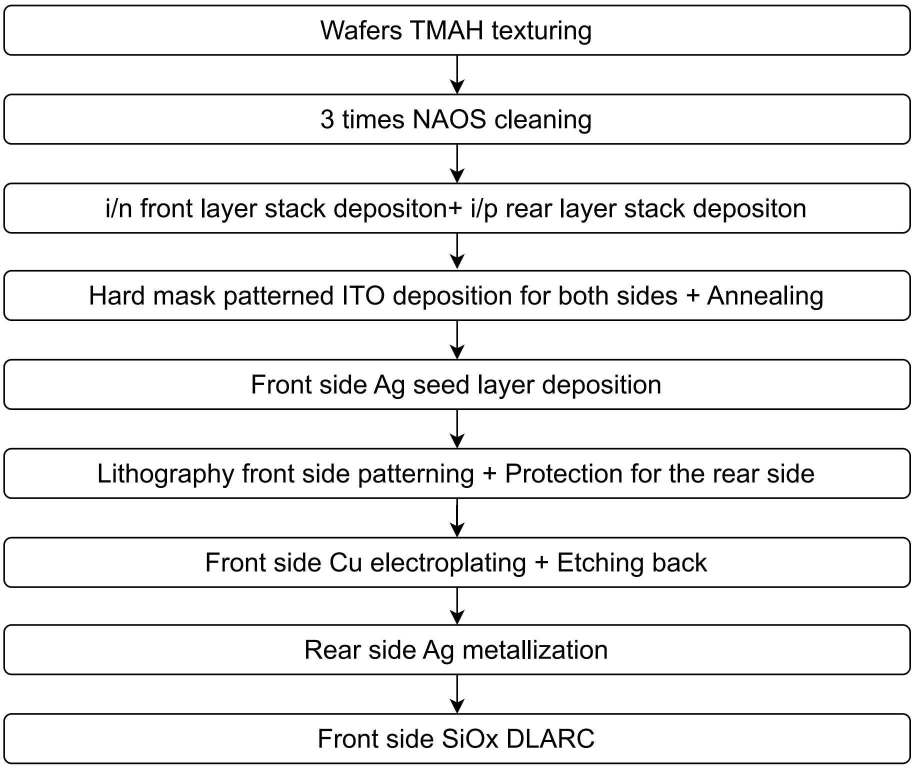

Figure 5.1: Flowchart of FBC-SHJ solar cell fabrication.

The finalized FBC-SHJ solar cell after fabrication was shown in Figure 5.4. Each wafer contains 6 identical cells (dies) with each cell having an active area of 3.86 cm^2. To assess the performance of the solar cells, various parameters including J-V characteristics, pseudo-fill factor (pseudo-FF), SunsVoc, external quantum efficiency (EQE), and reflectance were acquired through measurements and subjected to analysis. Detailed explanations regarding the measurement tools can be found in Section 3.3.

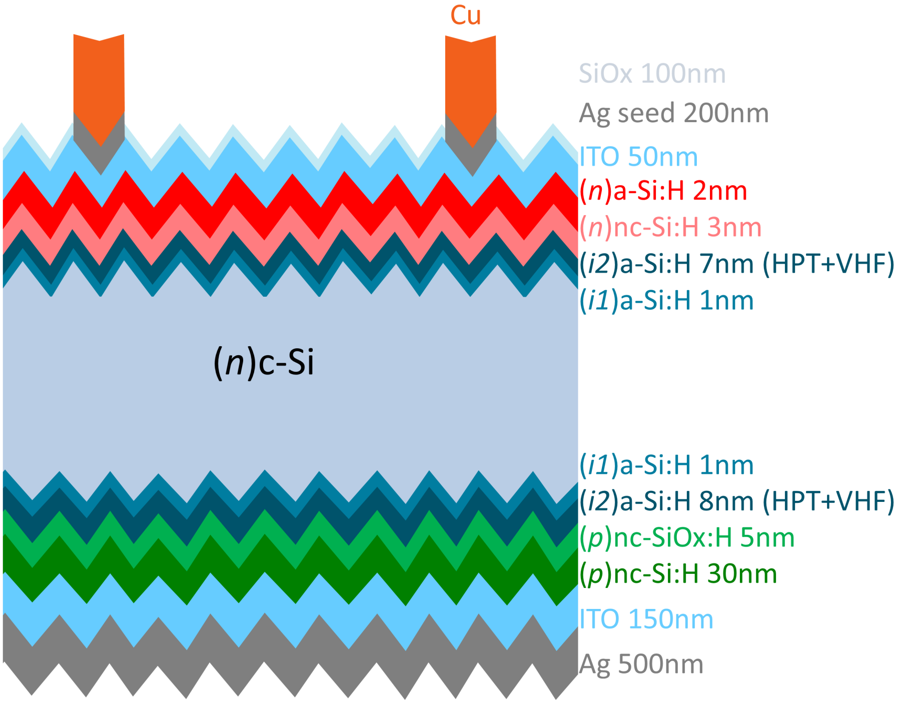

Figure 5.2: Schematic illustrations of the FBC-SHJ solar cell [22]. “7 nm” and “8 nm” refers to the thickness of the i2 layer before HPT and VHF treatments. Around 3.5 nm of the i2 layer will be etched away after treatments.

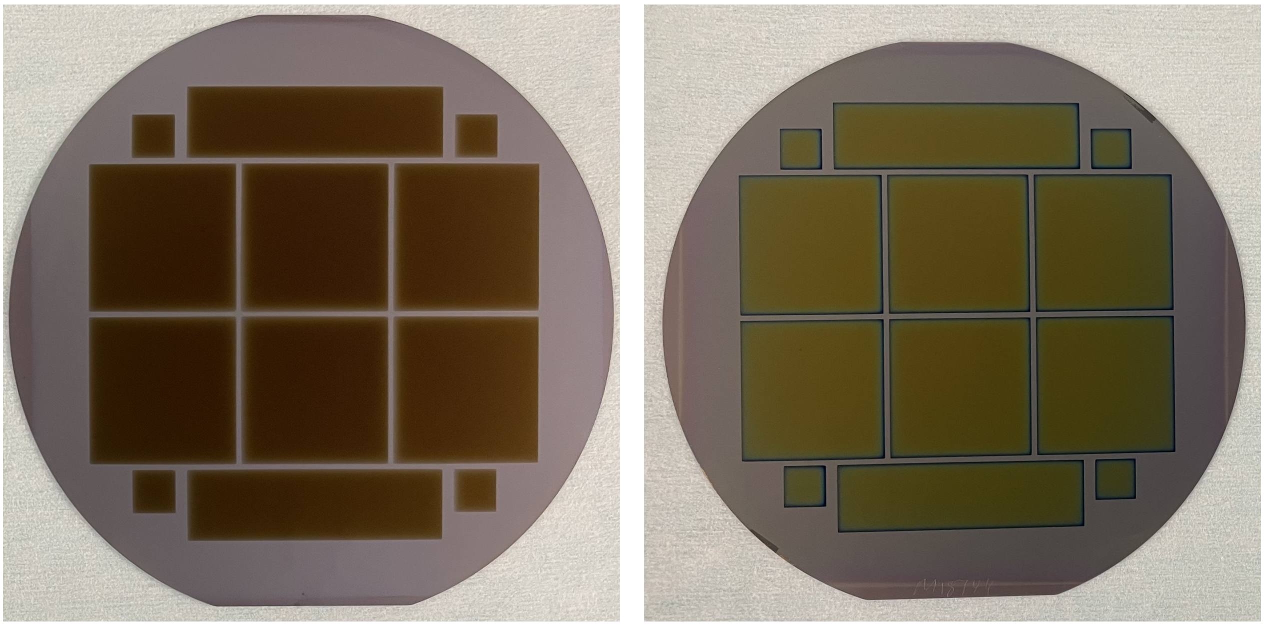

(a) (b)

Figure 5.3: The FBC-SHJ solar cell precursor after ITO deposition: (a) the front side, and (b) the rear side.

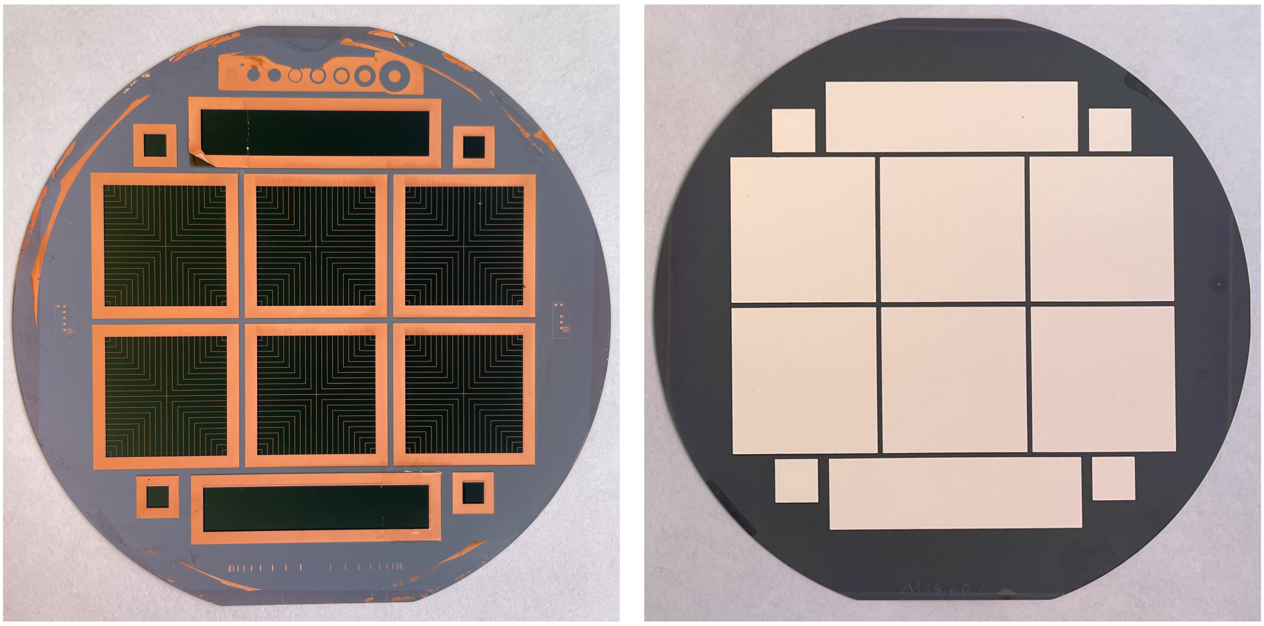

(a) (b)

Figure 5.4: The finalized FBC-SHJ solar cell after fabrication: (a) the front side, and (b) the rear side. HPT and VHF treatment were optionally applied.

5.1.2 Impact of SiO_x as double-layer anti-reflection coating

The reflection losses could be reduced effectively through the combined utilization of SiO_x and ITO as a double-layer anti-reflection coating.[73]. The effect of the additional SiO_x on the solar cell performance has been evaluated. In Figure 5.5, the external quantum efficiency (EQE) and 1 - R curves of the standard FBC-SHJ solar cells were compared before and after the implementation of 100 nm SiO_x layer. The addition of the SiO_x layer effectively reduces the reflectance losses, resulting in an increase in EQE mainly in the wavelength of 550 nm - 1100 nm. This contributes to an increase in J_{SC} by 1.4 mA/cm^2, leading to an overall efficiency improvement of 0.9%. Therefore, in this thesis, SiO_x was applied as the final step in the solar cell fabrication process.

5.1.3 Preliminary bilayer selection

The solar cell performance of well-passivating bilayer structures, which were optimized in Chapter 4, has been evaluated. For the i1 layer, A1 with R* = 0.409 and C1 with higher R* = 0.732 were first selected. For the i2 layer, D2 with R* = 0.205 was chosen. The deposition parameters for these layers were provided in Table 5.1.

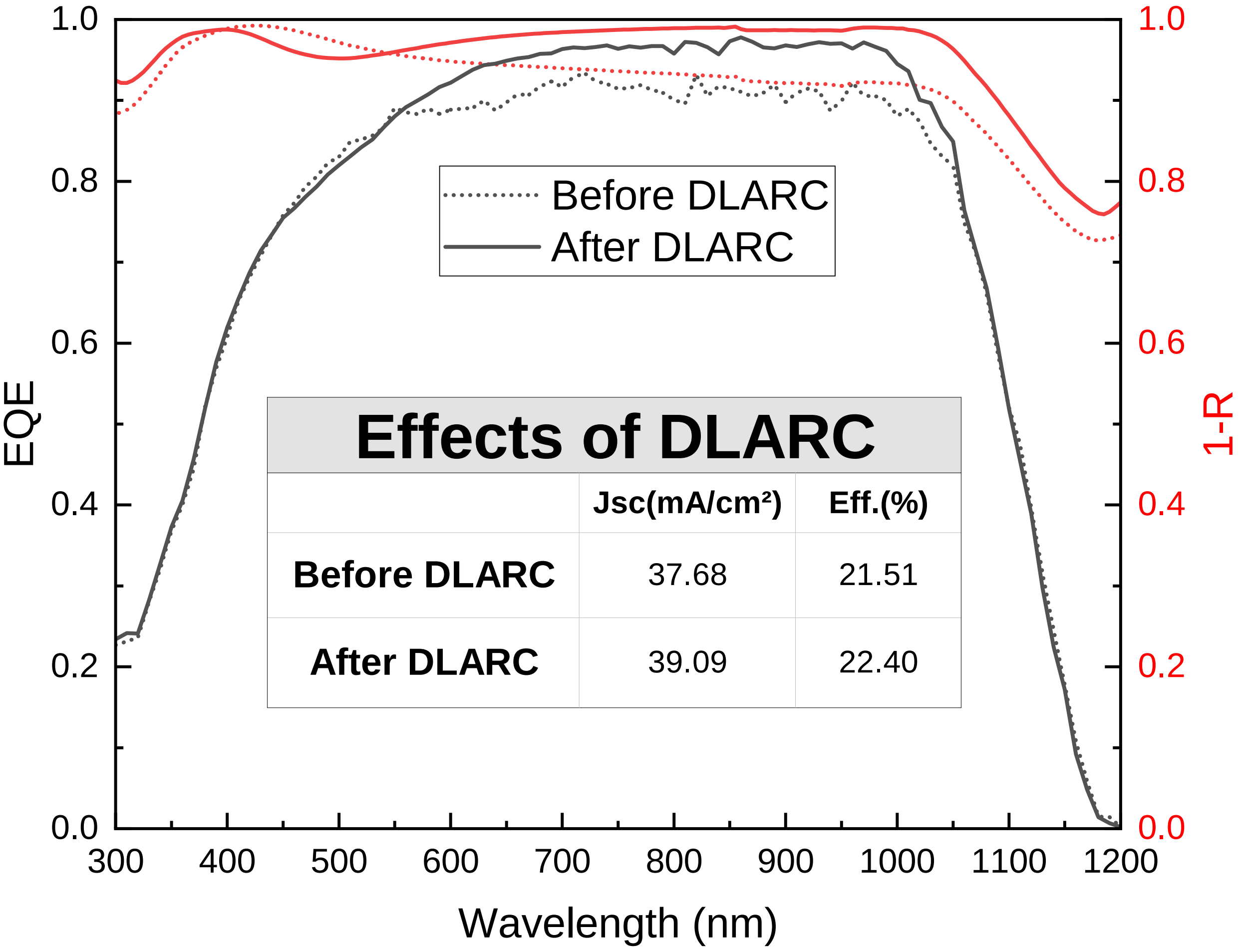

Effects of DLARC

	Jsc(mA/cm²)	Eff.(%)
Before DLARC	37.68	21.51
After DLARC	39.09	22.40

Figure 5.5: External quantum efficiency (EQE) and 1 - R curves of the standard FBC-SHJ solar cells before and after SiO_X as DLARC deposited on the top.

Table 5.1: Deposition parameters and properties of the selected (i)a-Si:H layers on FBC-SHJ solar cell fabrication.

Parameters	Dilution Ratio H_2/SiH_4	Pressure mbar	Power W	R* (-)	Non-uniformity (-)	Deposition time[1] (s)
Standard i1	0	0.7	3	0.261	4%	9 (1 nm)
A i1	3	1.9	8	0.409	7%	5 (1 nm)
C i1	1	2.8	8	0.732	9%	3 (1nm)
Standard i2	3	1.4	3	0.314	7%	85 (8 nm)
D i2	5	1.4	3	0.205	5%	110 (8 nm)

Figure 5.7 compares the J-V parameters of the designed FBC-SHJ solar cells with standard (i)a-Si:H bilayer solar cells. The spread of the box of "A1 + D2" reflects non-uniformity during the deposition process. Compared with standard solar cells, FF

---

[1] The deposition times specifically refer to the deposition time for the p-side i2 layer with a thickness of 8 nm, and the i1 layer with a thickness of 1 nm on the textured side. The deposition time for the n-side i2 layer, with a thickness of 7 nm, should be adjusted according to its thickness variation. The films were deposited in Amigo with the auto-running recipe.

dropped significantly, leading to a lower overall efficiency for both types of solar cells. This is because the actual deposited A1 and C1 layer thickness is thicker than 1 nm, taking into consideration the time required for plasma ignition and shutdown in Amigo. Therefore, the series resistance for the solar cell increases and deteriorates the FF (see in Figure 5.6) [24].

To confirm the thickness, A1 and C1 layers were redeposited onto flat glass substrates using the same deposition time, and their thicknesses were measured using Spectroscopic Ellipsometry (SE). The actual thickness of deposited A1 and C1 were 2.01 nm and 2.61 nm (aimed at 1 nm), respectively. As a result, solar cells endowed with the "A1 + D2" bilayer were restructured through manual deposition control, as indicated by the yellow bar in the graph. To minimize variables, instead of symmetric alteration, only the bilayer deposition on the p-side was modified.

The summarized averaged J-V parameters are shown in Table 5.2. Compared with the standard samples, the adjusted "A1 +D2" indicates a higher V_{OC} (716 mV), which could be contributed to the improved passivation. However, the FF still experiences a decrease of approximately 2.5% due to the high series resistance of the i1 layer with higher R* (see Figure 5.6 and Figure 5.7). This together contributes to a lower efficiency compared with the standard FBC-SHJ solar cells. Therefore, there is a trade-off between V_{OC} and FF, and the combination of the bilayers should be re-optimized.

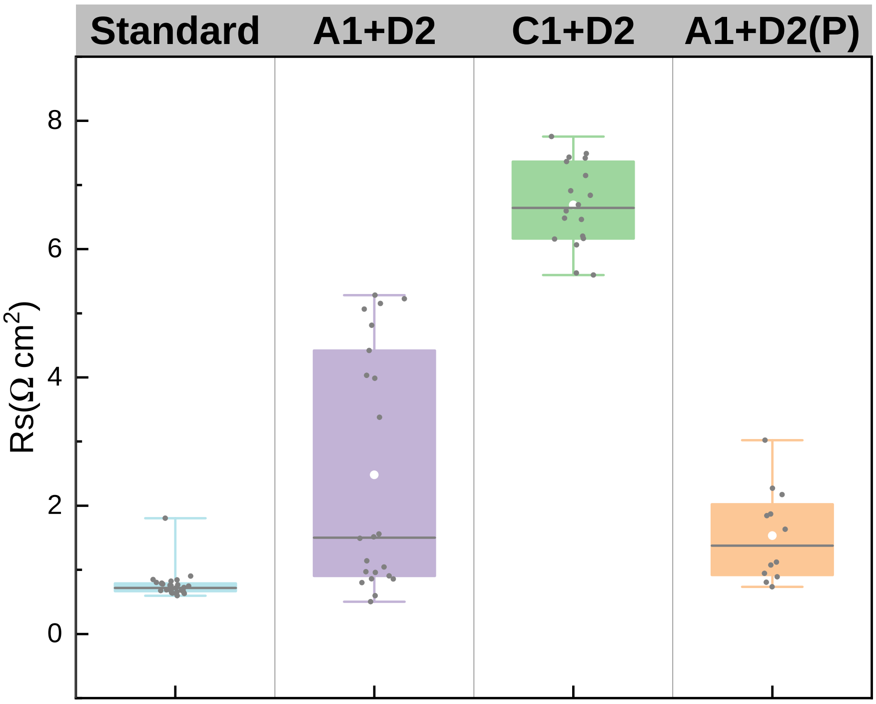

Figure 5.6: Series resistance among different types of solar cells.

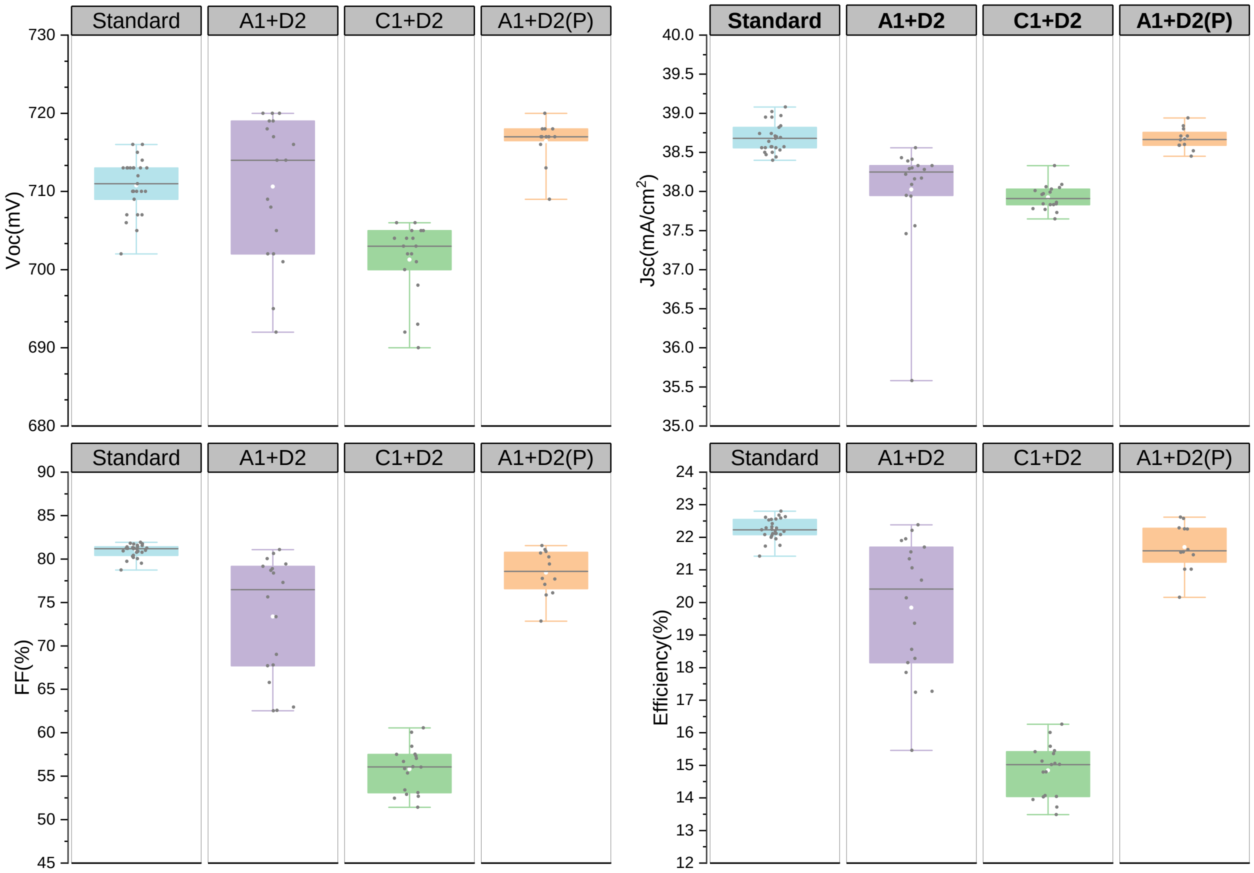

Figure 5.7: J-V parameters of FBC-SHJ solar cells with different (i)a-Si:H bilayers, containing open circuit voltage (V_{OC}), short circuit current density (J_{SC}), fill factor (FF), and efficiency, respectively. "STD" represents the standard i1 + i2 bilayer structure solar cells. The detailed properties could be found in Table 5.1. "A1 + D2 (P)" represents the cells reconstructed bilayer with manual deposition on the p side, while using the same standard bilayer structure on the n side. Solar cells with the same types but fabricated in different wafers were combined in one box. The white dot in the box-and-whisker-plot represents the average.

Table 5.2: The results of the designed bilayer structure FBC-SHJ solar cells compared with the standard cells. The J-V parameters were averaged.

Parameters	V_{OC} mV	J_{SC} mA/cm^2	FF %	Efficiency %
Standard	711	38.68	80.92	22.24
A1 + D2 (p-side)	716	38.67	78.43	21.70

5.2 Optimization of FBC-SHJ solar cells

According to the results shown in Section 5.1.3, a series of (i)a-Si:H layers were re-selected based on the R* dataset in Figure 4.10 and listed in Table 5.3, considering a controllable deposition time over 5 s for depositing 1 nm on the textured surface.

Table 5.3: Deposition parameters and properties of (i)a-Si:H layers in variations of R* from 0.205 to 0.560.

Parameters	Dilution Ratio (H_2/SiH_4)	Pressure (mbar)	Power (W)	R* (-)	Non-uniformity (-)	Deposition time[2] (s)
STD i1	0	0.7	3	0.261	4%	9 (Auto)
M i1	3	1.4	3	0.314	7%	11 (Manual)
N i1	3	2	3	0.362	7%	11 (Auto)
X i1	0	0.93	4	0.383	8%	7 (Manual)
Y i1	0	1.4	6	0.407	11%	7 (Manual)
Z i1	0	1.9	8	0.560	12%	6 (Manual)
STD i2	3	1.4	3	0.314	7%	85 (Auto)
D i2	5	1.4	3	0.205	5%	94 (Auto)

5.2.1 Optimization of i1 layer

Based on the previous experiments in Figure 5.7, the adoption of a high R* value of 0.732 in the i1 layer was ruled out. In order to achieve a balance between V_{OC} and FF, the optimal range of R* was explored from 0.314 to 0.560. Figure 5.9 shows the J-V parameters as increasing of R* in the i1 layer.

The passivation results of the solar cell precursors after ITO deposition and annealing as shown in Figure 5.8. The lifetime increased with R* to 14ms (see "X1 + D2")and dropped. Coherently, as presented in Figure 5.9, it is observed a higher V_{OC} increases with the R* to an average of 717 mV (with a maximum of 720 mV) and drops. The increase in V_{OC} is the void-rich and H-rich i1 layer that suppresses the epitaxial growth and thus improves the passivation, which is consistent with the discussion in Chapter 4. The reduction in V_{OC} would probably be: a) The films becoming more void-rich when the microstructure factor grows higher, and potentially introducing defects into a-Si:H [74]; b) The band offsets are too large for collecting holes due to the H-rich layer and therefore hindering the selective transport of holes [24]; c) The c-Si surface is not fully covered when the layer becomes too porous. These are coherent with the decreased lifetime in the case of the "Z1 + D2" precursor. Figure 5.10 shows the same trends of SunsVoc as Voc, indicating the promising potential for "X1 + D2".

As shown in Figure 5.11, the gap between the FF and pFF increases as R* in the i1 layer increases, which is contributed to the series resistance. Figure 5.12 summaries

---

[2] The deposition times specifically refer to the deposition time for the p-side i2 layer with a thickness of 8 nm, and the i1 layer with a thickness of 1 nm on the textured side. The deposition time for the n-side i2 layer, with a thickness of 7 nm, should be adjusted according to its thickness variation. Manual and auto represent whether the layer was deposited manually or with an automatic recipe in Amigo.

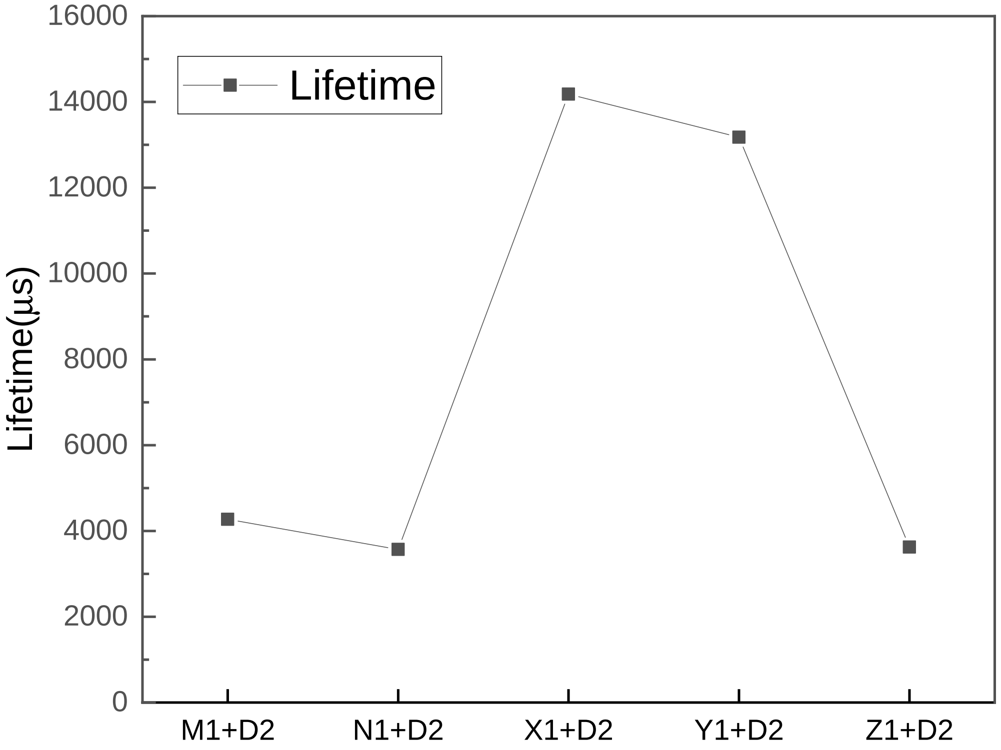

Figure 5.8: Lifetime of FBC-SHJ solar cell precursors as variations of R*. The results were measured after annealing. Only the center point of one wafer was selected for each type of solar cell. From M1 to Z1, the microstructure factor R* of the i1 layer increases.

the series resistance calculated by Equation 3.7. As the R* of the i1 layer increases, the series resistance grows significantly, causing the drop of FF in the solar cells. This could be explained by the holes as the minority carriers encounter greater difficulty to pass through the intrinsic a-Si:H layer with a higher degree of disorder [20], as the valence band offset of the (i)a-Si:H is more sensitive to H content as compared to the conduction band offset [75].

Figure 5.9 shows a slight improvement in J_{SC} with an increase of R* of the i1 layer. EQE and 1-R curves lifted up a little bit at a short wavelength around 400 - 600 nm in Figure 5.13. This could be explained by the bandgap of i1 layer becoming wider with the increase in H content, therefore less parasitic absorption in short wavelength, higher EQE, and J_{SC} is obtained [74]. Another explanation could be a better anti-reflection effect at the short wavelength, which may originate from the varied refractive index of (i)a-Si:H due to their different H content and microstructure properties.

The enhancement in V_{OC}, along with a slight increase in J_{SC} and a tolerable drop in FF, collectively results in an average efficiency of 22.05% of the "X1 + D2" solar cells. This indicates that the optimal i1 layer is X1 with R* value of 0.382. The summarized J-V parameters for both average and best performance results are presented in Table 5.4. Given that the performance may fluctuate between different batches, adopting X1 as the i1 layer choice appears promising.

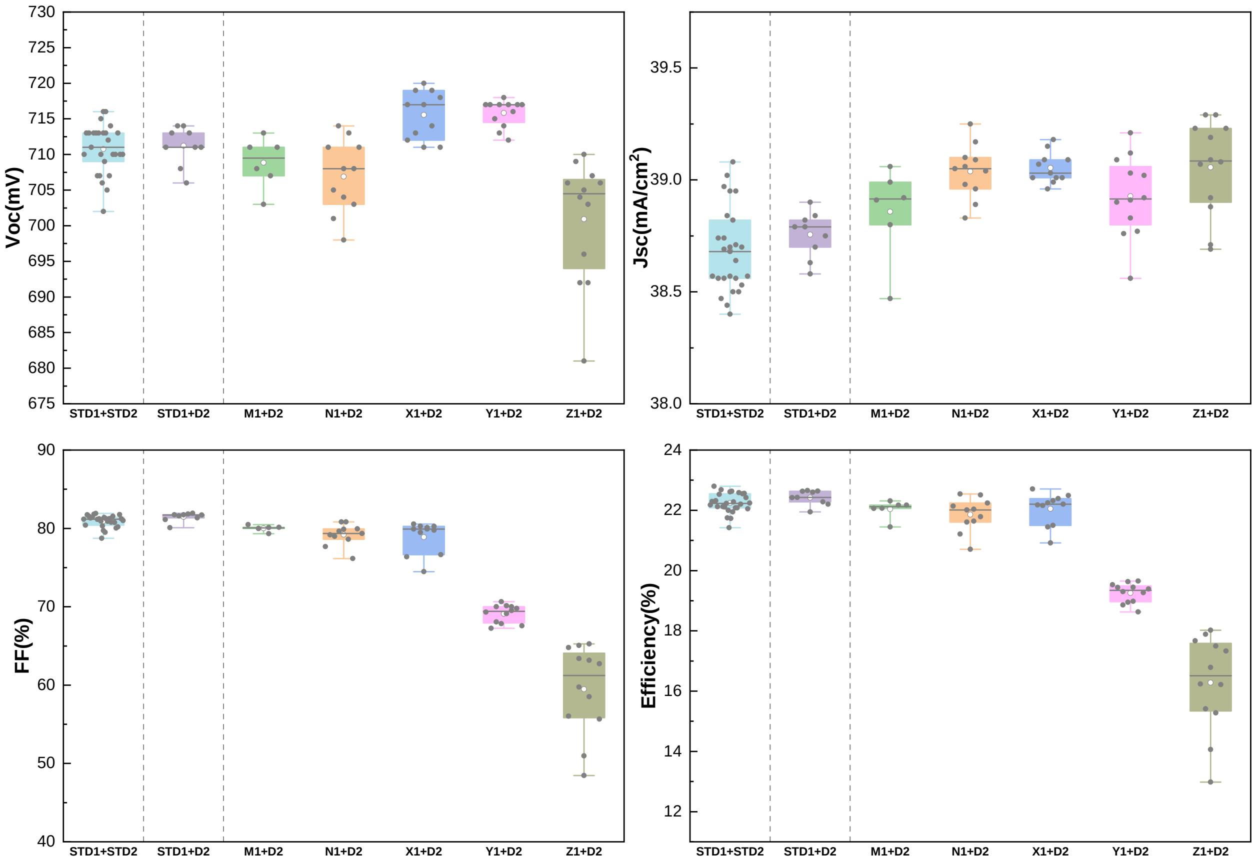

Figure 5.9: J-V parameters of FBC-SHJ solar cells as variations of R*. The standard cells “STD1 + STD2” and “STD1 + D2” cells fabricated in the previous round are included as references. The detailed properties and deposition parameters could be found in Table 5.3. From M1 to Z1, the microstructure factor R* of the i1 layer increases. All non-standard types of cells were only modified on the p side, while keeping the n side the same as standard. Cells within different wafers were combined as in one single bar in the graph for comparative analysis. The white dot in the box-and-whisker-plot represents the average.

Table 5.4: The results of the “X1 + D2” bilayer structure FBC-SHJ solar cells compared with standard cells. The cells were only modified on the p side.

Parameters	V_{OC} mV	J_{SC} mA/cm^2	FF %	Efficiency %
Standard (avg)	711	38.68	80.92	22.24
Standard (best)	716	38.97	81.75	22.80
X1 + D2 (avg)	717	39.05	78.89	22.05
X1 + D2 (best)	720	39.15	80.55	22.71

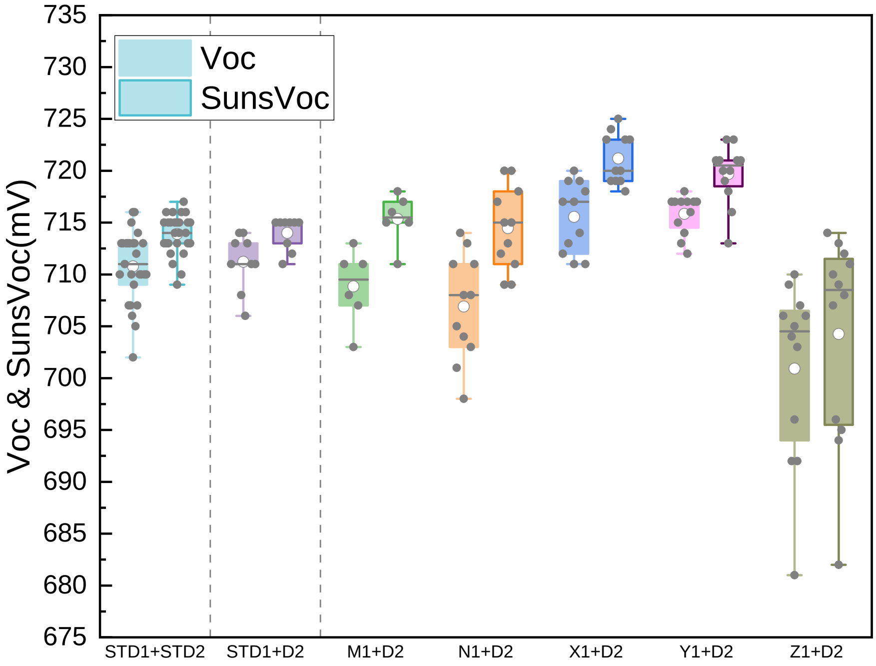

Figure 5.10: V_{OC} (the left bar) and SunsVoc (the right bar) of FBC-SHJ solar cell precursors as variations of R*. From M1 to Z1, the microstructure factor R* of the i1 layer increases.

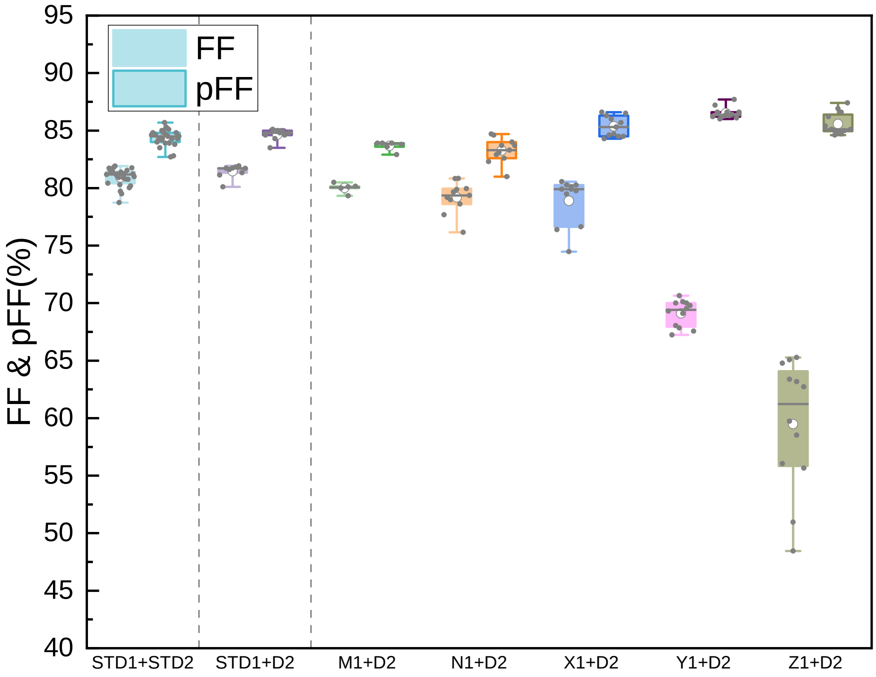

Figure 5.11: FF (the left bar) and pFF (the right bar) of FBC-SHJ solar cell precursors as variations of R*. From M1 to Z1, the microstructure factor R* of the i1 layer increases.

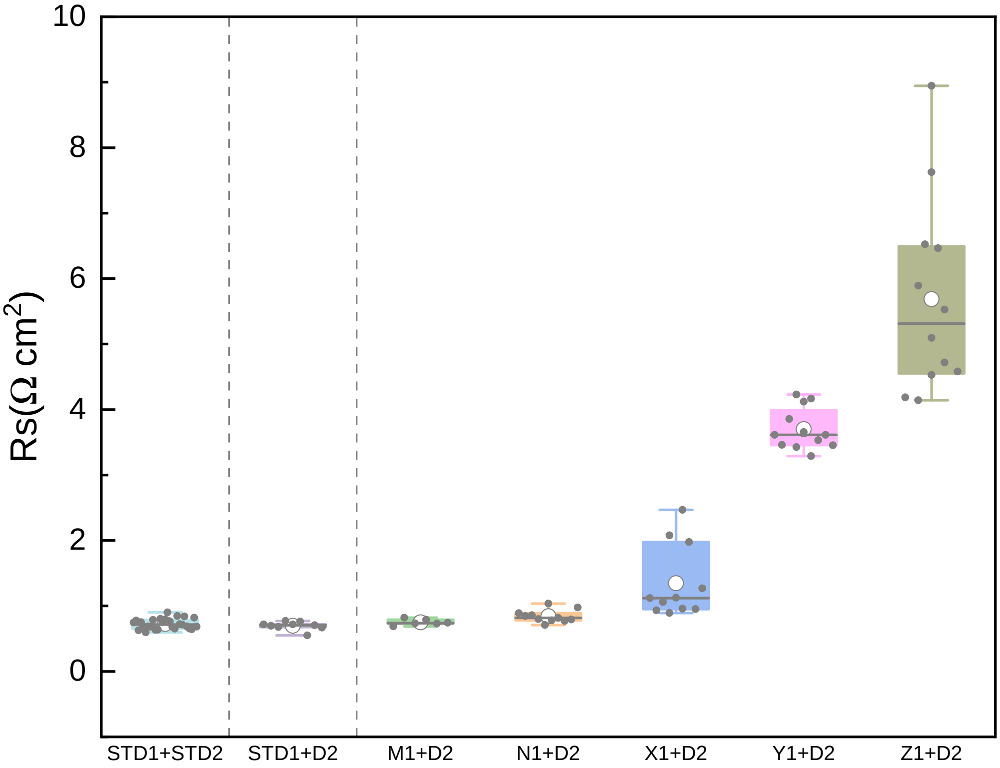

Figure 5.12: Series resistance of FBC-SHJ solar cells as variations of R*. From M1 to Z1, the microstructure factor R* of the i1 layer increases.

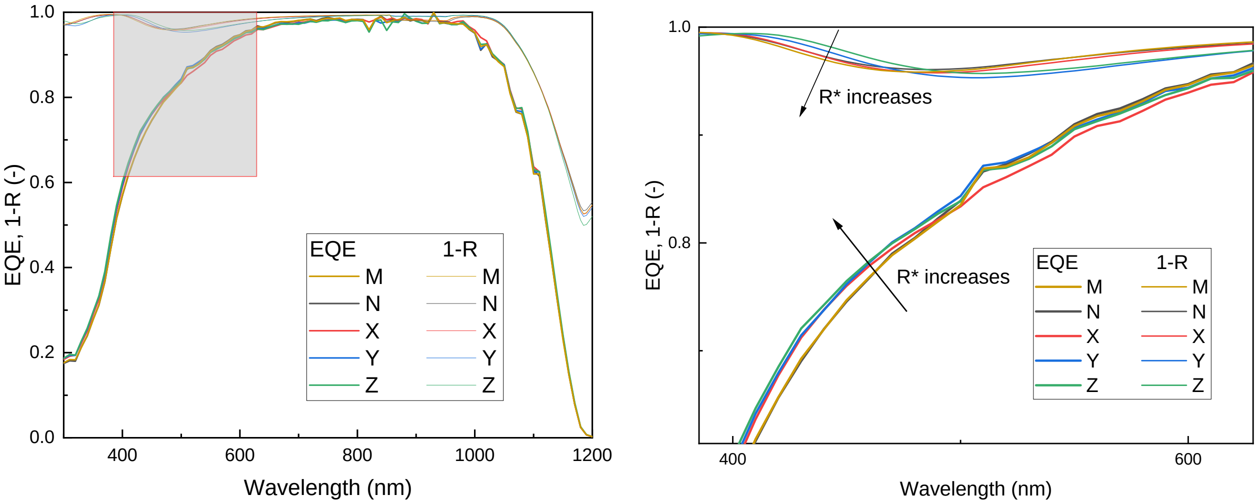

(a)

(b)

Figure 5.13: External quantum efficiency (EQE) and 1 - R curves of FBC-SHJ solar cells as variations of R* in i1 layer. (a) Figure at full wavelength, and (b) enlarged figure at short wavelength.

5.2.2 Optimization of i2 layer

Figure 5.14 shows the J-V parameters and series resistance of FBC-SHJ solar cells fabricated with different i2 layers. With the implementation of D2 on the p side, the V_{OC} and SunsVoc drop, while the FF experiences a modest rise of approximately $0.5\%_{abs}$, and R_S decreases [24]. The decreased series resistance is contributed to the enhancement of the charge carrier when a denser i2 layer with lower defect density is applied [74]. This combined effect leads to a slight improvement in efficiency to 22.72%, as shown in Table 5.5.

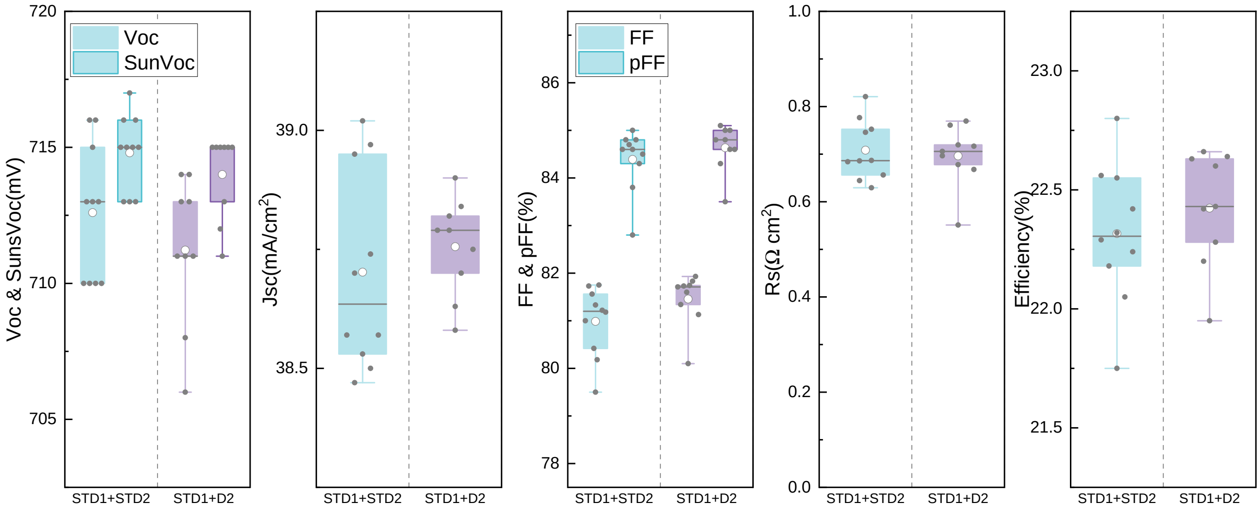

Figure 5.14: J-V parameters, the series resistance of FBC-SHJ solar cells with the change of i2 layer in the same batch. "STD1 + D2" cells were only modified on the p side, while the n side is kept the same as the standard. The detailed properties could be found in Table 5.3. The same type of cells were combined into one box in the graph.

Table 5.5: The results of the "STD1 + D2" bilayer structure FBC-SHJ solar cells compared with standard cells. The J-V parameters were averaged. In this case, "STD1 + D2" cells were only modified on the p side.

Parameters	V_{OC} mV	J_{SC} mA/cm^2	FF %	Efficiency %
Standard (avg)	713	38.70	80.99	22.32
STD1 + D2 (avg)	711	38.76	81.46	22.42

5.2.3 Effects of i1 and i2 layers

In the previous optimization, X1 and D2 were proved as the optimal bilayer combinations. In this section, the bilayer structure was changed on both sides during the fabrication of FBC-SHJ solar cells, and the impact of modifying individual layers was studied without employing HPT and VHF treatment.

Figure 5.15 shows the lifetime of the precursors after the complete PECVD depositions, which is coherent with the passivation test of the bilayer (a)-Si:H in Figure 4.18. The passivation of the precursors improved with the implementation of an underdense X1 layer or a dense D2 layer. The combination of the "X1 + D2" precursor gives the highest lifetime of 7.5 ms.

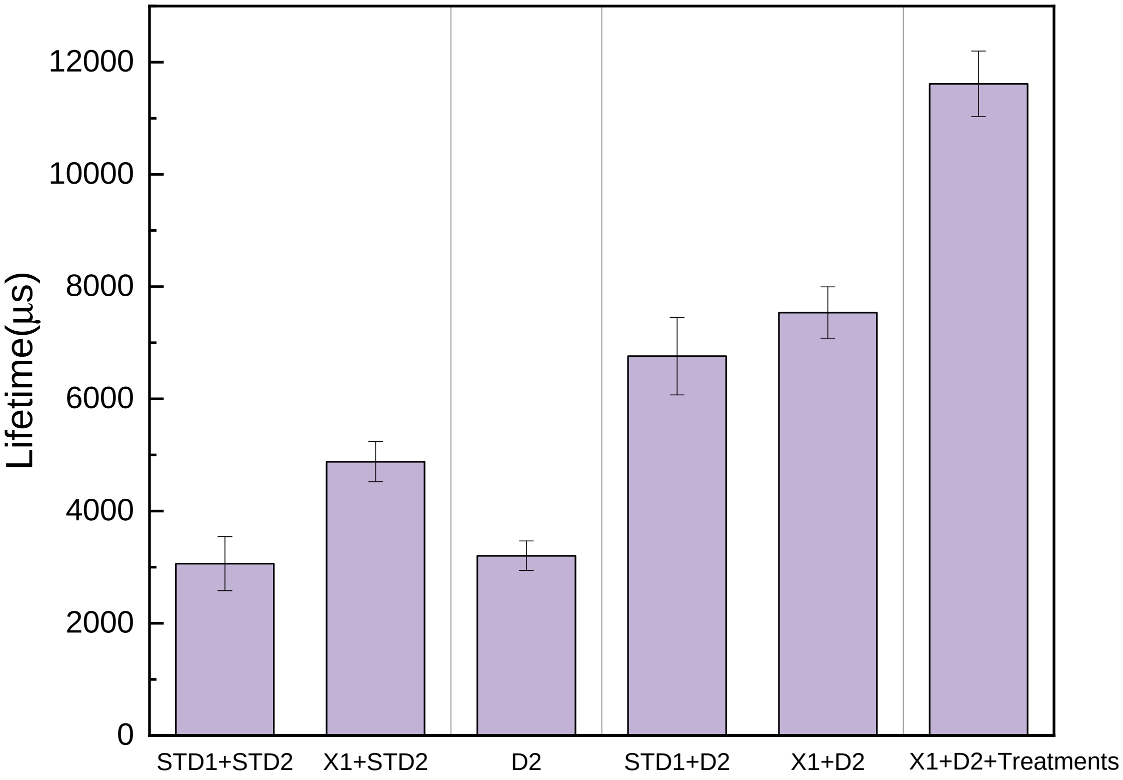

Figure 5.15: Lifetime of the solar cell precursors after complete PECVD depositions. The bilayer structure of the cells was changed symmetrically and without treatments after (i)a-Si:H deposition except for the last column. In the measurement of lifetime, a total of 6 points were sampled on each wafer (2 points in the center and 4 points near the center). The error bars represent the fluctuations in passivation within each wafer.

As shown in Figure 5.16, implementing X1 layer gives an over 15 mV rise in V_{OC}, compared with D2 without i1 layers. This is consistent with the observed improved surface passivation in Figure 5.15. Compared with the cells with STD1, the V_{OC} and SunsVoc of the cell with X1 should be higher as shown in previous results in Figure 5.9. However, one of the "STD1 + STD2" cells reaches a V_{OC} over 720 mV, mainly because the precursor reaches the highest lifetime of 15 ms even without treatment. This might be ascribed to the instability of PECVD deposition tool.

It is also observed that when using D2 instead of STD2, both V_{OC} and SunsVoc deteriorate, as shown in Figure 5.17. However, as a trade-off, the series resistance (R_S) is reduced, helping to counteract the elevated series resistance associated with the incorporation of the X1 layer. This brings the R_S for "X1 + D2" to a comparable level with standard solar cells (as seen in Figure 5.18). This decrease in R_S from 1.6 $\Omega \cdot cm^2$ to 0.91 $\Omega \cdot cm^2$ contributes to the enhancement of the fill factor from 78.65% to 80.53% [24]. In addition, the denser i2 could be a protector to protect the well-passivated (i1)a-Si:H/c-Si interface from the defects in dopant layer [24], [76].

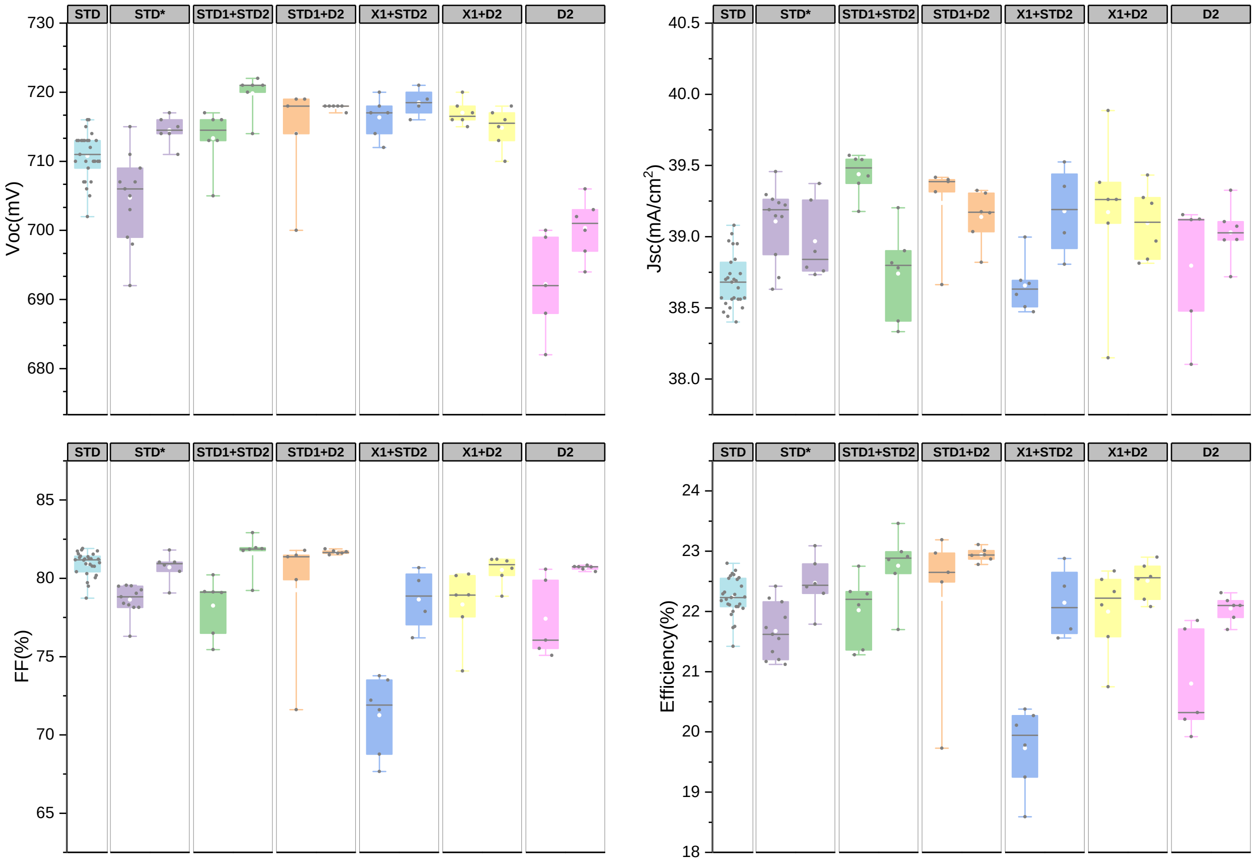

Figure 5.16: J-V parameters of FBC-SHJ solar cells with different (i)a-Si:H bilayers. “STD” represents the standard i1 + i2 bilayer structure solar cells with treatments in previous batches. “STD*” represents the current batch of standard structure with HPT + VHF treatments. All the other bars represent the corresponding bilayer structure solar cells without treatments. Due to the instability of Amigo, solar cells of the same type were grouped into two bars based on batches produced on different days. The comparison between different solar cells can be analyzed either from the left box or the right box.

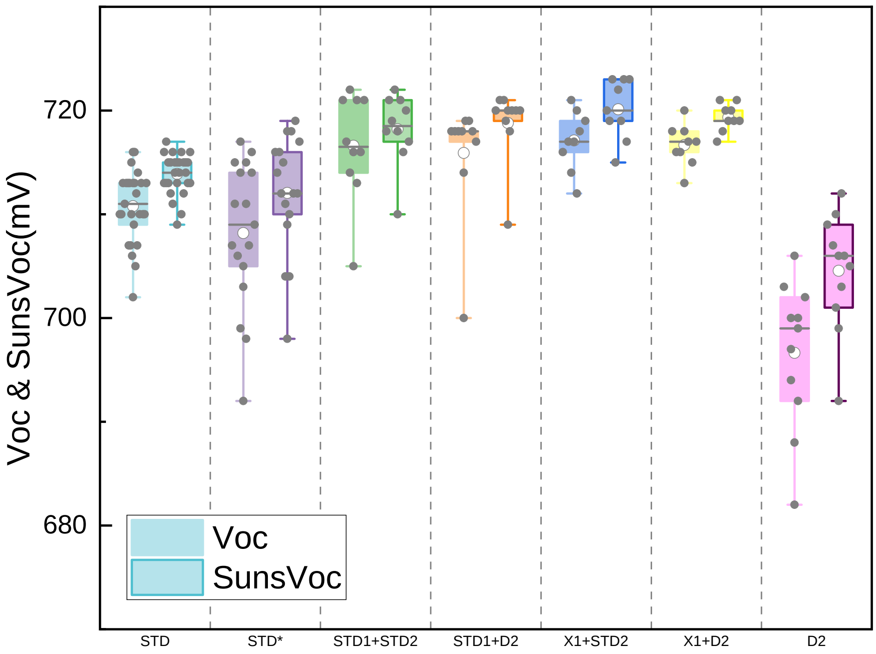

Figure 5.17: V_{OC} and SunsVoc of FBC-SHJ solar cells with different (i)a-Si:H bilayers. All solar cells with the same type were summarized into one bar.

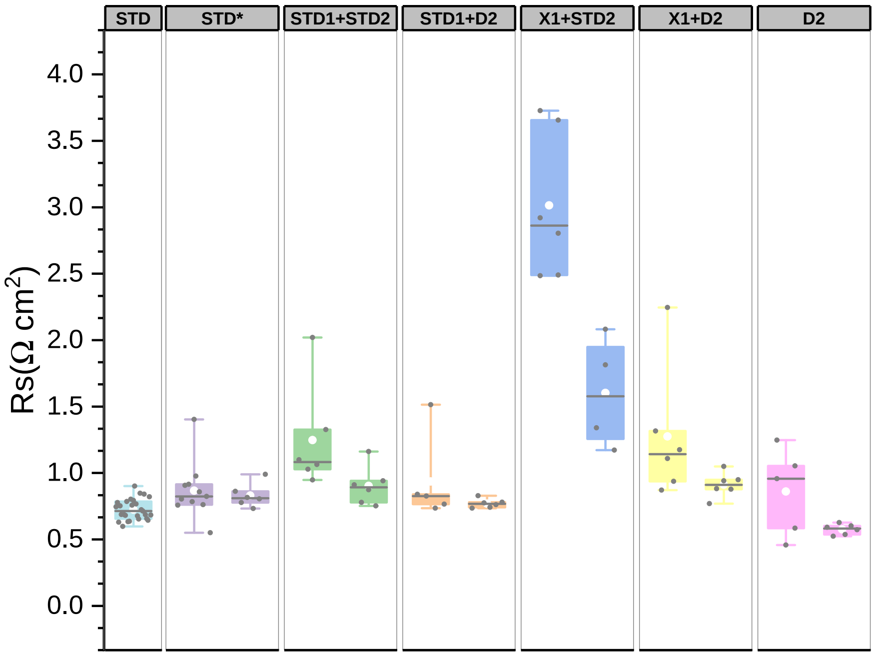

Figure 5.18: Series resistance of FBC-SHJ solar cells with different (i)a-Si:H bilayers.

5.2.4 Effects of HPT and VHF treatments

The effect of HPT and VHF treatments is shown in Figure 5.19. V_{OC} deteriorated after treatment, and FF improved because of the series resistance reduced. This is coherent with the findings in [11]. The drop in V_{OC} could be caused by the epitaxial layer at the a-Si:H/c-Si interface after HPT [18]. The combined effect results in the "X1 + D2" bilayer configuration with treatments achieving an improved average efficiency of 22.16% compared to an average efficiency of 21.67% standard solar cell in the same batch, as detailed in Table 5.6. The best performance of the cell reaches 23.23% in another batch and the EQE, 1-R, and J-V curves presented in Figure 5.22.

Due to the instability of PECVD tools, there are always some fluctuations from batch to batch in terms of solar cell performance. Throughout the experiments, random tilting of the holder during transfer into different DPC chambers is often noticed, potentially causing non-uniformity within each wafer. This results in a larger error bar, rendering the results less evident for analysis. Furthermore, there are instances where the lifetime for certain solar cell precursors remains within the range of 2 ms to 5 ms, in contrast to the standard solar cell precursors with a lifetime of 10 ms, which were produced in the previous round. This could be attributed to the instability of the VHF chamber, which had, sometimes, non-uniform distribution of plasma. However, this leads to the conclusion that even without the application of HPT and VHF treatments, the manufactured FBC-SHJ solar cells could still be comparable and in some cases, even outperform the cells that underwent these treatments.

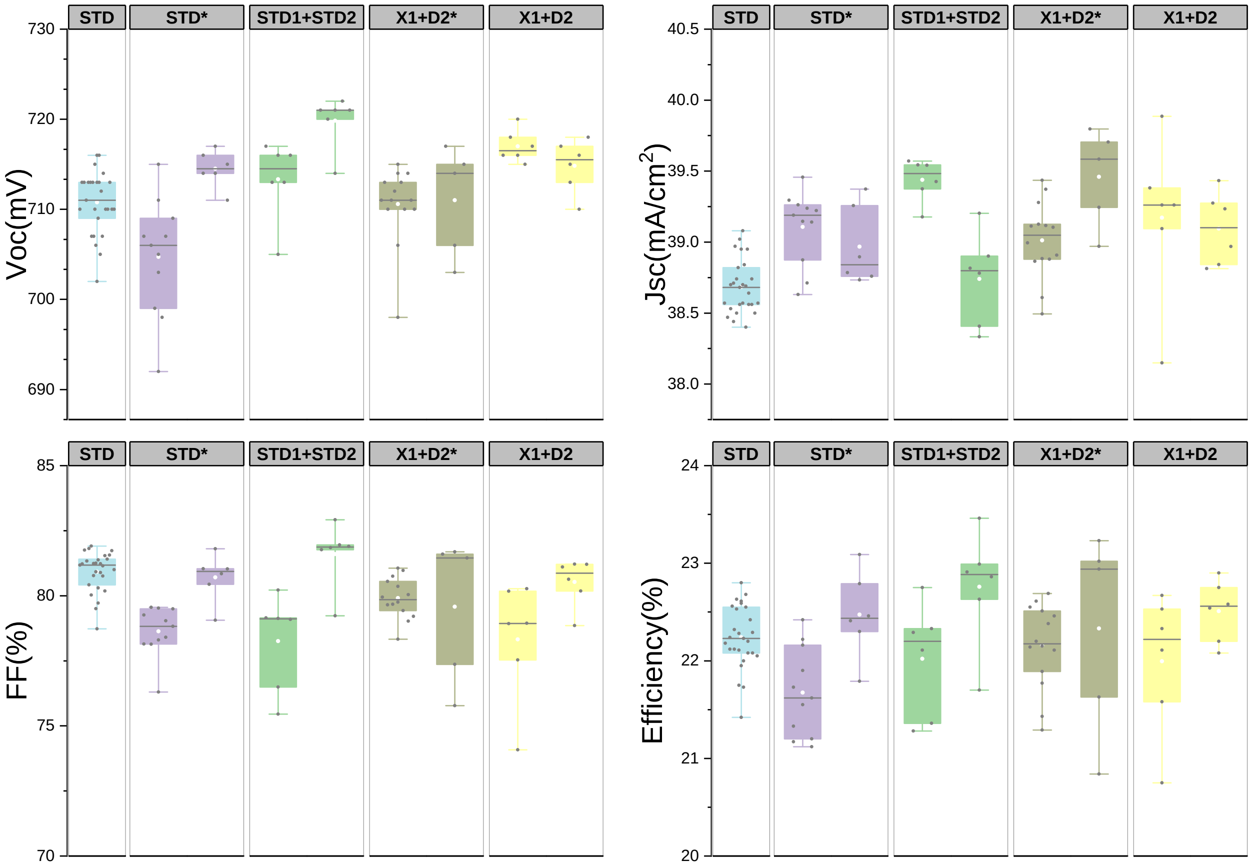

Figure 5.19: J-V parameters of FBC-SHJ solar cells with different (i)a-Si:H bilayers. “STD” represents the standard i1 + i2 bilayer structure solar cells with treatments in previous batches as a reference. “STD*” and “X1 + D2*”represent the solar cells with treatments. Due to the instability of Amigo, solar cells of the same type were grouped into two bars based on batches produced on different days.

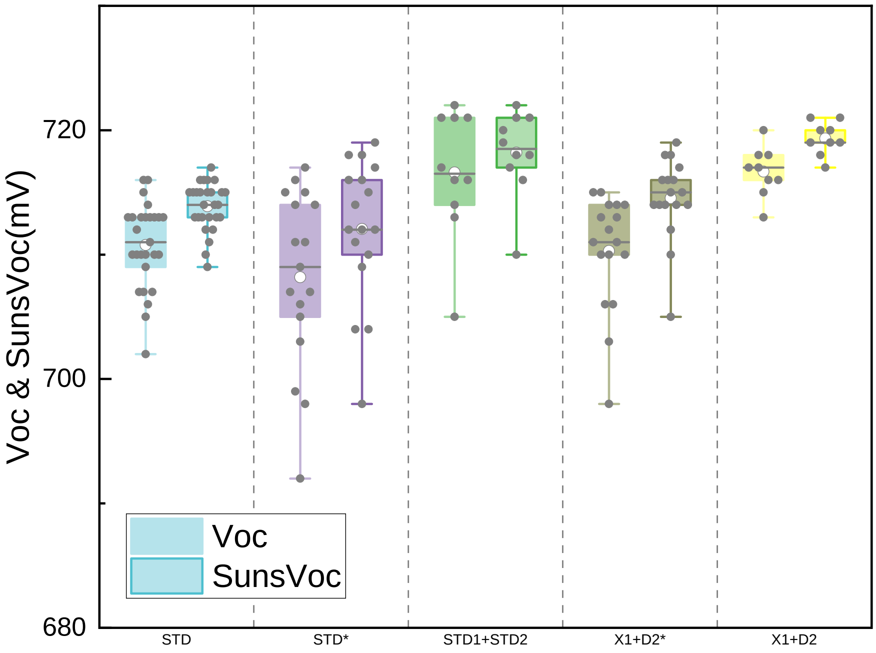

Figure 5.20: V_{OC} and SunsVoc of FBC-SHJ solar cells with different (i)a-Si:H bilayers with and without treatments. All solar cells with the same type were summarized into one bar.

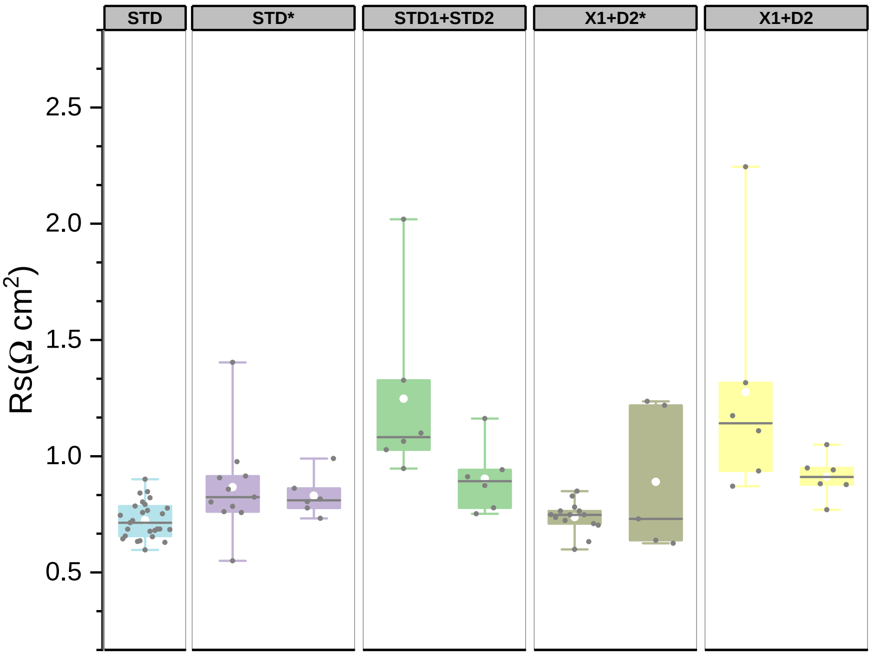

Figure 5.21: Series resistance of FBC-SHJ solar cells with different (i)a-Si:H bilayers with and without treatments. The average of the cells taken from one batch of wafers.

Table 5.6: The J-V parameter results of the "X1 + D2" bilayer structure FBC-SHJ solar cells compared with standard cells with and without treatments. The superscript number 1 and 2 after average or best indicate different batches of wafers, 0 indicates previous results in the last two cycles as reference.

Parameters	V_{OC} mV	J_{SC} mA/cm^2	FF %	Efficiency %
Standard + Treatments (avg^0)	711	38.68	80.92	22.24
Standard + Treatments (avg^1)	705	39.11	78.63	21.67
X1 + D2 + Treatments (avg^1)	**711**	**39.01**	**79.91**	**22.16**
Standard + Treatments (avg^2)	715	38.97	80.70	22.47
Standard + Treatments (best^2)	714	39.37	81.80	23.09
X1 + D2 + Treatments (avg^2)	**711**	**39.46**	**79.57**	**22.33**
X1 + D2 + Treatments (best^2)	**717**	**39.70**	**81.60**	**23.23**
Standard w/o treatments (avg^2)	719	38.74	81.60	22.78
Standard w/o treatments (best^2)	722	39.20	82.92	23.46
X1 + D2 w/o treatments (avg^2)	**715**	**39.09**	**80.53**	**22.50**
X1 + D2 w/o treatments (best^2)	**721**	**39.35**	**80.67**	**22.88**

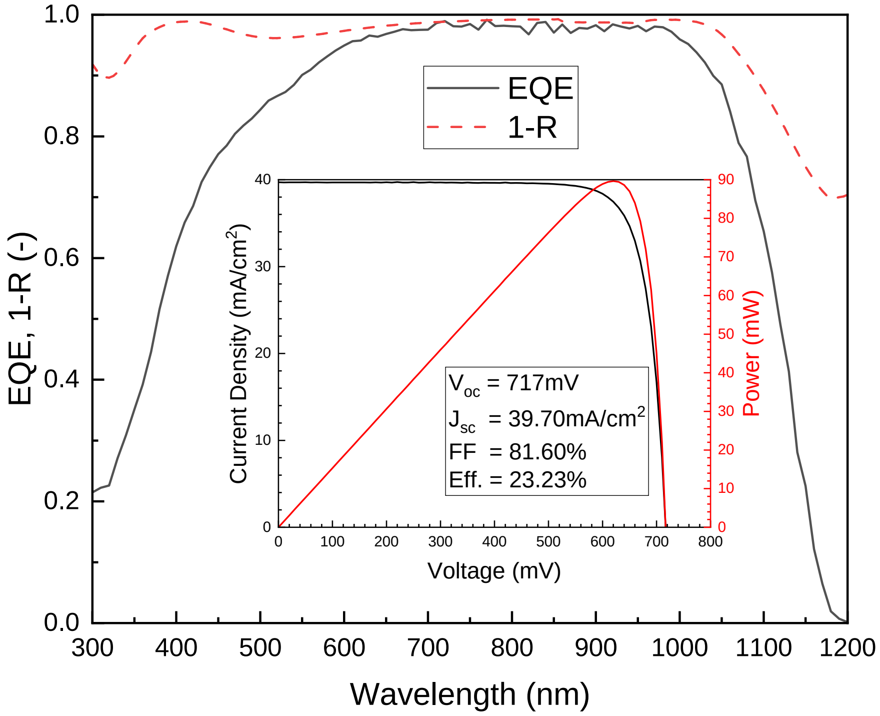

Figure 5.22: EQE, 1-R and J-V curves of the best manufactured FBC SHJ solar cell "X1+D2+Treatments". $J_{SC,EQE}$ = 40.13 mA/cm^2.

5.3 Summary

As passivation quality has been improved by using carefully selected (i)a-Si:H layers composing the bilayer in Chapter 4, this chapter mainly aims to balance surface passivation with carrier transport in FBC-SHJ solar cells. During the fabrication process, Indium Tin Oxide (ITO) was selected as the transparent conductive oxide (TCO) material, and front metal grids were formed through Cu plating. Additionally, SiO_2 was employed as a double-layer anti-reflection coating to enhance light absorption.

In an initial assessment of solar cell performance, the promising bilayer structure labeled as "A1 + D2" from Chapter 4 was subjected to testing. It is crucial to maintain the i1 layer at 1 nm thickness, as increasing this thickness would adversely affect the series resistance (R_S) and the short-circuit current density (J_{SC}), resulting in lower efficiency. Changing the bilayer structure on the p-side led to a 5 mV increase in the open-circuit voltage (V_{OC}) from 711 mV to 716 mV, but the average efficiency achieved was 21.70%, as opposed to the standard cell's 22.24%. This discrepancy was mainly attributed to the higher series resistance, which negatively impacted the fill factor. Consequently, there exists a trade-off between V_{OC} and FF.

A range of R* values for the i1 layer, varying from 0.314 to 0.560, was incorporated into solar cells to assess their performance. As R* increased, the V_{OC} exhibited a rise to an average of 717 mV, followed by a subsequent drop. The increase is coherent with the bilayer (i)a-Si:H passivation results in Chapter 4, and as well as the lifetime of precursors. This indicates that the void-rich and H-rich underdense i1 layer effectively saturate the dangling bonds and suppresses the epitaxial growth. The subsequent decrease in V_{OC} can be a higher defect density in a-Si:H when R* continues to rise. Furthermore, it is also observed that R_S increases with higher R*, indicating the minority carriers are harder to pass with a higher disorder in i1 layer. It is also observed that a slight increase in J_{SC} with higher R*, potentially linked to the widening of the bandgap of the i1 layer with the increasing of H content. After comprehensive assessments of the J-V parameters, X1 with an R* value of 0.382 was identified as the optimal i1 layer.

Combined with a denser D2 film, the R_S resistance of FBC-SHJ solar cell can be reduced, although at the expense of a slightly lower V_{OC} which needs to be further investigated. The best-performing cell X1 + D2 with treatments gives achieved the highest efficiency of 23.23% and the highest V_{OC} of 717 mV. Average efficiency of 22.33% compared to an average of 22.24% of 'non-optimized' standard cells fabricated in previous rounds. It is also observed that after treatments, the FF increases while V_{OC} reduces. However, the observed lack of a clear efficiency improvement could be attributed to the instability of the PECVD tool, which primarily affects the lifetime of precursors, coupled with the relatively large error bars present in the results. However, even without the treatments, FBC-SHJ solar cells remained comparable to cells with treatments and, in some cases, even exhibited better performance.

6 Conclusions and Outlook

The primary objective of this research is to develop high-efficiency FBC-SHJ solar cells utilizing optimized (i)a-Si:H bilayers. The investigation has unfolded progressively, starting from the analysis of film microstructure properties, moving on to layer stack configurations, and finally to the assessment of device performance. During this study, two main topics are investigated: passivation optimization of (i)a-Si:H bilayer, based on the study of microstructure properties of (i)a-Si:H films; and balance the passivation and carrier transport of (i)a-Si:H bilayers that enable high-efficiency FBC-SHJ solar cells. The conclusions are summarized in this chapter, and outlooks for further improvements are given based on the practical experimental experience and the solar cell performance.

6.1 Conclusions

6.1.1 Optimization of the (i)a-Si:H layers

First, focusing on the microstructure properties of (i)a-Si:H layers was established. The database was compiled by systematically varying the PECVD deposition parameters of (i)a-Si:H layers, specifically the pressure (ranging from 0.4 mbar to 3 mbar), power (ranging from 1 W to 12 W), and hydrogen dilution ratio (ranging from 1 to 5). Higher power and pressure settings were found to correspond with an increased absorption strength of high stretching modes (HSM), which in turn indicated a higher R* and higher hydrogen (H) content. These conditions led to the formation of a film that was rich in voids and hydrogen. Further increasing the pressure could potentially decrease the deposition rate while simultaneously contributing to a higher R*. Conversely, a denser a-Si:H film could be achieved through a higher dilution ratio of 5, in which the low stretching modes (LSM) became dominant. Overall, the built database showcases the possibilities to deposit (i)a-Si:H layers with microstructure factor spanning from 0.193 to 0.805.

Subsequently, in order to optimize the passivation capability of (i)a-Si:H bilayer, a series of (i)a-Si:H with various R* from 0.205 to 0.732 has been selected. The investigation revealed that optimal surface passivation was achieved through the combination of an underdense i1 layer with a thickness of 1 nm and a dense i2 layer with a thickness of 9 nm, both deposited on (111)-orientated textured wafer. The void-rich i1 layer, characterized by higher R* and rich H content, could effectively suppress the dangling bonds and prevent epitaxial growth. Conversely, the dense i2 layer deposited with hydrogen-diluted plasma (DR = 5) capped on the top (R* = 0.205) supplied H to the (i)a-Si:H-1/c-Si interface from its highly H diluted plasma and constrained hydrogen within the i1 layer, thus further contributing to better passivation. This optimized combination of (i)a-Si:H bilayer improved the lifetime of symmetrical passivation sample greatly from 2 ms to 7.5 ms, as compared to 'non-optimized' STD1 layer (R* = 0.261) and STD2 layer (R* = 0.314).

Despite various passivation qualities enabled by various bilayer structures (varied from 2 ms to 7.5 ms), after HPT treatment applied to deposited (i)a-Si:H bilayers, the lifetime of all bilayer structures increased drastically to 17 ms, accompanied by FTIR-characterized increases in both H content and R*. That is, the differences in lifetime among various bilayers are not significant, which may indicate the passivation could be saturated after HPT. However, the passivation trend after VHF treatment was not clear. This could potentially be the cause of the instability in the PECVD deposition tool.

6.1.2 Integration of (i)a-Si:H bilayers into the FBC-SHJ solar cells

First, applied to deposited (i)a-Si:H bilayers, a range of R* from 0.314 to 0.560 were incorporated into solar cells on the hole collection side to evaluate their performance. As R* increased, the V_{OC} exhibited a rise from 711 to an average of 717 mV when utilizing the X1 layer with an R* from 0.261 to 0.382. However, this increase was followed by a subsequent decline in V_{OC} when R* value continued to rise. Furthermore, it is also observed that series resistance R_S of solar cells increases when the i1 layer features a higher R*, indicating the minority carriers are hindered to be transported through the i1 layer with a higher degree of disorder.

Then, by using a denser i2 layer, which helps to counteract the elevated series resistance of solar cells associated with the incorporation of the porous X1 layer, the eventual solar cell's R_S is reduced. This combination of "X1 + D2" to a comparable level with standard solar cells, contributing to the enhancement of the fill factor from 78.65% to 80.53%. However, the expense of a slightly lower V_{OC} needs to be further investigated. The best-performing cell endowed with X1 + D2 bilayer with HPT and VHF treatments achieved the highest efficiency of 23.23% (22.33 % on average) and the highest V_{OC} of 717 mV compared with an average of 22.24% and 711 mV of the standard cells fabricated in previous rounds. It is also observed that after hpt and VHF treatments, the FF increases while V_{OC} reduces. However, the observed lack of a clear efficiency improvement when using the optimized bilayer as compared to 'non-optimized' standard bilayer could be attributed to the instability of the PECVD tool, which primarily affects the lifetime of precursors, coupled with the relatively large error bars present in the results.

6.2 Outlook

6.2.1 Layer optimization

Changing deposition parameters in PECVD

During the fabrication process, it is crucial to maintain the i1 layer at 1 nm thickness. Increasing this thickness would adversely affect the series resistance (R_S) and the short-circuit current density (J_{SC}), resulting in lower efficiency. In this thesis, the modification of deposition parameters, specifically power, pressure, and dilution ratio, has been the focus. Although increasing the pressure might potentially reduce the deposition rate while simultaneously increasing R*, in practical experimentation, it is challenging to extend the deposition time to more than 5 s for a 1 nm thickness on the textured surface with a high R*. This is due to the shorter mean free path of the radicals in comparison to the longer travel distance to the substrate. Parameters such as electrode gap, which significantly affects growth conditions optimization [77], and gas flow rate, which plays a pivotal role in gas residence time and depletion [78], could have a correlated relationship with the main deposition parameters altered in this study. Hence, it would be valuable to gather a broader dataset of microstructure properties encompassing a wider range of parameter variations. This approach would provide a more comprehensive understanding of the interactions between different deposition parameters and their impact on film properties.

Hydrogen plasma treatment in between the layers

Instead of the post-hydrogen plasma treatment after deposition of i1 and i2 layers, HPT after i1 prior to i2 could also be added as an option that does not cause any etching effect in a short time. It was found that subjecting the (i1)a-Si:H layer to a 35-second HPT after its deposition led to a reduction in series resistance (Rs) occurred at the hole contact, and passivation quality also showed enhancement. This can be attributed to the reduction in void density, which facilitates more efficient carrier transport, and the saturation of interface states [24]. This approach offers a promising method to further optimize the (i)a-Si:H bilayer structure for enhanced solar cell performance.

IWO-based SHJ device

To further increase the efficiency of the solar cell, RF magnetron sputtered Indium Tungsten Oxide (IWO) TCO material could be used to replace ITO layer. IWO-based SHJ cell has an increased visible-to-near-infrared optical response than ITO-based cell, significantly increasing the current density, thus improved overall cell performance [48].

6.2.2 Improvement in optimization process

There are some proposed improvement methods and measurement tools that could streamline and enhance the optimization process:

- **Enhanced single layer passivation testing:** Similar to the bilayer passivation test outlined in Section 4.2.1, the passivation test of single (i)a-Si:H film on the Topsil wafer that used for solar cell fabrication could be cut into half and deposited with the sample for FTIR measurement simultaneously in PECVD. This could match the microstructure properties of (i)a-Si:H films with passivation efficiently.
- **Contact Resistance Test Structures:** To evaluate the trade-off between passivation and carrier transport in the SHJ solar cells, fabrication of contact resistance test structures for the electron (hole) contact on n-type (p-type) wafers is important for providing more insights [79]. With this approach, contact resistivity (ρ_c) and passivation could be directly compared with different symmetrically deposited intrinsic layer/doped layer stacks [24].
- **Secondary Ion Mass Spectrometry (SIMS) for H content measurment:** Because of the uncertainties and inaccuracies of obtaining H content in the textured wafer by FTIR, H content could be more accurately measured by secondary ion mass spectrometry (SIMS) to analysis the H concentration and redistribution among different layers in depth profiling [80], [81].

6.2.3 Towards large area solar cells

The microstructure properties of (i)a-Si:H database with change of deposition parameters gives a reference to upsacle cells into M2 size with industrial scalable PECVD tool, named Aramis in PVMD group. In addition, due to the supplement of CO_2 in intrinsic depostition chamber in Aramis, a structure of using intrinsic hydrogenated amorphous silicon oxide alloy ((i)a-SiO_x:H) could be investigated further [25].

References

[1] *The Paris Agreement — UNFCCC*. [Online]. Available: `https://unfccc.int/process-and-meetings/the-paris-agreement` (visited on 08/18/2023).

[2] *Global Energy Transitions Stocktake – Topics*, en. [Online]. Available: `https://www.iea.org/topics/global-energy-transitions-stocktake` (visited on 08/18/2023).

[3] Solarpower Europe, *Global Market Outlook For Solar Power 2023 - 2027*. [Online]. Available: `https://www.solarpowereurope.org/insights/outlooks/global-market-outlook-for-solar-power-2023-2027#download` (visited on 08/18/2023).

[4] *2023 Levelized Cost Of Energy+*, en. [Online]. Available: `https://www.lazard.com/research-insights/2023-levelized-cost-of-energyplus/` (visited on 08/18/2023).

[5] *Solar PV still dominates renewable energy capacity additions*, en. [Online]. Available: `https://www.iea.org/energy-system/renewables/solar-pv` (visited on 08/18/2023).

[6] Y. Liu, Y. Li, Y. Wu, *et al.*, "High-Efficiency Silicon Heterojunction Solar Cells: Materials, Devices and Applications," en, *Materials Science and Engineering: R: Reports*, vol. 142, p. 100 579, Oct. 2020, ISSN: 0927796X. DOI: `10.1016/j.mser.2020.100579`. [Online]. Available: `https://linkinghub.elsevier.com/retrieve/pii/S0927796X20300371` (visited on 08/18/2023).

[7] H. Lin, M. Yang, X. Ru, *et al.*, "Silicon heterojunction solar cells with up to 26.81% efficiency achieved by electrically optimized nanocrystalline-silicon hole contact layers," en, *Nature Energy*, May 2023, ISSN: 2058-7546. DOI: `10.1038/s41560-023-01255-2`. [Online]. Available: `https://www.nature.com/articles/s41560-023-01255-2` (visited on 08/18/2023).

[8] R. V. K. Chavali, S. De Wolf, and M. A. Alam, "Device physics underlying silicon heterojunction and passivating-contact solar cells: A topical review," en, *Progress in Photovoltaics: Research and Applications*, vol. 26, no. 4, pp. 241–260, Apr. 2018, ISSN: 1062-7995, 1099-159X. DOI: `10.1002/pip.2959`. [Online]. Available: `https://onlinelibrary.wiley.com/doi/10.1002/pip.2959` (visited on 08/19/2023).

[9] M. Tanaka, M. Taguchi, T. Matsuyama, *et al.*, "Development of New a-Si/c-Si Heterojunction Solar Cells: ACJ-HIT (Artificially Constructed Junction-Heterojunction with Intrinsic Thin-Layer)," *Japanese Journal of Applied Physics*, vol. 31, no. 11R, p. 3518, Nov. 1992, ISSN: 0021-4922, 1347-4065. DOI: `10.1143/JJAP.31.3518`. [Online]. Available: `https://iopscience.iop.org/article/10.1143/JJAP.31.3518` (visited on 08/19/2023).

[10] M. Tanaka, S. Okamoto, S. Tsuge, and S. Kiyama, “Development of hit solar cells with more than 21% conversion efficiency and commercialization of highest performance hit modules,” in *Proceedings of 3rd World Conference onPhotovoltaic Energy Conversion, 2003*, vol. 1, May 2003, 955–958 Vol.1.

[11] Y. Zhao, L. Mazzarella, P. Procel, *et al.*, “Doped hydrogenated nanocrystalline silicon oxide layers for high-efficiency c-Si heterojunction solar cells,” en, *Progress in Photovoltaics: Research and Applications*, vol. 28, no. 5, pp. 425–435, 2020, ISSN: 1099-159X. DOI: `10.1002/pip.3256`. [Online]. Available: `https://onlinelibrary.wiley.com/doi/abs/10.1002/pip.3256` (visited on 08/11/2023).

[12] Z. Sun, X. Chen, Y. He, *et al.*, “Toward Efficiency Limits of Crystalline Silicon Solar Cells: Recent Progress in High-Efficiency Silicon Heterojunction Solar Cells,” en, *Advanced Energy Materials*, vol. 12, no. 23, p. 2 200 015, Jun. 2022, ISSN: 1614-6832, 1614-6840. DOI: `10.1002/aenm.202200015`. [Online]. Available: `https://onlinelibrary.wiley.com/doi/10.1002/aenm.202200015` (visited on 08/19/2023).

[13] C. Han, “High-Mobility TCO-Based Contacting Schemes for c-Si Solar Cells,” en, 2022. DOI: `10.4233/uuid:d6f35adf-486e-453a-9ae9-679a81105bed`. [Online]. Available: `https://repository.tudelft.nl/islandora/object/uuid%3Ad6f35adf-486e-453a-9ae9-679a81105bed` (visited on 06/22/2023).

[14] K. Yoshikawa, W. Yoshida, T. Irie, *et al.*, “Exceeding conversion efficiency of 26% by heterojunction interdigitated back contact solar cell with thin film Si technology,” en, *Solar Energy Materials and Solar Cells*, vol. 173, pp. 37–42, Dec. 2017, ISSN: 09270248. DOI: `10.1016/j.solmat.2017.06.024`. [Online]. Available: `https://linkinghub.elsevier.com/retrieve/pii/S092702481730332X` (visited on 08/19/2023).

[15] C. Ballif, F.-J. Haug, M. Boccard, P. J. Verlinden, and G. Hahn, “Status and perspectives of crystalline silicon photovoltaics in research and industry,” en, *Nature Reviews Materials*, vol. 7, no. 8, pp. 597–616, Mar. 2022, ISSN: 2058-8437. DOI: `10.1038/s41578-022-00423-2`. [Online]. Available: `https://www.nature.com/articles/s41578-022-00423-2` (visited on 08/19/2023).

[16] H. Sai, H.-J. Hsu, P.-W. Chen, P.-L. Chen, and T. Matsui, “Intrinsic Amorphous Silicon Bilayers for Effective Surface Passivation in Silicon Heterojunction Solar Cells: A Comparative Study of Interfacial Layers,” en, *physica status solidi (a)*, vol. 218, no. 9, p. 2 000 743, 2021, ISSN: 1862-6319. DOI: `10.1002/pssa.202000743`. [Online]. Available: `https://onlinelibrary.wiley.com/doi/abs/10.1002/pssa.202000743` (visited on 08/08/2023).

[17] X. Ru, M. Qu, J. Wang, *et al.*, “25.11% efficiency silicon heterojunction solar cell with low deposition rate intrinsic amorphous silicon buffer layers,” en, *Solar Energy Materials and Solar Cells*, vol. 215, p. 110 643, Sep. 2020, ISSN: 0927-0248. DOI: `10.1016/j.solmat.2020.110643`. [Online]. Available: `https://www.sciencedirect.com/science/article/pii/S0927024820302464` (visited on 08/08/2023).

[18] W. Liu, L. Zhang, R. Chen, *et al.*, “Underdense a-Si:H film capped by a dense film as the passivation layer of a silicon heterojunction solar cell,” en, *Journal of Applied Physics*, vol. 120, no. 17, p. 175 301, Nov. 2016, ISSN: 0021-8979, 1089-7550. DOI: `10.1063/1.4966941`. [Online]. Available: `https://pubs.aip.org/jap/article/120/`

17/175301/345737/Underdense-a-Si-H-film-capped-by-a-dense-film-as (visited on 08/16/2023).

[19] W. Duan, A. Lambertz, K. Bittkau, *et al.*, "A route towards high-efficiency silicon heterojunction solar cells," en, *Progress in Photovoltaics: Research and Applications*, vol. 30, no. 4, pp. 384–392, Apr. 2022, ISSN: 1062-7995, 1099-159X. DOI: 10.1002/pip.3493. [Online]. Available: https://onlinelibrary.wiley.com/doi/10.1002/pip.3493 (visited on 08/18/2023).

[20] H. Sai, P.-W. Chen, H.-J. Hsu, T. Matsui, S. Nunomura, and K. Matsubara, "Impact of intrinsic amorphous silicon bilayers in silicon heterojunction solar cells," *Journal of Applied Physics*, vol. 124, no. 10, p. 103 102, Sep. 2018, ISSN: 0021-8979. DOI: 10.1063/1.5045155. [Online]. Available: https://doi.org/10.1063/1.5045155 (visited on 08/09/2023).

[21] S. Kim, V. Ai Dao, Y. Lee, *et al.*, "Processed optimization for excellent interface passivation quality of amorphous/crystalline silicon solar cells," en, *Solar Energy Materials and Solar Cells*, vol. 117, pp. 174–177, Oct. 2013, ISSN: 09270248. DOI: 10.1016/j.solmat.2013.05.042. [Online]. Available: https://linkinghub.elsevier.com/retrieve/pii/S0927024813002651 (visited on 08/19/2023).

[22] Y. Zhao, P. Procel, A. Smets, *et al.*, "Effects of (i)a-Si:H deposition temperature on high-efficiency silicon heterojunction solar cells," en, *Progress in Photovoltaics: Research and Applications*, vol. n/a, no. n/a, ISSN: 1099-159X. DOI: 10.1002/pip.3620. [Online]. Available: https://onlinelibrary.wiley.com/doi/abs/10.1002/pip.3620 (visited on 08/04/2023).

[23] S. M. Karabanov and M. A. Reginevich, "Impact of Hydrogen Plasma Treatment on Intrinsic Amorphous Silicon Bilayers in Silicon Heterojunction Solar Cells," in *2021 IEEE International Conference on Environment and Electrical Engineering and 2021 IEEE Industrial and Commercial Power Systems Europe (EEEIC / I&CPS Europe)*, Bari, Italy: IEEE, Sep. 2021, pp. 1–5, ISBN: 978-1-66543-613-7. DOI: 10.1109/EEEIC/ICPSEurope51590.2021.9584467. [Online]. Available: https://ieeexplore.ieee.org/document/9584467/ (visited on 08/11/2023).

[24] C. Luderer, D. Kurt, A. Moldovan, M. Hermle, and M. Bivour, "Intrinsic layer modification in silicon heterojunctions: Balancing transport and surface passivation," en, *Solar Energy Materials and Solar Cells*, vol. 238, p. 111 412, May 2022, ISSN: 09270248. DOI: 10.1016/j.solmat.2021.111412. [Online]. Available: https://linkinghub.elsevier.com/retrieve/pii/S0927024821004542 (visited on 08/17/2023).

[25] L. Wen, L. Zhao, G. Wang, *et al.*, "Beyond 25% efficient crystalline silicon heterojunction solar cells with hydrogenated amorphous silicon oxide stacked passivation layers for rear emitter," en, *Solar Energy Materials and Solar Cells*, vol. 258, p. 112 429, Aug. 2023, ISSN: 09270248. DOI: 10.1016/j.solmat.2023.112429. [Online]. Available: https://linkinghub.elsevier.com/retrieve/pii/S0927024823002507 (visited on 08/19/2023).

[26] M. Boccard and Z. C. Holman, “Amorphous silicon carbide passivating layers for crystalline-silicon-based heterojunction solar cells,” en, *Journal of Applied Physics*, vol. 118, no. 6, p. 065 704, Aug. 2015, ISSN: 0021-8979, 1089-7550. DOI: 10.1063/1.4928203. [Online]. Available: https://pubs.aip.org/jap/article/118/6/065704/140773/Amorphous-silicon-carbide-passivating-layers-for (visited on 08/19/2023).

[27] K. Ohdaira, T. Oikawa, K. Higashimine, and H. Matsumura, “Suppression of the epitaxial growth of Si films in Si heterojunction solar cells by the formation of ultra-thin oxide layers,” en, *Current Applied Physics*, vol. 16, no. 9, pp. 1026–1029, Sep. 2016, ISSN: 15671739. DOI: 10.1016/j.cap.2016.06.001. [Online]. Available: https://linkinghub.elsevier.com/retrieve/pii/S156717391630147X (visited on 08/19/2023).

[28] M. Lozac’h, S. Nunomura, H. Sai, and K. Matsubara, “Passivation property of ultrathin SiOx:H / a-Si:H stack layers for solar cell applications,” en, *Solar Energy Materials and Solar Cells*, vol. 185, pp. 8–15, Oct. 2018, ISSN: 0927-0248. DOI: 10.1016/j.solmat.2018.05.004. [Online]. Available: https://www.sciencedirect.com/science/article/pii/S0927024818302162 (visited on 06/21/2023).

[29] A. Smets, K. Jäger, O. Isabella, R. van Swaaij, and M. Zeman, *Solar Energy: The physics and engineering of photovoltaic conversion, technologies and systems*. Cambridge: UIT Cambridge Limited, 2016, ISBN: 978-1-906860-32-5. [Online]. Available: https://www.amazon.com/Solar-Energy-Engineering-Photovoltaic-Technologies/dp/1906860327 (visited on 07/25/2023).

[30] W. G. J. H. M. Van Sark, L. Korte, and F. Roca, Eds., *Physics and Technology of Amorphous-Crystalline Heterostructure Silicon Solar Cells* (Engineering Materials), en. Berlin, Heidelberg: Springer, 2012, vol. 0, ISBN: 978-3-642-22274-0 978-3-642-22275-7. DOI: 10.1007/978-3-642-22275-7. [Online]. Available: https://link.springer.com/10.1007/978-3-642-22275-7 (visited on 07/25/2023).

[31] E. Płaczek-Popko, “Top PV market solar cells 2016,” *Opto-Electronics Review; 2017; vol. 25; No 2; 55-64*, 2017, Publisher: Polish Academy of Sciences and Association of Polish Electrical Engineers in cooperation with Military University of Technology, ISSN: 1896-3757. [Online]. Available: https://czasopisma.pan.pl/dlibra/publication/132040/edition/115347 (visited on 08/21/2023).

[32] Y. Liu, Y. Sun, W. Liu, and J. Yao, “Novel high-efficiency crystalline-silicon-based compound heterojunction solar cells: HCT (heterojunction with compound thin-layer),” en, *Physical Chemistry Chemical Physics*, vol. 16, no. 29, pp. 15 400–15 410, Jul. 2014, Publisher: The Royal Society of Chemistry, ISSN: 1463-9084. DOI: 10.1039/C4CP00668B. [Online]. Available: https://pubs.rsc.org/en/content/articlelanding/2014/cp/c4cp00668b (visited on 08/21/2023).

[33] J. Haschke, O. Dupré, M. Boccard, and C. Ballif, “Silicon heterojunction solar cells: Recent technological development and practical aspects - from lab to industry,” en, *Solar Energy Materials and Solar Cells*, vol. 187, pp. 140–153, Dec. 2018, ISSN: 09270248. DOI: 10.1016/j.solmat.2018.07.018. [Online]. Available: https://linkinghub.elsevier.com/retrieve/pii/S0927024818303805 (visited on 08/21/2023).

[34] A. Descoeudres, L. Barraud, S. De Wolf, *et al.*, "Improved amorphous/crystalline silicon interface passivation by hydrogen plasma treatment," en, *Applied Physics Letters*, vol. 99, no. 12, p. 123 506, Sep. 2011, ISSN: 0003-6951, 1077-3118. DOI: `10.1063/1.3641899`. [Online]. Available: `https://pubs.aip.org/apl/article/99/12/123506/340741/Improved-amorphous-crystalline-silicon-interface` (visited on 08/17/2023).

[35] A. Siddique, M. Hasan, M. Matin, N. Amin, and M. M. Rahman, "Modeling and Simulation of Highly Efficient Amorphous Silicon Single Junction Solar Cell," Dec. 2017.

[36] M. Stuckelberger, R. Biron, N. Wyrsch, F.-J. Haug, and C. Ballif, "Review: Progress in solar cells from hydrogenated amorphous silicon," *Renewable and Sustainable Energy Reviews*, vol. 76, pp. 1497–1523, Sep. 2017, ISSN: 1364-0321. DOI: `10.1016/j.rser.2016.11.190`. [Online]. Available: `https://www.sciencedirect.com/science/article/pii/S1364032116309467` (visited on 08/21/2023).

[37] J. C. Sturm, Y. Huang, L. Han, *et al.*, "Amorphous silicon: The other silicon," in *Ulis 2011 Ultimate Integration on Silicon*, Cork, Ireland: IEEE, Mar. 2011, pp. 1–4, ISBN: 978-1-4577-0090-3. DOI: `10.1109/ULIS.2011.5758011`. [Online]. Available: `http://ieeexplore.ieee.org/document/5758011/` (visited on 08/22/2023).

[38] A. H. M. Smets and M. C. M. Van De Sanden, "Relation of the Si H stretching frequency to the nanostructural Si H bulk environment," en, *Physical Review B*, vol. 76, no. 7, p. 073 202, Aug. 2007, ISSN: 1098-0121, 1550-235X. DOI: `10.1103/PhysRevB.76.073202`. [Online]. Available: `https://link.aps.org/doi/10.1103/PhysRevB.76.073202` (visited on 08/22/2023).

[39] J. Panigrahi and V. K. Komarala, "Progress on the intrinsic a-Si:H films for interface passivation of silicon heterojunction solar cells: A review," en, *Journal of Non-Crystalline Solids*, vol. 574, p. 121 166, Dec. 2021, ISSN: 0022-3093. DOI: `10.1016/j.jnoncrysol.2021.121166`. [Online]. Available: `https://www.sciencedirect.com/science/article/pii/S0022309321005299` (visited on 08/05/2023).

[40] Y.-S. Cho, C.-H. Hsu, S.-Y. Lien, D.-S. Wuu, and I.-C. Hsieh, "Effect of Hydrogen Content in Intrinsic a-Si:H on Performances of Heterojunction Solar Cells," en, *International Journal of Photoenergy*, vol. 2013, e121875, Sep. 2013, Publisher: Hindawi, ISSN: 1110-662X. DOI: `10.1155/2013/121875`. [Online]. Available: `https://www.hindawi.com/journals/ijp/2013/121875/` (visited on 08/21/2023).

[41] *Light Trapping — PVEducation*. [Online]. Available: `https://www.pveducation.org/pvcdrom/design-of-silicon-cells/light-trapping` (visited on 06/22/2023).

[42] D. Deligiannis, S. Alivizatos, A. Ingenito, *et al.*, "Wet-chemical Treatment for Improved Surface Passivation of Textured Silicon Heterojunction Solar Cells," en, *Energy Procedia*, vol. 55, pp. 197–202, Jan. 2014, Publisher: Elsevier, ISSN: 1876-6102. DOI: `10.1016/j.egypro.2014.08.117`. [Online]. Available: `https://www.sciencedirect.com/science/article/pii/S1876610214013423` (visited on 07/25/2023).

[43] D. B. Fenner, D. K. Biegelsen, and R. D. Bringans, “Silicon surface passivation by hydrogen termination: A comparative study of preparation methods,” *Journal of Applied Physics*, vol. 66, no. 1, pp. 419–424, Jul. 1989, ISSN: 0021-8979. DOI: `10.1063/1.343839`. [Online]. Available: `https://doi.org/10.1063/1.343839` (visited on 07/25/2023).

[44] E. Yablonovitch, D. L. Allara, C. C. Chang, T. Gmitter, and T. B. Bright, “Unusually Low Surface-Recombination Velocity on Silicon and Germanium Surfaces,” *Physical Review Letters*, vol. 57, no. 2, pp. 249–252, Jul. 1986, Publisher: American Physical Society. DOI: `10.1103/PhysRevLett.57.249`. [Online]. Available: `https://link.aps.org/doi/10.1103/PhysRevLett.57.249` (visited on 07/25/2023).

[45] D. Deligiannis, “Surface Passivation for Silicon Heterojunction Solar Cells,” en, 2017. DOI: `10.4233/uuid:73f1fba5-dbe1-49bb-a34c-66a35dca32d8`. [Online]. Available: `https://repository.tudelft.nl/islandora/object/uuid%3A73f1fba5-dbe1-49bb-a34c-66a35dca32d8` (visited on 08/19/2023).

[46] K. Kovačević, “Simplified processing of interdigitated-back-contacted silicon heterojunction solar cells,” en, 2022. [Online]. Available: `https://repository.tudelft.nl/islandora/object/uuid%3A20e68de3-f3ae-4fc7-b8a1-91be086a6a18` (visited on 08/19/2023).

[47] *WHAT IS MAGNETRON SPUTTERING?* en-US. [Online]. Available: `https://www.polyteknik.com/technology/sputtering/` (visited on 08/20/2023).

[48] C. Han, Y. Zhao, L. Mazzarella, *et al.*, “Room-temperature sputtered tungsten-doped indium oxide for improved current in silicon heterojunction solar cells,” en, *Solar Energy Materials and Solar Cells*, vol. 227, p. 111 082, Aug. 2021, ISSN: 09270248. DOI: `10.1016/j.solmat.2021.111082`. [Online]. Available: `https://linkinghub.elsevier.com/retrieve/pii/S0927024821001239` (visited on 08/20/2023).

[49] G. Yang, “High-efficient n-i-p thin-film silicon solar cells,” en, 2015. [Online]. Available: `https://repository.tudelft.nl/islandora/object/uuid%3A50a4a249-3373-48b4-90b9-5ed2b7098579` (visited on 08/20/2023).

[50] G. Papakonstantinou, “Investigation and Optimization of the Front Metal Contact of Silicon Heterojunction Solar Cells,” en, 2014. [Online]. Available: `https://repository.tudelft.nl/islandora/object/uuid%3A4f372da0-7325-424a-88ba-491c08054300` (visited on 08/19/2023).

[51] T. Hatt, J. Bartsch, S. Kluska, S. Nold, S. W. Glunz, and M. Glatthaar, “Low-cost Cu-plated metallization on TCOs for SHJ Solar Cells - Optimization of PVD Contacting-layer,” in *2020 47th IEEE Photovoltaic Specialists Conference (PVSC)*, 2020, pp. 0397–0400. DOI: `10.1109/PVSC45281.2020.9300706`.

[52] G. Limodio, Y. De Groot, G. Van Kuler, *et al.*, “Copper-Plating Metallization With Alternative Seed Layers for c-Si Solar Cells Embedding Carrier-Selective Passivating Contacts,” *IEEE Journal of Photovoltaics*, vol. 10, no. 2, pp. 372–382, Mar. 2020, Conference Name: IEEE Journal of Photovoltaics, ISSN: 2156-3403. DOI: `10.1109/JPHOTOV.2019.2957671`.

[53] *Potentiostat.* [Online]. Available: `https://www3.nd.edu/~kamatlab/documents/facilities/potentiostat.pdf` (visited on 10/27/2022).

[54] C. Han, G. Yang, P. Procel, *et al.*, "Controllable Simultaneous Bifacial Cu-Plating for High-Efficiency Crystalline Silicon Solar Cells," *Solar RRL*, vol. 6, no. 6, p. 2 100 810, 2022, _eprint: https://onlinelibrary.wiley.com/doi/pdf/10.1002/solr.202100810. DOI: https://doi.org/10.1002/solr.202100810. [Online]. Available: https://onlinelibrary.wiley.com/doi/abs/10.1002/solr.202100810.

[55] L. Wei, *Copper electroplating fundamentals.* en-US. [Online]. Available: https://www.dupont.com/electronic-materials/blogs/knowledge/copper-electroplating-fundamentals.html (visited on 10/24/2022).

[56] J. Ojeda and M. Dittrich, "Fourier Transform Infrared Spectroscopy for Molecular Analysis of Microbial Cells," *Methods in molecular biology (Clifton, N.J.)*, vol. 881, pp. 187–211, Apr. 2012, ISSN: 978-1-61779-826-9. DOI: 10.1007/978-1-61779-827-6_8.

[57] F. A. Settle, *Handbook of instrumental techniques for analytical chemistry*, eng. Upper Saddle River, NJ: Prentice Hall PTR, 1997, OCLC: 36656437, ISBN: 978-0-13-177338-7.

[58] T. Scientific, *Omnic User Manual 2004*. [Online]. Available: https://mmrc.caltech.edu/FTIR/Nicolet/Nicolet%20manuals/Omnic%20User%20Manual%202004.pdf (visited on 07/25/2023).

[59] A. A. Langford, M. L. Fleet, B. P. Nelson, W. A. Lanford, and N. Maley, "Infrared absorption strength and hydrogen content of hydrogenated amorphous silicon," *Phys. Rev. B*, vol. 45, pp. 13 367–13 377, 23 Jun. 1992. DOI: 10.1103/PhysRevB.45.13367. [Online]. Available: https://link.aps.org/doi/10.1103/PhysRevB.45.13367.

[60] A. H. M. Smets, W. M. M. Kessels, and M. C. M. Van De Sanden, "Vacancies and voids in hydrogenated amorphous silicon," en, *Applied Physics Letters*, vol. 82, no. 10, pp. 1547–1549, Mar. 2003, ISSN: 0003-6951, 1077-3118. DOI: 10.1063/1.1559657. [Online]. Available: https://pubs.aip.org/apl/article/82/10/1547/513967/Vacancies-and-voids-in-hydrogenated-amorphous (visited on 08/18/2023).

[61] Y. Zhang, M. Kim, L. Wang, P. Verlinden, and B. Hallam, "Design considerations for multi-terawatt scale manufacturing of existing and future photovoltaic technologies: Challenges and opportunities related to silver, indium and bismuth consumption," en, *Energy & Environmental Science*, vol. 14, no. 11, pp. 5587–5610, 2021, Publisher: Royal Society of Chemistry. DOI: 10.1039/D1EE01814K. [Online]. Available: https://pubs.rsc.org/en/content/articlelanding/2021/ee/d1ee01814k (visited on 10/24/2022).

[62] A. A. Langford, M. L. Fleet, B. P. Nelson, W. A. Lanford, and N. Maley, "Infrared absorption strength and hydrogen content of hydrogenated amorphous silicon," en, *Physical Review B*, vol. 45, no. 23, pp. 13 367–13 377, Jun. 1992, ISSN: 0163-1829, 1095-3795. DOI: 10.1103/PhysRevB.45.13367. [Online]. Available: https://link.aps.org/doi/10.1103/PhysRevB.45.13367 (visited on 08/16/2023).

[63] E. Bhattacharya and A. H. Mahan, "Microstructure and the light-induced metastability in hydrogenated amorphous silicon," en, *Applied Physics Letters*, vol. 52, no. 19, pp. 1587–1589, May 1988, ISSN: 0003-6951, 1077-3118. DOI: 10.1063/1.99089. [Online]. Available: https://pubs.aip.org/apl/article/52/19/1587/53765/Microstructure-and-the-light-induced-metastability (visited on 08/19/2023).

[64] Y. Zhao, "Contact Stack Evaluation for SHJ Solar Cells and Process Development of IBC-SHJ Solar Cells," en, 2018. [Online]. Available: https://repository.tudelft.nl/islandora/object/uuid%3A77f483ae-f1da-42c1-8c5a-ae601b140d90 (visited on 08/20/2023).

[65] D. Pysch, A. Mette, and S. Glunz, "A review and comparison of different methods to determine the series resistance of solar cells," en, *Solar Energy Materials and Solar Cells*, vol. 91, no. 18, pp. 1698–1706, Nov. 2007, ISSN: 09270248. DOI: 10.1016/j.solmat.2007.05.026. [Online]. Available: https://linkinghub.elsevier.com/retrieve/pii/S0927024807002255 (visited on 08/20/2023).

[66] L. Xiao, Y. Yan, and S. Yang, "Uniformity improvement of a-C: H films prepared by PECVD," in *2015 China Semiconductor Technology International Conference*, ISSN: 2158-2297, Mar. 2015, pp. 1–3. DOI: 10.1109/CSTIC.2015.7153412.

[67] J. Ge, Z. Ling, J. Wong, T. Mueller, and A. Aberle, "Optimisation of Intrinsic a-Si:H Passivation Layers in Crystalline-amorphous Silicon Heterojunction Solar Cells," en, *Energy Procedia*, vol. 15, pp. 107–117, 2012, ISSN: 18766102. DOI: 10.1016/j.egypro.2012.02.013. [Online]. Available: https://linkinghub.elsevier.com/retrieve/pii/S1876610212003499 (visited on 08/17/2023).

[68] U. Kroll, J. Meier, P. Torres, J. Pohl, and A. Shah, "From amorphous to microcrystalline silicon films prepared by hydrogen dilution using the VHF (70 MHz) GD technique," en, *Journal of Non-Crystalline Solids*, vol. 227-230, pp. 68–72, May 1998, ISSN: 00223093. DOI: 10.1016/S0022-3093(98)00329-9. [Online]. Available: https://linkinghub.elsevier.com/retrieve/pii/S0022309398003299 (visited on 08/17/2023).

[69] J. Ge, Z. P. Ling, J. Wong, T. Mueller, and A. G. Aberle, "Optimisation of Intrinsic a-Si:H Passivation Layers in Crystalline-amorphous Silicon Heterojunction Solar Cells," *Energy Procedia*, vol. 15, pp. 107–117, 2012, ISSN: 1876-6102. DOI: https://doi.org/10.1016/j.egypro.2012.02.013. [Online]. Available: https://www.sciencedirect.com/science/article/pii/S1876610212003499.

[70] A. Neumüller, O. Sergeev, S. J. Heise, *et al.*, "Improved amorphous silicon passivation layer for heterojunction solar cells with post-deposition plasma treatment," en, *Nano Energy*, vol. 43, pp. 228–235, Jan. 2018, ISSN: 2211-2855. DOI: 10.1016/j.nanoen.2017.11.053. [Online]. Available: https://www.sciencedirect.com/science/article/pii/S2211285517307395 (visited on 08/11/2023).

[71] M. Mews, T. F. Schulze, N. Mingirulli, and L. Korte, "Hydrogen plasma treatments for passivation of amorphous-crystalline silicon-heterojunctions on surfaces promoting epitaxy," en, *Applied Physics Letters*, vol. 102, no. 12, p. 122 106, Mar. 2013, ISSN: 0003-6951, 1077-3118. DOI: 10.1063/1.4798292. [Online]. Available:

https://pubs.aip.org/apl/article/102/12/122106/24989/Hydrogen-plasma-treatments-for-passivation-of (visited on 08/11/2023).

[72] F. Finger, P. Hapke, M. Luysberg, R. Carius, H. Wagner, and M. Scheib, “Improvement of grain size and deposition rate of microcrystalline silicon by use of very high frequency glow discharge,” en, *Applied Physics Letters*, vol. 65, no. 20, pp. 2588–2590, Nov. 1994, ISSN: 0003-6951, 1077-3118. DOI: 10.1063/1.112604. [Online]. Available: https://pubs.aip.org/apl/article/65/20/2588/522708/Improvement-of-grain-size-and-deposition-rate-of (visited on 08/11/2023).

[73] D. Zhang, I. A. Digdaya, R. Santbergen, *et al.*, “Design and fabrication of a SiOx/ITO double-layer anti-reflective coating for heterojunction silicon solar cells,” *Solar Energy Materials and Solar Cells*, Dye Sensitized Solar Cells, Organic, Hybrid Solar Cells and New Concepts, vol. 117, pp. 132–138, Oct. 2013, ISSN: 0927-0248. DOI: 10.1016/j.solmat.2013.05.044. [Online]. Available: https://www.sciencedirect.com/science/article/pii/S0927024813002675 (visited on 08/16/2023).

[74] T. Ruan, M. Qu, X. Qu, *et al.*, “Achieving high efficiency silicon heterojunction solar cells by applying high hydrogen content amorphous silicon as epitaxial-free buffer layers,” *Thin Solid Films*, vol. 711, p. 138 305, Oct. 2020, ISSN: 0040-6090. DOI: 10.1016/j.tsf.2020.138305. [Online]. Available: https://www.sciencedirect.com/science/article/pii/S0040609020305149 (visited on 08/15/2023).

[75] T. F. Schulze, L. Korte, F. Ruske, and B. Rech, “Band lineup in amorphous/crystalline silicon heterojunctions and the impact of hydrogen microstructure and topological disorder,” en, *Physical Review B*, vol. 83, no. 16, p. 165 314, Apr. 2011, ISSN: 1098-0121, 1550-235X. DOI: 10.1103/PhysRevB.83.165314. [Online]. Available: https://link.aps.org/doi/10.1103/PhysRevB.83.165314 (visited on 08/20/2023).

[76] B. Fischer, W. Beyer, A. Lambertz, *et al.*, “The Microstructure of Underdense Hydrogenated Amorphous Silicon and its Application to Silicon Heterojunction Solar Cells,” en, *Solar RRL*, vol. 7, no. 10, p. 2 300 103, 2023, ISSN: 2367-198X. DOI: 10.1002/solr.202300103. [Online]. Available: https://onlinelibrary.wiley.com/doi/abs/10.1002/solr.202300103 (visited on 08/17/2023).

[77] M. Isomura, M. Kondo, and A. Matsuda, “Device-Grade Amorphous Silicon Prepared by High-Pressure Plasma,” en, *Japanese Journal of Applied Physics*, vol. 41, no. Part 1, No. 4A, pp. 1947–1951, Apr. 2002, ISSN: 0021-4922, 1347-4065. DOI: 10.1143/JJAP.41.1947. [Online]. Available: https://iopscience.iop.org/article/10.1143/JJAP.41.1947 (visited on 08/20/2023).

[78] A. Pandey, S. Bhattacharya, J. Panigrahi, S. Mandal, and V. K. Komarala, “Effect of Gas Flow Rate in PECVD of Amorphous Silicon Thin Films for Interface Passivation of Silicon Heterojunction Solar Cells,” en, *physica status solidi (a)*, vol. 219, no. 16, p. 2 200 183, Aug. 2022, ISSN: 1862-6300, 1862-6319. DOI: 10.1002/pssa.202200183. [Online]. Available: https://onlinelibrary.wiley.com/doi/10.1002/pssa.202200183 (visited on 08/20/2023).

[79] C. Luderer, L. Tutsch, C. Messmer, M. Hermle, and M. Bivour, “Influence of TCO and a-Si:H Doping on SHJ Contact Resistivity,” *IEEE Journal of Photovoltaics*, vol. 11, no. 2, pp. 329–336, Mar. 2021, ISSN: 2156-3381, 2156-3403. DOI: 10.1109/JPHOTOV.2021.3051206. [Online]. Available: https://ieeexplore.ieee.org/document/9340291/ (visited on 08/20/2023).

[80] J. Christensen, A. Ulyashin, K. Maknys, A. Kuznetsov, and B. Svensson, “Analysis of thin layers and interfaces in ITO/a-Si:H/c-Si heterojunction solar cell structures by secondary ion mass spectrometry,” en, *Thin Solid Films*, vol. 511-512, pp. 93–97, Jul. 2006, ISSN: 00406090. DOI: 10.1016/j.tsf.2005.12.007. [Online]. Available: https://linkinghub.elsevier.com/retrieve/pii/S0040609005023345 (visited on 08/20/2023).

[81] C. Magee and D. E. Carlson, “Investigation of the hydrogen and impurity contents of amorphous silicon by secondary ion mass spectrometry,” en, *Solar Cells*, vol. 2, no. 4, pp. 365–376, Dec. 1980, ISSN: 03796787. DOI: 10.1016/0379-6787(80)90012-5. [Online]. Available: https://linkinghub.elsevier.com/retrieve/pii/0379678780900125 (visited on 08/20/2023).